Imperial College London

Biomimetic Orthopaedic Implants

Harnessing Bone's Remodelling Response with Additive Manufacturing

By

Maxwell James Munford

A thesis submitted to Imperial College London for the degree of Doctor of Philosophy and the Diploma of Imperial College

Department of Mechanical Engineering

Imperial College London, SW7 2AZ

Originality Declaration

I, Maxwell Munford hereby declare that all work contained in this thesis has been produced by me and that all else has been appropriately referenced.

Copyright Declaration

The copyright of this thesis rests with the author. Unless otherwise indicated, its contents are licensed under a Creative Commons Attribution-Non Commercial-No Derivatives 4.0 International Licence (CC BY-NC-ND).

Under this licence, you may copy and redistribute the material in any medium or format on the condition that; you credit the author, do not use it for commercial purposes and do not distribute modified versions of the work.

When reusing or sharing this work, ensure you make the licence terms clear to others by naming the licence and linking to the licence text.

Please seek permission from the copyright holder for uses of this work that are not included in this licence or permitted under UK Copyright Law.

Abstract

The long-term healing of bone is inherently coupled with the strain it experiences, as described by numerous laws governing bone's mechanobiology and natural remodelling process. Bone regeneration can therefore be accelerated by the use of porous structures in orthopaedics which have a mechanical modulus akin to the bone being replaced. Following design and regulatory requirements, a further consideration is that yield strength and fatigue strength must be suitable for the implants applications. Conventional orthopaedic implants are solid metal so therefore have excessive strength and stiffness. This means that they cause regions of bone to be underloaded, leading to bone resorption which complicates surgery. This PhD explored optimising additively manufactured (AM) porous structures for application as bone growth stimulating orthopaedic implants. The mechanical modulus, strength and anisotropy of bone and AM structures was characterised in a workflow which uses manufacturing and imaging methods commonly used in industry. Following this, individual AM structures were designed and manufactured based on computed tomography (CT) scans of bone to control the strain experienced. Orthopaedic implants were then manufactured which replicated the loading and strain environment experienced in healthy bone. Mechanical mappings of bone and AM structures were shown to predict properties to within 5.6% and 2%, while custom AM implants could control bone strain from -15% to +15% of homeostasis (corresponding to an extension of -4500 μm to 4500 μm). Conventional solid counter parts underloaded up to 70% of peri-prospethic bone, whereas AM implants closely replicated the loaded experienced by bone prior to implantation (achieving mechanical environments which were 68-78% similar). This thesis has emphasis on understanding bone's mechanical properties and the effect of implants on mechanical stimulus, which will allow for more accurate testing of the mechanical behaviour of bone in response to implanted porous scaffolds and for better translation from in vivo studies to commercial implants.

Acknowledgements

First and foremost, I would like to thank Dr Jonathan Jeffers for providing me with the opportunity and freedom to research a topic that I have found so interesting. Your continued guidance, knowledge, support and enthusiasm have been truly invaluable – I have very much enjoyed studying for my PhD under your supervision.

It was also a pleasure to work with and learn from my co-authors: Dannier Xiao, Jennifer Stoddart, Dr. Umar Hossain, Dr. Shaaz Ghouse, Dr. Geoffrey Ng, Mr. Alex Liddle and Prof. Justin Cobb. You were all so willing to share your knowledge, ideas and previous work with me and this greatly improved my own research. Thank you.

To all the members of the Biomechanics group, thank you, because undoubtedly you have helped me during this time and I have enjoyed working with you all. In particular, thank you to the pie boys who were with me from day one on this journey. I have had a lot of fun working with you all – you are all excellent people.

I am truly grateful for the financial support I personally received from Renishaw plc and the Engineering and Physical Sciences Research Council.

Above all else, I would also like to thank mum, dad, Maddie and my family, for everything and more. My parents have always supported me, I could not be more appreciative of the hours they spent driving me to music lessons and engineering experience days, practising interviews, sitting through engineering talks I'm sure they found dull and just providing the best family environment I could ever have asked for. Without them I would never have made it this far and I doubt I will ever be able to thank them enough for what they have done.

To my girlfriend Maddie, you have been there for me every step of this journey and I hope that you know how much I appreciate you. From talking for hours about my work and our plans, always being excited for me and proud of me, putting up with me, teaching me so much, being my rock in lockdown and so much more. Thank you for everything you do and everything we will do together in the future.

The past 4 years have been a whirlwind and I have loved every minute of it. The fit I had with the project, stage of technology, supervisor and institution couldn't have been better. From getting stuck into long days the lab, seeing surgeries with Alex and Justin in the operating room, discussing orthopaedics and engineering with JJ, design, manufacturing and testing implants and getting all of the support to begin a start-up, it's been perfect. Recently I have come to realise just how extremely grateful I am for the mentors I have been able to learn from and hope I will continue to do so.

I have learned so much during my PhD and am completely grateful for the opportunities I have had - most of all the opportunity to build a company from the ground up.

Contents

Contents VIII

List of Figures XIV

List of Tables XVIII

1 Introduction 1
- 1.1 Motivation . . . 2
- 1.2 Aims and Objectives . . . 2
- 1.3 Structure . . . 3
- 1.4 Bibliography . . . 5

2 Literature Review 9
- 2.1 Clinical Background . . . 10
- 2.2 Osteoarthritis in the Knee . . . 10
  - 2.2.1 A History of Knee Arthroplasty . . . 12
- 2.3 Remodelling of Bone . . . 13
  - 2.3.1 Mechanisms of Remodelling . . . 14
  - 2.3.2 Strain Response . . . 16
- 2.4 Variation in Bone Properties . . . 18
  - 2.4.1 Mechanical Property Mapping and Prediction . . . 18
  - 2.4.2 Spatial Variation . . . 19
  - 2.4.3 Mechanical Anisotropy . . . 22
  - 2.4.4 Structural Anisotropy . . . 22
- 2.5 Additive Manufacturing and Biomimetic Design . . . 24
  - 2.5.1 A background on Additive Manufacturing . . . 24
  - 2.5.2 Applications of Additive Manufacturing . . . 25
  - 2.5.3 Fatigue Life of Porous Implants . . . 26

2.5.4 Improvements in surface area 26
2.6 Clinical Applications of Porous Materials 27
2.6.1 Osseointegration 27
2.6.2 Stress shielding 28
2.7 Rationale and review of experimental approaches used 29
2.7.1 Chapter 3: Prediction and characterisation of bone's properties 29
2.7.2 Chapter 4: Characterisation and control of lattice modulus and anisotropy 31
2.7.3 Chapter 5: Application of lattices for fine control of bone strains 31
2.7.4 Chapter 6: Demonstration of the technology in partial and total knee implants 32
2.8 Summary 33
2.9 Bibliography 34

3 Mapping Mechanical Properties in the Tibia 51
3.1 Introduction 52
3.2 Material and Methods 53
3.2.1 Sample Preparation 53
3.2.2 Quantifying Bone Density from CT Scan 55
3.2.3 Specimen Testing 55
3.2.4 Statistical Analysis and Model Fitting 57
3.3 Results 57
3.3.1 Mechanical Data for Apparent Modulus and Strength 57
3.3.2 Apparent Modulus 58
Analysis of variance 58
Regression Modelling: All test directions by subchondral depth 59
Regression Modelling: Z direction by subchondral depth and condyle 61
3.3.3 Yield Strength 63
3.4 Discussion 64
3.4.1 Summary of Results 64
3.4.2 Comparison to Literature 65
3.4.3 Considerations 68
3.4.4 Clinical Significance 69
3.4.5 Conclusion 69
3.5 Bibliography 70

4 Predicting Anisotropy in Porous Materials 77
4.1 Introduction 78
4.2 Material and Methods 79
4.2.1 Specimen Design and Manufacture 79

Stochastic Structure 79
Rhombic Dodecahedron Structure 80
Structure Orientation 80
4.2.2 Calculation of Fabric Tensors and Fitting of Predictive Model 81
4.2.3 Mechanical Measurement of Anisotropic Properties 83
4.3 Results 85
4.3.1 Stochastic Lattice Results 85
4.3.2 Rhombic Dodecahedron Lattice Results 89
4.4 Discussion 92
4.4.1 Summary of Results 92
4.4.2 Comparison to Literature 93
4.4.3 Considerations 94
4.4.4 Clinical Significance 95
4.5 Conclusion 95
4.6 Bibliography 95

5 Implants that Generate Remodeling Strains in Bone 101
5.1 Introduction 102
5.2 Materials and Methods 103
5.2.1 Bone property measurement and prediction 103
5.2.2 Titanium Lattice 103
Structure Generation 103
Control of Lattice Anisotropy 104
Characterising Lattice Mechanical Properties 104
Mechanical Testing of Bone-Lattice Pairs 105
FE Modelling 106
5.3 Control of Bone Strain 107
5.4 Control of Lattice Anisotropy 110
5.5 Discussion 110
5.5.1 Summary of Results 110
5.5.2 Comparison to Literature 111
5.5.3 Considerations 112
5.5.4 Clinical Significance 113
5.6 Conclusion 113
5.7 Bibliography 113

6 Implants that Maintain Native Tibial Load Transfer 119
6.1 Introduction 120
6.2 Methods 121
6.2.1 Implant Design and Manufacture 121
6.2.2 Surgical Planning and Specimen Preparation 122
6.2.3 Knee loading 123
6.2.4 Analysis of Data 125

6.3 Results . . . 125
6.3.1 UKA Results . . . 125
Stress Distribution . . . 125
Maximum induced stress . . . 127
6.3.2 TKA Results . . . 127
Stress Distribution . . . 127
Maximum induced stress . . . 130
6.4 Discussion . . . 131
6.4.1 Summary of Results . . . 131
6.4.2 Comparison to Literature . . . 131
6.4.3 Considerations . . . 132
6.4.4 Clinical Significance . . . 133
6.5 Conclusion . . . 133
6.6 Bibliography . . . 133

7 Overall Discussion **139**
7.1 Most Important Findings . . . 139
7.2 Advancement of the Field . . . 139
7.2.1 Prediction and characterisation of bone's properties . . . 139
7.2.2 Characterisation and control of lattice modulus and anisotropy 139
7.2.3 Application of lattices for fine control of bone strains . . . 140
7.2.4 Demonstration of the technology in partial and total knee implants . . . 140
7.3 Translational Opportunity . . . 140
7.4 Future work . . . 142
7.4.1 Technical Limitations . . . 142
7.5 Conclusions . . . 143
7.6 Bibliography . . . 144

A Appendix A **147**
A.1 Appendices to Chapter 3 . . . 147
A.2 Appendices to Chapter 4 . . . 149
A.3 Appendices to Chapters 5 and Chapter 6 . . . 150

List of Figures

2.1 Definitions of compartmental knee osteoarthritis 13
2.2 Bone has a complex hierarchical structure which is dependant on many factors. 14
2.3 Bone remodelling at a cellular level 15
2.4 Bone remodelling is dependent on amplitude and frequency of loading 16
2.5 Bone remodelling is regulated by states of disuse and overuse. 17
2.6 Bone resorption in knee arthroplasty 18
2.7 A comparison of models for bone apparent modulus from literature . . 19
2.8 Variation of apparent modulus across the human proximal tibia 20

3.1 Summary of methods for measurement of bone density from computed tomography (CT) scans. 54
3.2 Example stress-strain traces for multiaxial sample testing. 56
3.3 Multiaxial apparent modulus with subchondral depth. 60
3.4 Multiaxial apparent modulus with subchondral depth correlated with bone density. 61
3.5 Medial and lateral axial apparent modulus. 62
3.6 Medial and lateral axial apparent modulus correlated with bone density. 63
3.7 Multiaxial yield strength against apparent density. 64
3.8 Comparison of data with existing literature. 66

4.1 Manufacture of titanium stochastic structures for testing directional properties. 81
4.2 Summary of data extracted from CAD strut vectors. 82
4.3 Typical load-displacement curve for a stochastic titanium structure. . . 84
4.4 Model predictions for titanium stochastic structure anisotropic apparent modulus. 87

4.5 Model predictions for titanium stochastic structure anisotropic peak strength. 88
4.6 Peak strength against apparent modulus for titanium stochastic structures. 89
4.7 Model predictions for nylon rhombic-dodecahedron structure anisotropic apparent modulus. 90
4.8 Model predictions for nylon rhombic-dodecahedron structure anisotropic peak strength. 91
4.9 Peak strength against apparent modulus for nylon rhombic-dodecahedron specimens. 92

5.1 Mechanical parallel compression testing set up. 105
5.2 Tekscan pressure sensor decay. 106
5.3 Induced strain response of bone as a function of change in lattice implant modulus. 107
5.4 Relative stress induced in bone as a function of change in lattice implant modulus. 108
5.5 Stress distribution across the surface of bone cubes correlated with density distribution across the bone cube surface. 109

6.1 Summary of the methods for planning surgeries, preparing and testing cadaveric specimens. 123
6.2 Test setup and constraining of the knee 124
6.3 Bone-implant interface stress distribution in UKA. 126
6.4 Maximum bone-implant interface stress in UKA. 127
6.5 Bone-implant interface stress distribution in TKA. 129
6.6 Maximum bone-implant interface stress in TKA. 130

A.1 Tekscan pressure film equilibration fixture. 151

List of Tables

2.1 A summary of literature on the apparent modulus of trabecular bone in the proximal tibia. 21

3.1 Summary of the 7 donors and extracted cores. 55
3.2 Summary of the calculated apparent density and measured apparent moduli for all cores. 57
3.3 Observed apparent modulus for each test direction. 58
3.4 Statistical significance and effect sizes for each group factor on each target variable. 59
3.5 Comparison of power-law models found in literature to the data observed here. 66

4.1 Spherical coordinates of structure test directions. 81
4.2 Summary of specimen build direction, density, fabric and mechanically tested apparent modulus and peak strength data. 85
4.3 Parameters defining prediction models for both apparent modulus and strength of the stochastic lattice and the rhombic dodecahedron lattice. 86
4.4 Summary of existing models for apparent modulus prediction in literature 93

5.1 Induced bone strain for bone cubes and each corresponding lattice. . 108
5.2 Induced bone stress for bone cubes and each corresponding lattice when loaded to 1 kPa. 109
5.3 Bone-lattice axial modulus variation. 110
5.4 Bone-lattice transverse modulus variation. 111
5.5 Bone-lattice anisotropy variation. 111

6.1 Description of implant variants tested. 121

6.2 Summary of results for UKA implant variants. 127
6.3 Summary of results for TKA implant variants. 131

A.1 Model parameters for power law models for X, Y and Z apparent modulus. 147
A.2 Model parameters for power law models for X apparent modulus data. 148
A.3 Model parameters for power law models for Y apparent modulus data. 148
A.4 Summary of Z apparent modulus data and power-law model parameters for the data. 149
A.5 Model parameters for power law models for strength data. 149

Acronyms

μCT micro computed tomography

μFE Finite Element

3D three-dimensional

AM additive manufactured

AM additive manufacturing

CAD computer-aided design

CT computed tomography

FE Finite Element

GST Gradient Structure Tensor

HU Hounsfield units

MIL Mean Intercept Length

qCT quantified computed tomography

RMSE root mean square error

SST Sobel Structure Tensor

1 Introduction

In orthopaedics, implants have traditionally been machined, forged or cast solid pieces of metal to meet high strength requirements, but this means they are orders of magnitude stiffer than natural bone [1]. Bone response is proportional to load and the use of solid implants reduces the load and strain in the surrounding bone. This means that bone density around implants is reduced over time and can lead to failure of fixation and the resulting bone loss can make revision surgery challenging. Additive manufactured porous structures are now viable choices for the engineer in a variety of fields, particularly in orthopaedics [2–4]. These implants can now be composed of low stiffness architectured porous structures produced by additive manufacturing (AM) [5], from established biocompatible metals like Titanium, Cobalt Chrome, and Tantalum [6, 7]. Orthopaedic devices therefore now have the potential to match the stiffness of cancellous bone throughout the skeleton which may enable new and better treatment options in the management of osteoarthritis and other bone pathologies, particularly for early intervention in young patients. Bone repair and regeneration can be driven by strain response with respect to load, i.e. the more strain, bone experiences due to loading the greater the increase is in bone volume [8–10]. Thus, to accelerate bone regeneration, a porous scaffold or porous coating on an implant should have a stiffness less than the bone that is being replaced, to induce more strain at the defect site [11]. However, maximising strength (unless otherwise stated, strength refers to compressive yield strength hereafter) of AM porous metals at low stiffness remains a challenge, particularly in applications under high cyclic loads [12, 13]. Optimisation of the design and incorporation of AM porous structures into orthopaedic implants provides an opportunity to develop implants which engender homeostatic strains in bone for long term bone maintenance.

The overriding research questions for this thesis are:

- How are the mechanical properties of bone in the proximal tibia distributed and can improved mappings and predictions of such properties allow for design of implants which engender strains to stimulate the homeostatic response?

- Can tibial implants be designed to restore a transfer of load into the proximal tibia which is similar to that in the native tibia?

1.1 Motivation

Osteoarthritis is the most common joint disorder in the world, causing pain and reduced quality of life. It has a growing prevalence both in the UK and globally. In the UK, common orthopaedic treatments are hip and knee replacements, of which 92,000 and 100,000 procedures are done every year, respectively [14]. The average ages of patients undergoing hip and knee replacements are 69 and 70 respectively. 21% of total hip replacement procedures and 14% of total knee replacement procedures are performed on patients under the age of 60. In patients younger than 60 years old 35% of implants fail [15]. Due to the bone loss associated with the use of solid implants, revision and re-revision surgery necessitates the use of larger and more complex implants to achieve stable fixation in the remaining host bone. As a result, there is a limit to the number of revision procedures that can be performed as bone stock diminishes. Because of this, and in spite of the significant impact of osteoarthritis on the quality of life of young, economically active people, there is a reluctance to offer arthroplasty to patients in this age group. There is therefore a wide gap in the treatments available for patients in the 35 to 60 year old age bracket who are considered too old for biological repair, but too young to be considered ideal candidates for joint replacement.

Such patients' bones are healthy and have a very active and functional healing response, meaning surgeons are unlikely to fit a conventional implant. Existing implants are manufactured as solid pieces of metal, with properties vastly different to natural bone, and hinder this natural remodelling process rather than encouraging it. An improved type of implant which harnesses the natural mechanoresponse of bone, controlling response to loading, could create healthy patient biomechanics, preserve the joint and reduce the need for surgical revision.

1.2 Aims and Objectives

The aim of this research is to improve knowledge of how porous AM structures can be applied in orthopaedic applications, to develop load bearing implants which preserve bone and encourage positive bone remodelling. This work will focus first on mapping the relevant properties of bone in a clinically viable workflow and

modelling how porous structures can best replicate native bone. Another focus is to demonstrate that porous implants can improve upon conventional arthroplasty treatments by being designed to invoke a desired mechanobiological response from bone while utlising methods and materials used in industry to maintain compliance with regulation and ease the burden of translating this work.

This thesis details the work aiming to develop an AM tibial component for knee arthroplasty which is mechanically optimised to harness bone's mechanoresponse. This objective presents difficulties spanning many areas of research; including understanding the mechanical properties of bone (Chapter 3), the design of structures (Chapter 4), controlling bone strain with porous structures (Chapter 5) and integrating such structures into orthopaedic implants (Chapter 6).

Implants which are capable of maintaining a native load transfer to surrounding bone could invoke bone's homeostatic response to preserve bone quality long after primary surgery. There are opportunities for this technology to benefit young and active patients, whose bones have a strong remodelling response and implants have longer desired survival times. The growth in global cementless implant usage and pressure on surgeons to use bone preserving techniques provides a strong interest in this work.

Considerations for commercialisation play a key role in this thesis and in some cases help in understanding the rationale for research decisions. It was important that any outputs from this thesis be directly applicable to the processes, methods and materials used in the orthopaedic industry. This includes, but is not limited to, the ability for implants to be manufactured at scale, the stringent requirements of various regulatory systems, input from high volume orthopaedic surgeons and appreciating the compromise often required between idealised function and cost of goods.

1.3 Structure

This thesis presents four self-contained papers in a journal format: one has been published in Advanced Functional Materials, one with the Journal of Additive Manufacturing, one with the Journal of Orthopaedic Research and the last with Bone and Joint Research. Alongside these publications, supplementary material and methods and results are included and discussed. Each paper provides a concise description of the methods and main findings and so is also supported by an extensive set of appendices which describe parts of the method in finer detail, provide supporting sensitivity analyses, describe secondary results which were not included in the paper and provide more extensive verification for some of the key findings. The appendices are numbered to match their accompanying chapter and they are referenced and summarised in the main papers at the most relevant point.

The structure of this thesis is as follows:

- **Chapter 1 - Introduction**
  An introduction to the study and the motivation behind the work. The aims and objectives of the study are presented as well as the structure of the thesis.

- **Chapter 2 - Background**
  A summary of background literature and fundamental topics is presented. Topics covered include: clinical background and an introduction to characteristics of bone, bone remodelling, design for osseointegration in porous structures, effects of osteoarthritis, existing arthroplasty treatments, imaging methods, AM and how implant design may encourage bone growth. A brief introduction to powder bed fusion will be given followed by an overview of research into porous structures, focusing on the role of manufacturing parameters and common biomaterials used as bone implants or scaffolds.

- **Chapter 3 - Mapping Mechanical Properties in the Proximal Tibia**
  It is necessary to understand how the native mechanical environment varies in the proximal tibia. This chapter provides a more detailed mapping of bone apparent modulus and yield strength than seen previously in literature. Furthermore, it demonstrates how improved prediction of these properties is now possible in a clinically viable workflow.

- **Chapter 4 - Predicting Anisotropy in Porous Materials**
  Many examples of porous architecture structures exist in literature, mostly manufactured with repeating cell structures which inherently have hidden axes of minimal compliance predetermined by the unit cell structure. This chapter explores whether anisotropy can be better predicted and controlled in stochastic structures and to what extent this can prove beneficial in stimulating bone remodelling.

- **Chapter 5 - Generating Homeostatic Remodelling Strains in Bone**
  Bone remodeling is mediated by several factors including strain. This chapter explores whether orthopedic implants can be manufactured using clinically established methods can induce homeostatic strains in human bone.

- **Chapter 6 - Knee Replacement Implants that Maintain Native Tibial Load Transfer**
  Conventional monolithic knee replacement implants disrupt bone's natural homeostasis which leads to bone loss over time, causing problems if the implant needs to be revised. This chapter demonstrates that a

manufacturing method already in widespread use can be used to maintain normal load transfer to the bone after partial and total knee replacement.

This thesis represents work from four published research articles (reproduced under the terms of the Creative Commons Attribution License (CC BY)). The following is a breakdown of these papers into the respective chapters and sections:

- **M. J. Munford**, G. K. C. Ng, J. R. T. Jeffers, Adv. Funct. Mater., 30, p. 2004323, 2020, Accessed: Sep. 14, 2020.
  - Chapter 3
- **M. J. Munford**, U. Hossain, S. Ghouse, J. R. T. Jeffers, Addit. Manuf., 32, p. 101041, 2020.
  - Chapter 4
- **M. J. Munford**, D. Xiao, J. R. T. Jeffers, J. Orthop. Res., 2021.
  - Chapter 5
- **M. J. Munford**, J. Stoddart, A. D. Liddle, J. P. Cobb, J. R. T. Jeffers, Bone Joint Res., 2022.
  - Chapter 6

1.4 Bibliography

[1] S. A. Goldstein, D. L. Wilson, D. A. Sonstegard, and L. S. Matthews, "The mechanical properties of human tibial trabecular bone as a function of metaphyseal location," *Journal of Biomechanics*, vol. 16, pp. 965–969, 1 1983.

[2] L. Mullen, R. C. Stamp, W. K. Brooks, E. Jones, and C. J. Sutcliffe, "Selective laser melting: A regular unit cell approach for the manufacture of porous, titanium, bone in-growth constructs, suitable for orthopedic applications," *Journal of Biomedical Materials Research - Part B Applied Biomaterials*, vol. 89B, no. 2, pp. 325–334, 2009.

[3] M. J. Matthews, G. Guss, S. A. Khairallah, A. M. Rubenchik, P. J. Depond, and W. E. King, "Denudation of metal powder layers in laser powder bed fusion processes," *Acta Materialia*, vol. 114, pp. 33–42, 8 2016.

[4] V. J. Challis, X. Xu, L. C. Zhang, A. P. Roberts, J. F. Grotowski, and T. B. Sercombe, "High specific strength and stiffness structures produced using selective laser melting," *Materials and Design*, vol. 63, pp. 783–788, 2014.

[5] P. Heinl, L. Müller, C. Körner, R. F. Singer, and F. A. Müller, “Cellular Ti-6Al-4V structures with interconnected macro porosity for bone implants fabricated by selective electron beam melting,” *Acta Biomaterialia*, vol. 4, no. 5, pp. 1536–1544, 2008.

[6] L. Mullen, R. C. Stamp, P. Fox, E. Jones, C. Ngo, and C. J. Sutcliffe, “Selective laser melting: A unit cell approach for the manufacture of porous, titanium, bone in-growth constructs, suitable for orthopedic applications. II. Randomized structures,” *Journal of Biomedical Materials Research - Part B Applied Biomaterials*, vol. 92, no. 1, pp. 178–188, 2010.

[7] R. Wauthle, J. Van Der Stok, S. A. Yavari, J. Van Humbeeck, J. P. Kruth, A. A. Zadpoor, H. Weinans, M. Mulier, and J. Schrooten, “Additively manufactured porous tantalum implants,” *Acta Biomaterialia*, vol. 14, pp. 217–225, 3 2015.

[8] D. R. Carter and W. C. Hayes, “The compressive behavior of bone as a two-phase porous structure,” *Bone & Joint Research America*, vol. 59, pp. 954–962, 1 1977.

[9] A.-M. Pobloth, S. Checa, H. Razi, A. Petersen, J. C. Weaver, K. Schmidt-Bleek, M. Windolf, A. Tatai, C. P. Roth, K.-D. Schaser, G. N. Duda, and P. Schwabe, “Mechanobiologically optimized 3D titanium-mesh scaffolds enhance bone regeneration in critical segmental defects in sheep.,” *Science translational medicine*, vol. 10, 1 2018.

[10] J. Van Der Stok, O. P. Van Der Jagt, S. Amin Yavari, M. F. De Haas, J. H. Waarsing, H. Jahr, E. M. Van Lieshout, P. Patka, J. A. Verhaar, A. A. Zadpoor, and H. Weinans, “Selective laser melting-produced porous titanium scaffolds regenerate bone in critical size cortical bone defects,” *Journal of Orthopaedic Research*, vol. 31, pp. 792–799, 5 2013.

[11] J. Henkel, M. A. Woodruff, D. R. Epari, R. Steck, V. Glatt, I. C. DIckinson, P. F. Choong, M. A. Schuetz, and D. W. Hutmacher, “Bone Regeneration Based on Tissue Engineering Conceptions-A 21st Century Perspective,” *Bone Research*, vol. 1, pp. 216–248, 9 2013.

[12] X. Wang, S. Xu, S. Zhou, W. Xu, M. Leary, P. Choong, M. Qian, M. Brandt, and Y. M. Xie, “Topological design and additive manufacturing of porous metals for bone scaffolds and orthopaedic implants: A review,” *Biomaterials*, vol. 83, pp. 127–141, 3 2016.

[13] M. Ashby, T. Evans, N. Fleck, J. Hutchinson, H. Wadley, and L. J. Gibson, *Metal Foams: a Design Guide*. Butterworth-Heinemann, 2000.

[14] P. Howard, R. Brittain, S. Lawrence, J. Stonadge, M. Wilkinson, T. Wilton, S. Dawson-Bowling, A. Watts, O. Specialists, R. Craig, C. Esler, A. Goldberg,

S. Jameson, T. Jennison, J. Rees, A. Toms, E. Young, C. Boulton, D. Taylor, O. Espinoza, V. Mccormack, C. Newell, M. Royall, M. Swanson, Y. Ben-Shlomo, A. Blom, E. Clark, K. Deere, C. Gregson, L. Hunt, A. Judge, E. Lenguerrand, A. Price, D. Prieto-Alhambra, A. Sayers, and M. Whitehouse, "National Joint Registry | 17th Annual Report," tech. rep., National Joint registry, 2020.

[15] L. E. Bayliss, D. Culliford, A. P. Monk, S. Glyn-Jones, D. Prieto-Alhambra, A. Judge, C. Cooper, A. J. Carr, N. K. Arden, D. J. Beard, and A. J. Price, "The effect of patient age at intervention on risk of implant revision after total replacement of the hip or knee: a population-based cohort study," *The Lancet*, vol. 389, pp. 1424–1430, 4 2017.

2 Literature Review

This chapter details background knowledge and a brief introduction into the mechanobiology of bone and bone ingrowth into porous scaffolds, alongside the clinical relevance. An overview of how the powder bed fusion additive manufacturing process works is also provided. Theory regarding the behaviour of porous structures will be presented as well as a literature review regarding research into additive manufacturing (AM) porous structures. Literature on common orthopaedic biomaterials are also explored, including research into low stiffness biocompatible metals.

2.1 Clinical Background

The volume of orthopaedic reconstruction procedures to combat osteoarthritis, inflammatory arthritis, metabolic bone disease and other musculoskeletal disorders have increased dramatically, resulting in high demand on the advancement of bone implant technology [1]. Moreover, because of a prolonged life expectancy and an aging world population, there is a rapid increase in musculoskeletal pathologies such as fractures, low back pain, scoliosis, osteoporosis, bone infection or tumours and congenital defects, as well as rheumatic diseases like osteoarthritis. Large bone defects caused by severe fracture, tumour or infection are a challenging issue for the regeneration ability of the body. If the defect exceeds a critical size, bone regeneration cannot be handled by the body's healing process alone and requires supportive therapeutic intervention like autografts, allografts or a synthetic scaffold [2]. Similarly, in the treatment of osteoarthritis of a joint, which is degeneration of cartilage and underlying bone, typically caused by injury, obesity or wear and tear, either a partial or full replacement of the joint by an implant is required. Joint replacements typically involve replacing the articulating surfaces of the joint by metal or ceramic materials, and sometimes with an additional bearing material (polyethylene) acting as the cartilage. Porous metals offer significant benefits in the treatment of these pathologies, due to the mechanisms of bone regeneration and adaptation.

Arthroplasty treatments are commonly used in the knee, hip, shoulder and other joints. With regards to the number of patients treated across knee, hip and spine markets, all three markets are comparable in size [3]. The knee market stands out as unique compared to the hip and shoulder when considering the cause of failures and mechanical environment. In the knee, implant loosening is a leading cause of failure and peri-prosthetic bone loss is a common cause of complication for surgeons [4, 5]. In contrast, loss of bone quality is a lesser issue in the hip and spine and implant failures due to loosening are less common. These considerations are important because porous structures and additive manufacturing technologies are ideally placed to address loosening and bone loss related concerns. Knee arthroplasty is therefore a sensible focus for this research.

2.2 Osteoarthritis in the Knee

Over 10 million people in the UK suffer from musculoskeletal disorders, with Osteoarthritis being the most common. Within this group the disease causes 38% of people to give up work while 76% to feel their family and social life are compromised. Similarly, 31% report their friendships and relationships as being strained due to the effects of the disease [6].

A total of £5 billion is spent every year on all muskuloskeletal disorders, with

£1.2 billion of this spent on 192,000 hip and knee arthroplasty procedures. Of these, 100,000 are knee replacement procedures, consisting of 89% total knee arthroplasty (TKA), 10% unicompartmental knee arthroplasty (UKA) and 1% bi-unicompartmental knee arthroplasty (bi-UKA). In patients who have undergone knee arthroplasty, the lifetime risk of revision is 38% in those younger than 60 and only 5% in those older than 70 [7].Furthermore, in the UK it is common for patients under the age of 65 to wait 7-10 years before having surgery [6]. The discussion between TKA and UKA is growing. TKA does have good outcomes with around 5% survivorship at 10 years and good overall improvement, however, UKA has many advantages including lower morbitity, shorter hospital stays, greater cost-effectiveness and only removing bone at the site afflicted by osteoarthritis [8].Many surgeons argue that, regardless of the stage of osteoarthritis, TKA is suitable for most patients because 60% of patients with single compartmental osteoarthritis go on to develop it in a further compartment. Many surgeons prefer UKA as a treatment in such a case, with the knowledge that it can be converted to a TKA or bi-UKA if needed.

Osteoarthritis is the most common joint disorder in the world, causing pain and reduced quality of life. It has a growing prevalence both in the UK and globally [3, 6]. Knee osteoarthritis is a degenerative disease resulting in the damage and loss of the articular cartilage between the bones of the tibia and femur. This reduces the cushioning effect of cartilage, which can lead to reduced ease of motion, stiffness and pain. As we get older cartilage takes a longer time to heal so it is not surprising that the most common indicator for knee osteoarthritis is age. Osteoarthritis is most common in people over the age of 45 and is more prevalent in women than men [6]. Risk of osteoarthritis is also increased in those who are overweight [6].

Advances in arthroplasty technologies and materials has seen the causes of UKA revisions change in the past 20 years. Today, 35% of UKA revisions are performed due to aseptic loosening, while 20% are performed due to progression of arthritis and 9.3% are performed due to misalignment [4]. When stratifying data between early revisions are late revisions (before and after 5 years post-operation respectively) it is seen that 24.1% of late UKA revisions are due to aseptic loosening [9, 10]. An interesting trend can be seen in the percentage of revisions performed due to polyethylene wear, which has reduced from 9.3% to 3.2%, this is indicative of improvements in implant materials and cross-linked polyethylene [4].

Cost of revision is an important consideration in surgery and implant development. Total costs (including implant, supply and hospital costs) vary between territories, for example the average cost of a revision TKA in the USA is $49,630, compared to $16,243 for a primary TKA and $11,397 for a primary UKA [11, 12]. Of these total costs, the average unit cost (implant, cement and hospital stay post surgery)

of a UKA in the USA is $3448 compared to £2514 in the UK [12, 13]. Similarly, the average unit cost of a TKA in the USA is $5006 compared to £4280 in the UK. In the UK, the average unit costs of performing revision TKA are £6674 and £10,383 given a primary UKA and TKA respectively [13]. Revision TKA due to infection typically costs 25% more than revision due to loosening [14].

2.2.1 A History of Knee Arthroplasty

In the 1960s Freeman and Swanson in London and Insall and Walker in New York, USA contributed to the development of the condylar knee replacement through the use of a cobalt-chrome femoral prosthesis articulating with a high density polyethylene tibial tray. This permitted rotation of the knee as well as 90 degrees of flexion. The Freeman-Swanson ICLH knee prosthesis was the first to be subject to a multi-centre trial. In the 80s, Freeman and Samuelson modified the ICLH prosthesis by displacing the tibial articular surface posteriorly and decreasing the size of the posterior tibial lip to allow a greater deal of flexion [15].

Total knee arthroplasty, however, is not the only surgical treatment for patients with severe knee osteoarthritis. Unicompartmental knee replacements can be performed on patients as an alternative treatment to total knee arthroplasty. Indeed, 83% of patients do not have osteoarthritis in all three compartments of the knee so would be more suitable for unicompartmental knee replacement [16].

Unicompartmental knee replacement is a much smaller operation than total knee arthroplasty and involves less bone being removed; by preserving healthy joint surfaces and cruciate ligaments, unicompartmental knee replacement restores more normal kinematics and gives better high level function. As a smaller operation, it has a lower rate of early complications such as infection, venous thromboembolism and medical complications of surgery [4]. Surgical techniques for knee arthroplasty are constantly evolving in order to increase effectiveness of the implant and reduce the post-operative recovering period. This results in a shorter recovery period and can lead to more mobility in the knee post-operatively [17]. Partial knee replacements can replace the medial or lateral compartment of the knee, or the trochlea groove (Figure 2.1). Multiple replacements can be combined to replace multiple components of the knee which has disease. The benefit of this is that soft tissues are preserved so that more natural kinematics and gait are maintained compared to total knee replacement [18].

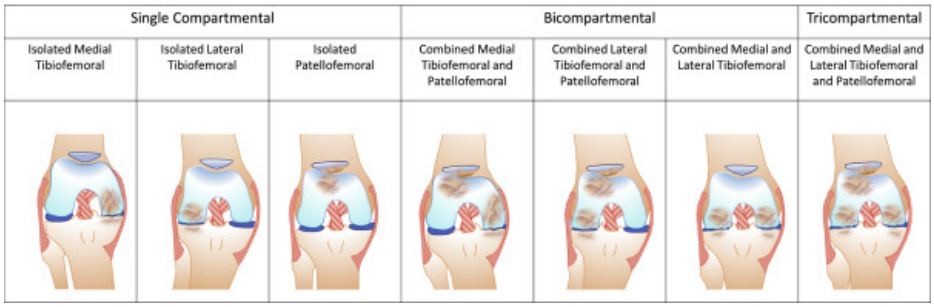


Figure 2.1: Definitions of compartmental knee osteoarthritis Single compartmental osteoarthritis (OA) includes-isolated medial tibiofemoral, isolated lateral tibiofemoral, isolated patellofemoral OA; bicompartmental OA includes-combined medial and lateral tibiofemoral, combined medial tibiofemoral and patellofemoral, combined lateral tibiofemoral and patellofemoral OA; and tricompartmental OA is when disease is located in all three compartments [16].

Common materials in knee arthroplasty include titanium alloys, cobalt-chromium alloys, PEEK and oxidised Zirconium ceramics. Titanium alloys are most commonly used (including Ti-6Al-4V). A growing trend in arthroplasty is to reduce the content of potentially allergenic metal materials, including Vanadium and Nickel, because of growing concerns over metal ion and metal allergenic response [19, 20]. This is a growing argument for the use of commercially pure titanium, non-cobalt-chromium alloys, polymers and ceramics.

2.3 Remodelling of Bone

Bone is a complex three-dimensional porous composite structure with a highly organised internal architecture (Figure 2.2). It serves two critical mechanical functions: providing a rigid skeletal framework to support and protect the internal organs and facilitating movement.

An important function of trabecular or cancellous bone in human joints is to distribute the large contact stresses applied at the articular surfaces to the compact bone of the cortical shafts. Indeed, the trajectorial theory of bone architecture, states that the trabeculae are organised along the lines of principal stresses [22]; with the structure and strength of trabecular bone being a function of these stresses. Trabecular bone also possesses very specific viscoelastic and anisotropic characteristics, both in morphology and mechanical properties. The unique mechanical performance of bone is characterised by high toughness, high specific strength, low stiffness and arguably most importantly, its ability to heal, i.e. bone remodelling and adaptation [23].

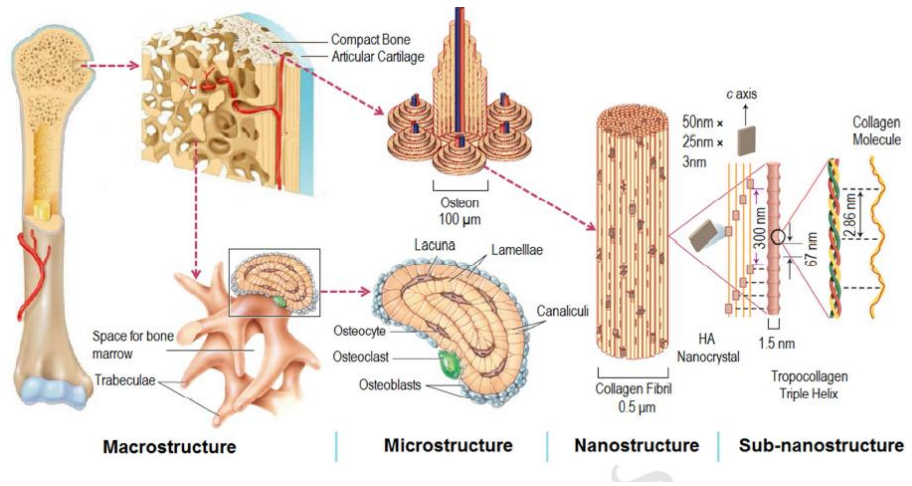


Figure 2.2: Bone has a complex hierarchical structure which is dependant on many factors. Bone's tissue has the natural ability to repair itself. Its mechanical properties vary significantly with age, anatomical site and bone quality [21].

2.3.1 Mechanisms of Remodelling

In 1892, Julius Wolff (a German scientist and anatomist) published his law on bone remodelling [23]. Although 'Wolff's law' was originally formulated in a strict mathematical sense that has since been discredited, the more general concept of 'bone functional adaptation' to mechanical loading is supported by much experimental and observational data [24].

It is likely that osteocytes (bone cells) respond to bone tissue strain by recruiting osteoclasts to sites where bone remodelling is required [25]. Indeed, there are both theories (e.g. Wolff's Law, Perren's strain theory, Frost's "mechanostat" etc. [23, 26, 27]) and experiments that corroborate the effect of mechanical loads and strain on bone adaptation [28, 29]. Adaptation and remodelling is hypothesised to optimise the stiffness and strength of bones, while minimising the metabolic cost of maintenance, ensuring that animal skeletons are continuously adjusted to control strain [29]. It must be noted that bone remodelling is a complex biological process not only dependent on functional (mechanical) requirements but also genetic, hormonal, metabolic and age-related factors as well (Figure 2.3).

Bone continually undergoes dynamic biological remodelling, the coupled process whereby osteoclasts (bone-resorbing cells) remove mature or damaged bone tissue followed by osteoblasts (bone-forming cells) that generate new bone to maintain healthy homeostasis of bone [30, 31]. This unique feature of bone underpins its ability to remodel itself to repair damage, reducing the risk of

fracture, whilst being able to adapt to its mechanical environment [29]. Bone therefore adapts to mechanical stimulus by formation under high loading and by resorption under disuse (or less than habitual loading [32]).

Osteoblasts and osteoclasts can form and resorb bone only at free bone surfaces. The foamy structure of trabecular bone provides ample surface and easy access for bone cells. Osteoclasts dig a roughly circular tunnel with a diameter of approximately 300 μm into the bone and, in their wake, osteoblasts are filling this tunnel with new bone material. In this way, a cylindrically shaped osteon is formed. Remodeling is a rather slow and local process. Trabecular bone resorption can take weeks and formation can even take months [33]. Although the exchanged volume in a remodeling event is rather small, the large number of remodeling events running in parallel leads in trabecular bone to a remodeled volume of 20% of the total volume each year [34].

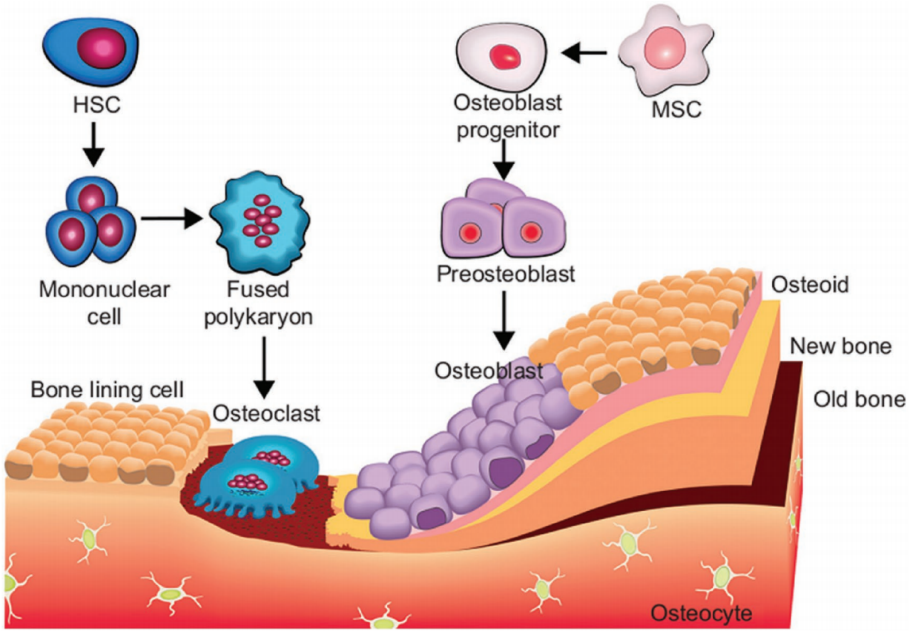


Figure 2.3: Bone remodelling at a cellular level Evolution of osteoblasts and osteoclasts in bone formation. [35]

To allow for an adaptation of the bone structure to changes in the mechanical loading, a mechanosensor has to have a controlling role in bone remodeling. Although the sensing mechanism is still debated, there is general agreement that osteocytes play a key role in bone mechanosensation [25]. Osteocytes are differentiated osteoblasts and are the most abundant bone cells. They live inside the mineralized bone matrix and connect with their multiple cell processes to other

cells to form a cell network. This cell network is housed in a fluid-filled porous network. A prominent theory of bone-mechanosensation is that mechanical loading on the bones induces a fluid flow through the porous network causing shear forces detected by osteocytes [36, 37]. Alternatively, it has been proposed that microdamage itself is the trigger of bone remodeling by disrupting some of the cell processes [38]. This disruption would lead to the death of osteocytes and the missing signal of the osteocyte would bring osteoclasts and osteoblasts to the scene [39].

2.3.2 Strain Response

Bone healing is stimulated by strain response and is dependent on both strain magnitude and cyclic frequency, as in Figure 2.4 [40].

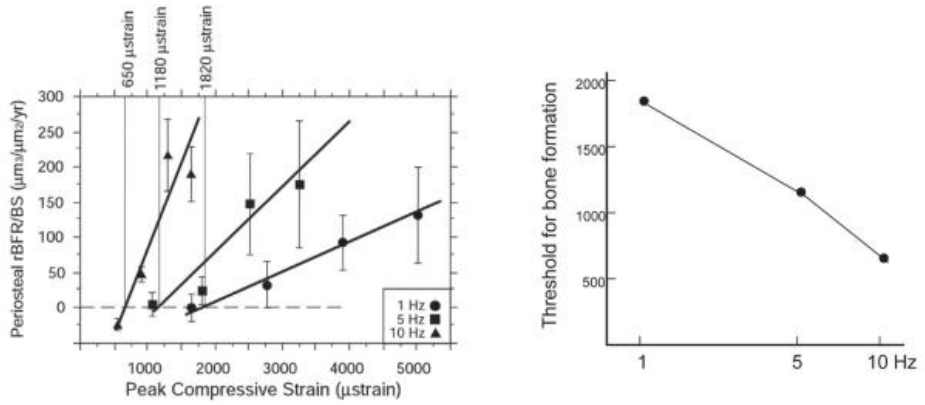


Figure 2.4: Bone remodelling is dependent on amplitude and frequency of loading The graph on the left shows dose-response curves for the bones' response to mechanical loading at 1 cycle/sec (Hz), 5 Hz, and 10 Hz.13 The y-axis is average bone formation rate and the x-axis is the peak strain engendered in the bone tissue. (Right) The graph on the right shows the minimum strain needed to initiate bone formation. This value is 1820 microstrain at 1 Hz but drops to 1180 microstrain at 5 Hz and to only 650 microstrain at 10 Hz.

Mechanical loading has profound influences on bone remodeling. Disuse or lack of loading causes an acceleration of bone resorption with bone resorption overwhelming bone formation resulting in a rapid loss of bone mass. Overuse of bone can cause small cracks or focal damage within the tissue, which in turn stimulates bone remodeling as a reparative process. One of the important roles of bone turnover is to continuously replace and repair damaged bone tissue. Osteoclasts target microcracks within bone tissue preferentially and remove compromised bone tissue [38]. The damaged tissue is then replaced by new

bone tissue. If damage accumulates faster than the tissue can be repaired, larger microcracks develop and propagate to form a stress fracture.

The increased number of bone remodeling sites with disuse or overuse is preceded by programmed cell death in osteocytes [41]. The mechanisms that initiate osteocyte death (apoptosis) are not well understood but may include direct damage to osteocytes via microcracks in the bone matrix or lack of convective fluid flow during disuse. Prolinerich tyrosine kinase 2 (Pyk2) must be activated before osteocyte apoptosis will occur [42]

The effects of loading on bone remodeling follows a U-shaped curve whereby resorption is increased in disuse (insufficient loading) or overuse (overloading causing damage), Figure 2.5. There is a range of loading within which bone remodeling is minimised. This is often called the physiological range [40]. Periosteal bone formation, on the other hand, steadily increases with increased loading, indicating that the mechanisms controlling the growth and reshaping of bones differ from those controlling of bone remodeling.

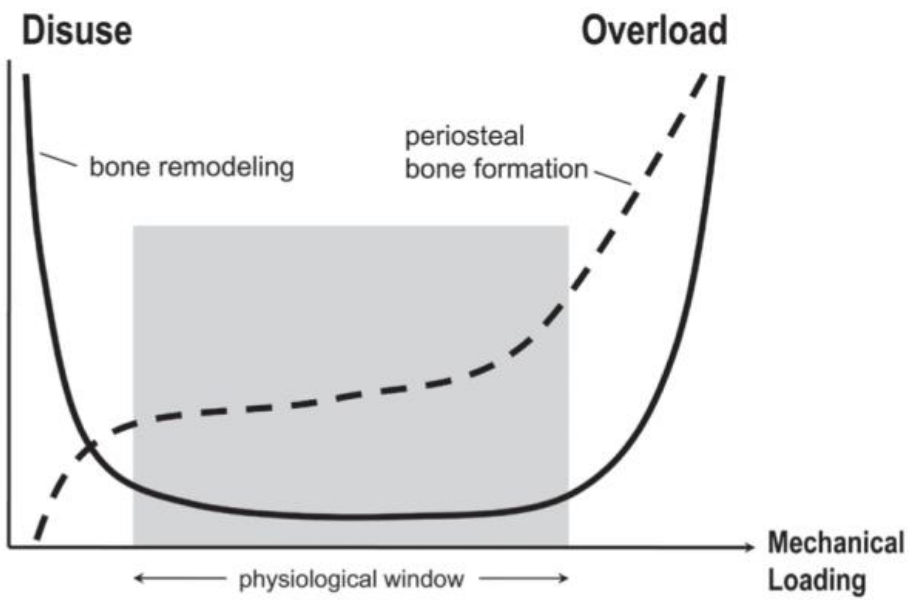


Figure 2.5: Bone remodelling is regulated by states of disuse and overuse. A physiological window falls between the extreme loading conditions, in which bone turnover is low. Bone formation at the periosteal bone surfaces is also affected by mechanical loading, but the relationship is different. Periosteal bone formation is very low in states of disuse and increases with increasing mechanical stimulus. Reprinted from Robling et al. [40],18 Annual Review of Biomedical Engineering.

Bone resorption due to disruption in bone remodelling around implants can manifest itself as reduced bone density (Figure 2.6).



Figure 2.6: Bone resorption in knee arthroplasty Grade 1 (left): Resorption to the level of the baseplate (including any prior uncovered bone) up to 50% of the width of the tray. Grade 2 (middle): Resorption beyond 50% but not to the keel. Grade 3 (right): Resorption to/beyond the level of the keel [5].

2.4 Variation in Bone Properties

Consideration of the spatial variation in bone's properties is important in the design of implants which manipulate bone remodelling to maintain bone density. Many properties vary throughout bone's anatomy, the principal properties explored here are apparent modulus and strength and their anisotropy because these have a significant affect on bone's strain and remodelling response.

2.4.1 Mechanical Property Mapping and Prediction

Numerous prior studies have reported power law relationships between bone density and apparent modulus but these report inconclusive and conflicting models. The power law relationships of seven previous studies in Figure 2.8 indicate a broad range of apparent modulus prediction for a given density [43]. These predicted the apparent modulus value with R^2 correlation coefficients between 0.53 and 0.57 and root mean square error (RMSE) between 106 MPa and 5,500 MPa. These seven previous studies indicate that factors which cannot be detected in computed tomography (CT) scans, such as bone collagen content, gait and diet affect these properties. Bone apparent density, trabecular volume, modulus, strength and strain energy are all affected by medication [44]. Furthermore, bone's ability to remodel changes with protein content and age, as osteocytes become senescent, which is likely to further contribute to the variation in properties observed in the data here [45].

Previous studies have suggested that the mechanical properties of bone vary between males and females [46, 47]. It is noted that many factors not explored in this research also affect bone's properties. One key factor is that of the menopause in women in an age range similar to the younger portion of arthroplasty patients focus on in this research [48, 49]. In such cases, bone modulus and strength can be even lower than otherwise reported, leading to a greater risk of fracture and resorption.

It is noted that the majority of models in literature suggest a power-law with an exponent greater than 1, whereas the majority of models which have been fit here have an exponent less than 1. Porous material theory suggests that power-law relationships with an exponent less than 1 is indicative of axial deformation being dominant over bending deformation [22, 23].

Relationships of the yield strength of bone based on apparent density have not been documented extensively in literature, however, the range of values observed for strength are consistent with those recorded by Goldstein et al. [22].

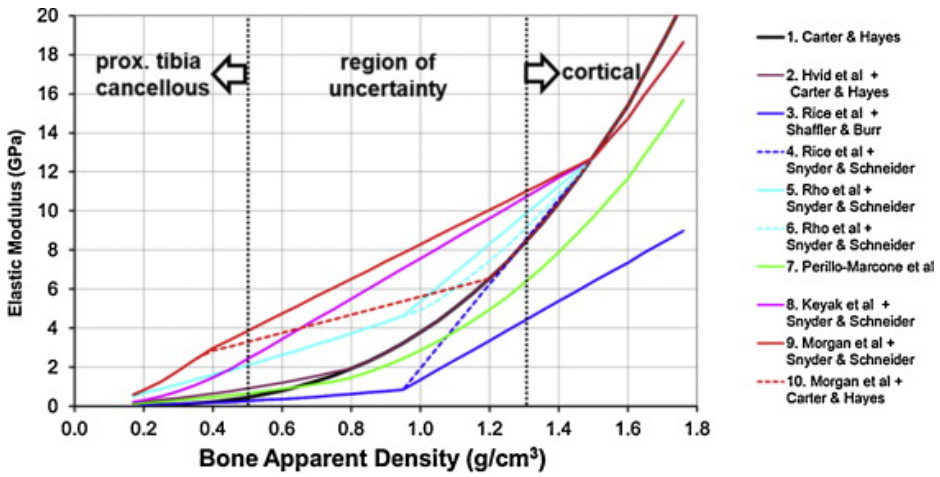


Figure 2.7: A comparison of models for bone apparent modulus from literature Many models exist to determine bone's modulus from apparent density, with vast variation in their predictions. Reproduced with permissions [43].

2.4.2 Spatial Variation

Relatively few studies have mapped cancellous bone apparent modulus and strength differences in regions across the tibia. Studies by Hvid and Hansen, Goldstein et al., Klever et al. and Ashman et al. observed modulus changes across the proximal tibia and these also found increased modulus in the medial condyle. The trends observed here suggest that the ratio of peak medial to lateral

modulus ranges from 1.1 at the most proximal slice to 1.8 more distally, with a mean ratio of 1.3. This agrees with literature values for peak medial-lateral ratio (averaged over all depths) of 1.7 [22, 50], 1.1 [51] and 1.4 [52]. Odgaard et al. observed an increase in strain response for bone more proximal in the tibia, which agrees with trends observed here [53]. Similarly, Goldstein et al., Klever et al. and Ashman et al. also imply a decrease in axial apparent modulus moving distally, but to a lesser extent as was found in this study.

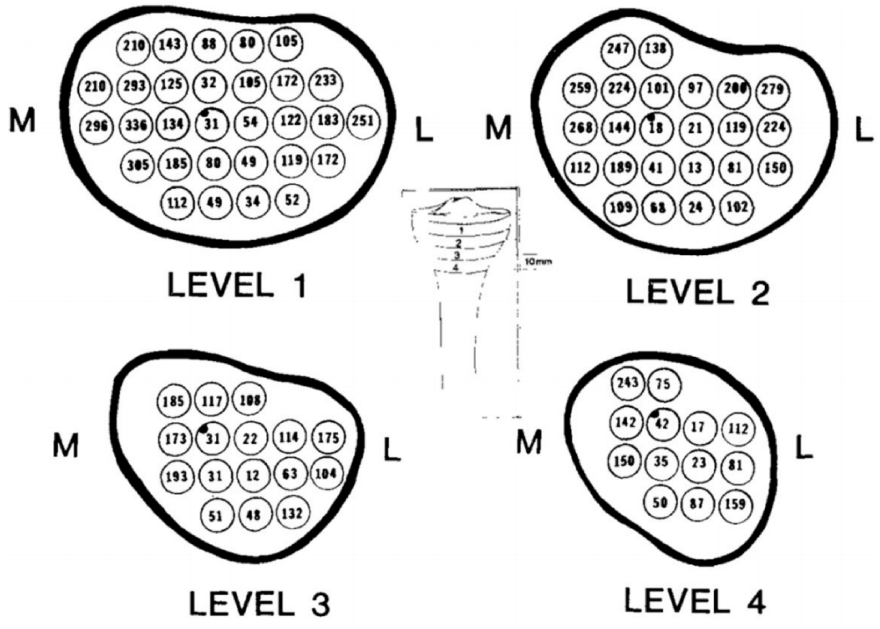


Figure 2.8: Variation of apparent modulus across the human proximal tibia
Image reproduced with permission of the rights holder, Elsevier [22].

Axial apparent modulus of the proximal tibia has been recorded by numerous authors with values ranging from 2.5 - 3780 MPa, as per Table 2.1 [54, 55]. The range of apparent modulus values recorded in this study are well supported by those in the similar studies in literature summarised in Table 2.1). It is noted that a number of studies, such as Garg and Walker, Goldstein, Hvid and Jensen and Lindahl et al., report apparent modulus to be significantly less that that mean predictions across studies in Table 2.1 [55–57]. Similarly, studies such as those from Odgaard and Linde, Keveany et al. and Ashman et al. report apparent modulus values which are significantly greater than those shown here [52, 54, 58]. These values may be larger due to differences in experimental method, small samples sizes of predominantly young males or inclusion of cortical bone regions within cores. Studies such as those by Johnston et al., Nazemi et al. and Ashman

et al. have found apparent modulus from alternative methods such as indentation testing, Finite Element (FE) combined with neural networks or ultrasound testing.

Table 2.1: A summary of literature on the apparent modulus of trabecular bone in the proximal tibia. Where possible, apparent modulus as a function of density and multiaxial properties are shown. *: additional displacement sensors were not used to mitigate compliance effects.

Author	Year	E(ρ)	Modulus Mean (Range) [MPa]		
			Z	X	Y
Ashman et al [52]	1989		1107 (340-3350)	347 (110-1230)	457 (140-1750)
Bentzen et al [59]	1987	35.5 $\rho^{1.7}$	400 (5-2000)		
Carter and Hayes [60]	1977	3790 ρ^{3}	360 (10-500)		
Ciarelli et al [61]	1991		520 (50-1100)	432 (10-900)	280 (5-552)
Garg and Walker* [56]	1968	0.00093 ρ_{CT}^{2}	120 (10-310)		
Goldstein et al* [22]	1983		150 (4-430)		
Hvid and Jensen [57]	1984		96 (31-308)		
Hvid and Linde et al [62]	1989	10256 ρ2.5	506 (113-1226)		
Johnston* [63]	2011		520 (124-820)		
Keaveny et al [54]	1993		2380 (605-3780)		
Klever et al [51]	1985	4100 ρ1.5	970 (293-1667)	434 (11-952)	427 (161-957)
Lindahl et al* [55]	1976		29 (2.5-103.6)		
Linde et al [64, 65]	1991-92	Various	276 (80-1226)		
Linde et al [66]	1990	1012 $\rho^{1.13}$	267 (67-734)	83 (18-493)	84 (18-481)
Morgan et al [67]	2003	15520 $\rho^{1.93}$	860 (200-2700)		
Nazemi et al [68]	2017		250 (10-420)		
Odgaard et al [53]	1989		428 (103-1058)		
Odgaard and Linde [58]	1991	0.029 $\rho^{1.87}$	689 (108-1637)		
Rice et al [69]	1988	1.1 ρ^{2}	(1-20)		
Rincon-Kohli et al [70]	2009		598 (105-1310)		
Tabor et al* [71]	2007		280 (80-410)		
Williams and Lewis [72]	1982	1.5x10^{9} VF	220 (8-475)	67 (8.3-130)	51 (9-84)

2.4.3 Mechanical Anisotropy

Most previous studies have assumed isotropic properties for bone [73], however. Works by Williams and Lewis, Klever et al., Linde et al., Ciarelli et al. and Ashman et al. have also quantified orthogonal properties of the proximal tibia [51, 52, 61, 66, 72]. All such studies, apart from that by Rincon-Kohli et al., suggest an orthotropic modulus. In previous work, apparent modulus in the transverse directions is reported between 51 and 553 MPa with a degree of anisotropy ranging from 1.1 to 4.3 which is not analysed for variation across the tibial plateau.

2.4.4 Structural Anisotropy

Other examples of analysis of anisotropy in the proximal tibia have utilised Finite Element (μFE) and fabric methods with results for average anisotropy between 1.3 and 2.8 [74–77]. Concerning fabric based methods in literature, some authors suggest that anisotropy in mechanical properties of bone correlate with micro computed tomography (μCT) derived fabric tensor data [78, 79].

Authors such as Chaffai et al. and Gdyczynski et al. provide examples of how image processing and filter techniques can be used to determine fabric from bone [80, 81]. Kersh et al. build upon their findings and modelled bone as fabric and compared the use of Mean Intercept Length (MIL), Gradient Structure Tensor (GST) and Sobel Structure Tensor (SST) for this purpose [82]. Kersh et al. identified that a second order fabric tensor, which can be considered as an ellipsoid with axis equal to the tensor eigenvectors, describes the degree of material preference along a particular direction.

MIL is the current gold standard for determining material fabric and Kersh et al. highlights errors between determining the principal direction of fabric based on MIL and GST [82]. It can be noted that the error in GST direction is significantly greater for clinical CT scans than for μCT scans due to the decrease in resolution. No improvement was seen in the use of SST. Other authors, such as Larsson et al., concur with Kersh et al. in that the angle between principal direction of GST and MIL is within 30 degrees [82, 83]. The suitability of GST for determining localised stiffness is therefore subjective and application sensitive.

The concept of material fabric helps to model a lattice or trabecular structured material as a bulk material with directional bias in properties. Some authors have made efforts to determine mechanical properties such as stiffness from fabric, most notably Nazemi et al., Moreno et al., Hazrati et al. and Zysset et al. [84–87]. All works on stiffness-fabric relationships stem from Cowin's work which characterised stiffness and compliance tensors in terms of fabric tensors and a number of coefficients. The initial models developed by Cowin require testing to determine a number of Cowin's coefficients [88].

Simplifications based on assumptions about the material in question are necessary to decrease the number of Cowin's coefficients which are necessary, these typically include assuming symmetrical or orthotropic tensors.

Nazemi et al. modelled the fabric properties of bone by mapping a clinical CT scan onto a FE model to determine the degree of anisotropy [84]. The base of their model was, however, existing density stiffness relationships which have certain limitations. Nazemi et al. present a good workflow towards correlating fabric and density to achieve anisotropic stiffness using indentation tests to collect their mechanical data [84]. One limitation of this study is that although the indentation tests are an effective way to test bone in situ, they cannot account for any effects of bone surrounding the test site. This limitation of indentation testing is represented in literature [89].

Both Nazemi et al. and Moreno et al. present an adaptation of Cowin's earlier work on stiffness-fabric relations [68, 85, 90]. Moreno et al. validate their model against FE relationships which use one of the unreliable density-stiffness relationships. This method of validation raises significant questions about the outcomes from this study. In spite of this, Moreno demonstrates a good correlation of MIL and GST fabric which agrees with conclusions made by Kersh et al., even though only μCT data is used.

Zysset et al. compare models with various conditions and assumptions imposed on the underlying Cowin's equations [79]. Zysset compares isotropic, orthotropic and anisotropic models made by Yang et al., Turner-Cowin and Zysset-Curnier [79]. For validation Zysset utilises third party data, collected from numerical, mechanical and ultrasound techniques. As explained previously, data from numerical techniques should be neglected and ultrasound data is invalid for a large proportion of the density domain which is being tested, only one subset of data (from Goulet et al. which contains mechanical data for a number of anatomical sites including the proximal tibia and distal femur [91]) is therefore relevant to the planned work in this project.

Zysset et al. provide a comprehensive method in their adaptations of Cowins equations for each model and conclude that assuming orthotropy when combining volume fraction and fabric provides a good approximation for experimental data.

An alternative method of determining local fabric from clinical CT scans was provided by Marangalou et al. who use a statistical model to match a clinical CT to its closest approximation in a database of μCT images [86].

2.5 Additive Manufacturing and Biomimetic Design

2.5.1 A background on Additive Manufacturing

AM, the process of joining materials to make objects from three-dimensional (3D) model data, typically layer-by-layer as opposed to traditional subtractive manufacturing methods, emerged in the late 1980s and has matured rapidly in recent years [92]. During the development stage in the 1990s, 3D printing was mostly used for rapid prototyping of polymer and thermoplastic materials. However, advancements in laser and electron beam technologies enabled the fabrication of metallic components. Over the years 3D printing progressed from rapid prototyping to rapid manufacturing of end-use and functional metallic parts [93].

The advantage of AM over conventional subtractive or forming methods is demonstrated by the design freedom that can be achieved, such as the possibility of producing geometries or topologically optimised lightweight components not possible by other means, or even consolidating assemblies into single parts. Whilst AM is a common term used to describe a group of advanced manufacturing technologies that create objects in a layer-wise method [94], only a few of these technologies are appropriate for producing structural components. One of the dominant methods for producing functional metal parts with properties that can rival those of traditional processing techniques is via laser powder bed fusion (LPBF) [95, 96]. LPBF was be the focal technology of this research due to its high manufacturing resolution, cost-effectiveness when manufacturing parts at scale and existing regulatory approval and supply chain in industry [21, 97, 98].

During the laser powder bed fusion process, micron sized powder particles (typically 15-45 μm) are spread in very thin layers (typically 25-60 μm) on a build platform and melted by the absorption of radiation from the thermal energy of a fibre laser beam under an inert atmosphere. The process begins by creating a computer-aided design (CAD) model of the object to be built and then geometrically slicing it into thin layers. Scan vectors are then generated to trace the contours of the cross-section with 'hatch scans' filling it in. This information is then transferred to a laser powder bed fusion system. For every layer, the laser beam exposes the relevant crosssectional area of the part(s), thereby melting and re-solidifying the powder particles to each other and to the layer beneath, the build platform is then lowered, coated with a new layer of powder and the process repeats. In order to achieve this, a coating device, usually with a silicon wiper, spreads a new layer of powder onto the previous layer. The laser beam is directed and focused across the surface of the powder bed/build platform by scanner mirrors (galvanometers) and optics (typically an f – Theta lens) respectively in such a way that the powder particles can be melted where desired.

2.5.2 Applications of Additive Manufacturing

There are numerous applications for AM implants which respect bone's local mechanical environment. These include the proximal tibia in the knee, the acetabulum of the hip and inter-vertebral body fusion in the spine, owing to the prevalence of osteoarthritis in these joints and the suitability of AM solutions in these applications [99–101]. Common successful procedures include total knee arthroplasty, partial knee arthroplasty, tibial osteotomy, hip resurfacing, total hip replacement and spinal fusion. Although these procedures are all promising, the long-term function and implant stability are suboptimal as none of them take advantage of the mechanoresponse of bone and result in bone resorption, implant loosening and failure due to comparatively high stiffness [5, 102]. There may be an opportunity for these treatments to harness bone's natural mechanoresponse by invoking a localised increase in strain in the range of 50-4000 $\mu\epsilon$ to maintain or improve the quality of the bone in which they are placed [103]. Implants with apparent modulus designed to control bone mechanobiology have been demonstrated in some cases [104, 105]. These would benefit from improved prediction and refined knowledge of the spatial variation of multi-axial bone properties within the proximal tibia. This could be particularly useful for early intervention treatments that are likely to be revised in the patient's lifetime as it would preserve, or even enhance, the bone available for implantation of the revision prothesis. In order to do this, it is necessary to understand and predict mechanical properties, such as apparent modulus and strength, in a clinically viable workflow as has been discussed here.

Bone is a unique and complex dynamic material, which remodels in response to applied strain, giving it enormous potential for biomimimetic designed implants using additive manufacturing. The apparent modulus is the key parameter for implant design, which can be predicted from CT scans and varies with respect to anatomical position and loading direction. Design of AM implants has the potential to harness the natural mechanoresponse of bone to invoke strain and induce desired bone formation. Such designs must be based upon understanding of the mechanical properties of bone at the implant site, and knowledge of the physical and mechanical properties of AM scaffolds and the manufacturing parameters that influence these.

Until recently Titanium implants were only manufactured by forging or machining as large pieces of metal due to limitations in manufacturing technology. Developments in additive manufacturing have enabled authors such as Ghouse et al., Van Arkel et al. and others to manufacture lattice based components [104, 106–111].

One advantage of additive manufacturing over conventional manufacturing methods is that complexity in design does not translate to complexity in

manufacture. This means that methods such as topology optimisation can be used to integrate reinforcing members into components at little additional cost.

2.5.3 Fatigue Life of Porous Implants

Material fatigue is a key consideration and one of the principal concerns related to the safety of additively manufactured scaffolds for bone repair. Fatigue failure occur under cyclic loading of a component or structure and is caused by the initiation of cracks either at the surface of a component or from pores within. Typically, fatigue failure occurs at stress below the static yield stress, making design for fatigue a key consideration. In the body, implants may typically need to survive upwards of 30 million cycles in their lifetime (8000 steps per day for 10 years), hence it is necessary to design structures for high cycle fatigue.

The problem of fatigue in orthopaedic implants is compounded when additive manufacturing is considered. The rough surface characteristic and inherent internal porosity provide excessive sites at which crack initiation may occur. This has been explored extensively in literature, where the AM-specific issues such as rapid cooling, high temperature gradients and complex micro-structures are common [112–120]. Methods of improving fatigue life in AM structures has been explored and summarised below.

2.5.4 Improvements in surface area

In porous structures the ratio of surface area to material volume is significantly greater than for solid structures, meaning that there are likely more crack initiation sites at the surface. Improving the surface finish of a structure is therefore a viable way to improve fatigue life. This has been achieved in literature via chemical etching, grit-blasting and heat treatment.

Chemical etching can be used to improved surface roughness and has been shown to improved fatigue life [115, 116, 121, 122]. Pintado et al. showed that grit-blasting can be used to go one step further, improving surface finish as well as imparting a compressive stress at the surface [123]. By contrast, heat treatment methods have been shown to improve fatigue life by reducing internal porosites. Hot isostatic pressing (HIP) treatments can be used to achieve a significant improvement in fatigue strength (a 80% increase in fatigue endurance ratio at 10^6 cycles has been shown), despite having negligible effects on surface roughness [124, 125]. Of course, combining these various methods can achieve fatigue strength even greater than any one treatment alone [126–128].

In summary, fatigue life is a key issue for both orthopaedic implants and additive manufactured porous components. Extensive work has been done to ascertain methods of improving fatigue life, largely focused on improving surface roughness and internal structure. A key consideration is the effect of material choice on

optimal treatment to improve fatigue strength. Recommended treatments vary between materials and even alloys of the same metal [112]. Design for fatigue is not pursued further in this thesis, however, choices of structural parameters, material and printing parameters will be made aiming to increase the ratio of fatigue strength to apparent modulus based on literature.

2.6 Clinical Applications of Porous Materials

Porous structures such as lattices and sheet-based cell structures are of growing use in orthopaedics as a route to improve implant fixation through osseointegration and improving bone maintenance by reducing stress shielding.

2.6.1 Osseointegration

Joint replacement surgery requires that metal components are bonded to bone. This is conventionally done with screws and cement. This approach has been shown to be cost-effective and gives long-term success. Some limitations such as longer surgery times, cement fragmentation, and the potential for the body to react negatively to wear debris [129–132]. These techniques also have the potential to cause stress-shielding, leading to the deterioration of the bone, as well as implant loosening and the need for revision surgery over time [133, 134]. These complications have inspired both academia and industry to pursue alternative measures of fixation.

Cementless arthroplasty relies on the natural growth of bone tissue onto and into the surface of the implant for fixation and is a logical area of development to address limitations of cemented joint replacement. This process, called osseointegration, begins several weeks after the implant is placed. This process is an extension of bone's natural formation response, whereby many structures and material factors of the implant surface encourage bone formation. An implant is typically impacted with an interference fit into good quality bone stock to ensure initial fixation - this can lead to higher fracture risk compared to cemented implants [135–138]. While initial fixation is provided by interference fit, the absence of cement gives the opportunity for longer-term fixation to be moderated by bone ongrowth and ingrowth, otherwise known as osseointegration [139]. Crucially, the strength of bond achieved with this fit is dependent on the quality of bone (largely a reflection of its apparent modulus) and the level of interference fit - whereby a larger interference fit achieves a better bond but also induces higher stresses and fracture risk in the bone.

Osseointegration requires an environment suitable for differentiated osteoblasts to adhere to, profilerate through and vasularise within [140, 141]. This process gradually builds up bone mineral and is influenced by a number of structural and material properties such as surface pore size and surface roughness. Methods

such as plasma spraying and grit blasting can achieve a surface suitable for ongrowth [142]. In contrast titanium beading, fiber meshes, hydroxyapetite coatings and additive manufacturing can be used to form open surface structures for virgin bone to proliferate into [143, 144]. Porous structures can be effective in promoting osseointegration, the natural growth of bone tissue onto and into the surface of an implant, because they provide a matrix onto which cells can attach, differentiate, grow, and interact, leading to bone regeneration [145]. The structural parameters of porous architectures can be controlled to moderate and encourage bone growth.

The main limitation of cementless arthroplasty is the high impaction forces required to achieve a strong seating of an implant, which will affect osseointegration. Osseointegration can take up to 12 weeks and is faster in younger, more active patients [146, 147]. This is why such implants are typically more suitable for younger patients who have healthy bones. Literature shows that minimising micromotion between an implant and bone improves osseointegration, although no optimal micromotion threshold has been shown (micromotion can typically range from tens to hundreds of a micrometer depending on implant design) [148, 149]. Knowledge of optimal structures and materials for osseointegration is required in the development of a new implant. Although the ideal pore structures for ingrowth are not documented here, where necessary the range of pore sizes and strut roughness will be selected based on suitable parameters given in literature. Finally, material selection in any relevant testing will be limited to materials already in used in industry to ensure not just biocompatibility but also scalability through regulation and manufacture (Titanium and Titanium alloys, Cobalt-Chromium Molybdenum alloys and PEEK) [150].

2.6.2 Stress shielding

Bone's dynamic remodelling behaviour means that a a balance is constantly maintained between bone formation and bone resorption [27]. This balance is maintained by strain in bone as it is loaded (as well as other contribution factors). A reduction in mechanical stimulus can therefore result in loss of bone quality. This phenomenon is manifested when areas of peri-prosthetic bone experience reduced strains (and stresses) post-surgery due to bone with modulus typically in the range from 200 MPa to 1500 MPa because ranged by orthopaedic implants manufactured from solid metal, often cobalt–chromium–molybdenum or titanium with a modulus of 230 GPa and 113 GPa respectively. The disruption in mechanical environment and reduction in strain magnitudes caused by such implants can result in stress shielding.

Prolonged stress shielding leads to a decrease in bone density and inevitably weakened bone [5]. In turn this leads to surgical complications for the patient and surgeon such as post-surgical complications and failure due to aseptic loosening.

Currently 35% of revisions in partial knee cases are due to aseptic loosening and in such cases it is expected that loss of biologic fixation and a reduction in bone density may contribute to this need for revision [4, 130, 151]. Porous structures may be useful in orthopaedic not just because of their potential for ongrowth and ingrowth to improve fixation but also because they allow for the mechanical modulus of the implant to be tailored to that of bone [1, 152]. In this way, implants may be able to maintain bone strains similar to those which are typically experienced in healthy bone so that healthy and positive remodelling can continue to occur post-surgery. In research studies, this has been demonstrated by modulating the mechanical modulus of structures to vary bone remodelling, which can be inferred from bone density measurements [153].

Ashby and Gibson showed that bulk material modulus and structure both contribute to the apparent modulus of a porous material [154]. Structural contributions can be split into volume fraction effects (whereby a structure with greater relative density has a greater modulus), connectivity effects (whereby how many neighbouring nodes a node connects with can influence its deformation) and directional effects (whereby fabric effects and strut or pore directionality affect anisotropy) [79, 88]. Typical approaches seek to select of parent material which can achieve a range of modulus values sufficient for the design use, i.e. Nylon structure inherently have a modulus lower than Titanium structures [153, 155]. For the purpose of the work in the remainder of this thesis, modulus of porous structures will be controlled by variation of both structural topology (structure fabric and CAD geometry) and strut thickness (relative density).

2.7 Rationale and review of experimental approaches used

In the following Chapters, 3 through 6, a combination of experimental methods have been used. Below is a summary and rationale of the methods used and in particular why they were chosen to address the aim of each specific Chapter.

2.7.1 Chapter 3: Prediction and characterisation of bone's properties

In this chapter, testing is conducted to assess the mechanical properties of bone. Cadaveric bone was extracted in cubes and compression tested in an Instron testing machine.

Bone cubes were used instead of cylinders as this enabled multi-axial testing of each core. It could have been possible to extract cylinders in varying directions to analyse multi-axial properties, however, this would have meant that fewer cores were extracted from each specimen. Literature also suggests suitable core

dimensions and aspect ratios for cubic and cylindrical cores and cylindrical cores would have been significantly larger than cubic cores, again meaning that fewer cores would have been extracted from each donor specimen. A larger sample size was beneficial for this study and enabled full characterisation of proximal tibial bone.

When performing the multi-axial compression testing, each bone cube was sequentially tested in each direction (anterior-posterior, inferior-superior and medial-lateral). This approach was preferred to one where each cube was only tested in one direction and compressed to failure. Testing each cube to failure in one direction would have mitigated any concerns of a test in a given direction affecting subsequent tests in the remaining orthogonal directions, but this would have also reduced the sample size by two thirds. On balance the approach taken was to randomise the order of testing direction for each sample and demonstrate with preliminary testing that testing in a direction did not affect the material properties measured in any subsequent direction.

Another method considered was indentation testing, as oppose to compression testing with 9mm side length cubes. This would have enabled measurement of the apparent modulus to be measured at a greater spatial resolution across the bone, compared to the 9mm resolution achieved with bone cubes. One negative consequence of this method would have been that indentation testing typically determines stiffness, rather than modulus. Modulus, as a material product, was the preferred variable to be examined in this study because it could be easily translated to other uses, such as in computational modelling and to influence implant design. On balance the priority to measure multi-axial apparent modulus meant that extracting bone cubes was the best way to consistently and repeatably measure material properties in this case.

A key consideration when working with cadaveric samples is the freeze-thaw protocol. In this study the samples were thawed, cut and tested all in the same day to reduce freeze-thaw effects.

When compression testing bone cubes, sample preparation can have significant effects on results [32]. Some authors have used grinding of samples to improve parallelity of sample face, which is required for the valid testing of mechanical properties such as apparent modulus. A consequence of grinding sample faces to maintain parallel faces is that metal particles typically become embedded in the sample which can affect properties during testing. The custom jigs used in Chapter 3 helped to achieve suitably parallel and orthogonal faces.

During the compression testing protocol strain was calculated from extension measurements made with linear variable differential transformers (LVDTs). A high resolution extension measurement is required for the calculation of modulus and to mitigate machine compliance effects. Other methods were available, such as

extensometers which would have been ill-suited to the small sample size and sample yielding or digital image correlation (DIC) which would have produced unnecessarily large amounts of data and has a setup time cost.

When analysing the results, a multivariate anova was used because this allowed the inclusion of all possible confounding input variables and covariates with all output variables.

2.7.2 Chapter 4: Characterisation and control of lattice modulus and anisotropy

In this Chapter, lattice based porous structures were manufactured in a number of orientations and compression tested to characterise their modulus and strength. This data was then used to train a model for predicting anisotropic apparent modulus and strength of titanium stochastic lattices and nylon repeating cell structures.

For the manufacture of lattice based parts there are a number of additive manufacturing techniques which may be suitable. Laser powder bed fusion (LPBF) was sued in this study because of the background and previous experience within the team and because of the high level of structural control which LPBF can achieve. With LPBF the strut diameter, apparent modulus, connectivity, strut density, surface roughness and geometry can all be controlled.

Similarly to in Chapter 3, the high resolution strain maps which can be achieved with DIC were not required for this analysis. Characterisation of the structures' apparent modulus and strength could be achieved with compression testing with LVDTs to capture extension for strain and modulus calculations.

In this study a matrix form of Cowin's equations for stress tensors were used to calculate coefficients which then enabled prediction of off-axis mechanical properties. This method utilised mechanical property data from compression testing as well as structure fabric data from CAD geometry. Other authors have found fabric data from the mean intercept length (MIL) method, which requires segmented structures from micro-CT data. The MIL method may have been a better measure, because it used determines fabric directly from the manufactured parts, whereas a CAD based method assumes a perfectly manufactured structure. The advantage of using a CAD based method is that off-axis mechanical properties can be predicted for structures quickly during the design process.

2.7.3 Chapter 5: Application of lattices for fine control of bone strains

In Chapter 5 a combination of Tekscan and LVDTs were used to measure the stress an strain change when bone is loaded alongside a lattice of controlled modulus. The lattices were manufactured to have a modulus dictated by and

scaled to the modulus of the bone. This study utilised the same bone cubes as discussed in Chapter 3 and some of the method considerations regarding cadaveric bone cubes were also relevant here.

Neither metal nor bone cube samples had their surfaces ground for this study. In the case of bone cubes this was to ensure that no metal particles became embedded in the bone. For the metal samples they were accurately cut from a build plate using electrical discharge machining which gave a suitably flat cut. DIC was considered as a method to measure the strain in both bone cubes and lattices, however, the glossy surface finish of the bone proved unsuitable for this. It may be possible to coat the bone in a speckle pattern, but this was not necessary for this study. Furthermore, the work in Chapter 5 did not require knowledge of the localised strains so using LVDTs was suitable.

2.7.4 Chapter 6: Demonstration of the technology in partial and total knee implants

In this study the results and outcomes from Chapters 3, 4 and 5 are combined to manufacture a series of lattice implants with apparent modulus matched to the peri-prosthetic bone with varying degrees of closeness. These implants are then loaded in cadaveric knees and the distribution of stresses around the implant are measured with Tekscan pressure film and compared to the native knee.

An alternative method for this study could have been to use a finite element approach rather than human cadaveric specimens. This would have had the advantage of producing greater resolution data, with knowledge of the dispersion of stress and strain at various depths beneath an implant. With finite element modelling it would have also been possible to observe various characteristics of the bone, such as strain, displacement and stress in multiple directions. Furthermore, a finite element approach could have enable a more accurate representation of typical orthopaedic implants as no modification to implant designs would have been necessary. The cadaveric method chosen required the implants to be designed without a keel so that the testing setup could accommodate a Tekscan pressure sensor beneath the implant. Another reason to follow a cadaveric method was that conducting the testing in the way described in Chapter 6 aided future translation of this technology, serving as a demonstration that the technology developed would perform as intended in an environment close to clinical practice. Part of he challenge of this study was demonstrating that the processes and platform developed in Chapters 3 to 5 as well as previous literature could actually be applied in a real implant, manufactured with industry standard methods.

Tekscan pressure film is a useful tool to measure stress magnitudes and distributions across a surface. Fuji film is an alternative suitable for some similar

scenarios. Both sensors are similar and can achieve similar results providing a thorough calibration (and equilibration for Tekscan) is performed. Fuji film only records a maximum pressure on a particular sensel and uses a colour staining technique rather than an electronic sensor. This means that once a Fuji film sensel has seen a given load, it will not change if the load is reduced. Assembling the full test setup was a difficult and cumbersome process, inserting the pressure film and implants through a small para-patella incision. This meant that a pressure film which might be damaged or accidentally loaded during test setup, such as Fuji film, was not suitable.

The order of testing each implant was randomised for each cadaveric specimen. This mitigated any concerns over whether testing a specific implant would affect subsequent tests. In a similar way, this study tested medial UKA followed by revision to TKA. In each case the native knee was tested first before implanting each implant. This does mean that the testing protocol was optimised for UKA results rather than TKA, because the TKA results may have been affected by the previous UKA studies. Had this been conducted with finite element methods then this would not be a consideration. Defining the test protocol in this way did mean that each specimen acted as its own control, because every UKA and TKA test was directly comparable to the intact native case for that knee.

A third alternative for this study was to use synthetic bone, such as polyurethane foams or Sawbone. In spite of being a less costly and simpler method with no time or freeze-thaw restrictions, key limitation of such a method is that there would be no variation in bone apparent modulus across the cut plane. This would make it difficult to conclude which implant designs performed better and for what reason.

2.8 Summary

- Bone is mechanobiological in nature and its remodelling can be accelerated by controlling the strain it experiences. High resolution mappings of the mechanical environment in the proximal knee have not been characterised and thus inconsistencies exist regarding optimal structural characteristics of porous scaffolds.

- The anisotropic nature of porous structures has not been fully explored. It is necessary to understand the off-axis modulus and strength of porous structures and be able to use such properties to predict how structures will respond to complicated multi-axial loading. This can integrate material and structural properties.

- Additive manufactured structures can be used to control bone strains under given loading but the interplay between implant multiaxial modulus and bone strain response has not yet been explored.

- Optimising implant modulus with porous structures and applying this in the unicompartmental and total knee arthroplasty implants has not been done before in a way which seeks to replicate the bone's mechanical environment. This would enable implants to comntinue to stimulate bone growth into the implant and around the implant.

2.9 Bibliography

[1] S. Wu, X. Liu, K. W. Yeung, C. Liu, and X. Yang, "Biomimetic porous scaffolds for bone tissue engineering," *Materials Science and Engineering: R: Reports*, vol. 80, pp. 1–36, 6 2014.

[2] J. Wieding, T. Lindner, P. Bergschmidt, and R. Bader, "Biomechanical stability of novel mechanically adapted open-porous titanium scaffolds in metatarsal bone defects of sheep," *Biomaterials*, vol. 46, pp. 35–47, 4 2015.

[3] GlobalData, "Global hip and knee replacement market report," tech. rep., 2018.

[4] G. S. Dyrhovden, S. H. L. Lygre, M. Badawy, Gøthesen, and O. Furnes, "Have the Causes of Revision for Total and Unicompartmental Knee Arthroplasties Changed During the Past Two Decades?," *Clinical Orthopaedics and Related Research*, vol. 475, p. 1874, 7 2017.

[5] J. T. Deen, T. B. Clay, D. A. Iams, M. B. Horodyski, and H. K. Parvataneni, "Proximal tibial resorption in a modern total knee prosthesis," *Arthroplasty Today*, vol. 4, pp. 244–248, 6 2018.

[6] Versus Arthtitis, "About arthritis | Conditions, symptoms, treatments, support," 2022.

[7] P. Howard, R. Brittain, S. Lawrence, J. Stonadge, M. Wilkinson, T. Wilton, S. Dawson-Bowling, A. Watts, O. Specialists, R. Craig, C. Esler, A. Goldberg, S. Jameson, T. Jennison, J. Rees, A. Toms, E. Young, C. Boulton, D. Taylor, O. Espinoza, V. Mccormack, C. Newell, M. Royall, M. Swanson, Y. Ben-Shlomo, A. Blom, E. Clark, K. Deere, C. Gregson, L. Hunt, A. Judge, E. Lenguerrand, A. Price, D. Prieto-Alhambra, A. Sayers, and M. Whitehouse, "National Joint Registry | 17th Annual Report," tech. rep., National Joint registry, 2020.

[8] A. Liddle, H. G. Pandit, A. Judge, and D. W. Murray, "Patient-reported outcomes after total and unicompartmental knee arthroplasty," *https://doi.org/10.1302/0301-620X.97B6.35155*, vol. 97-B, pp. 793–801, 6 2015.

[9] P. F. Sharkey, P. M. Lichstein, C. Shen, A. T. Tokarski, and J. Parvizi, “Why are total knee arthroplasties failing today-has anything changed after 10 years?,” *Journal of Arthroplasty*, vol. 29, pp. 1774–1778, 4 2013.

[10] D. F. Dalury, D. L. Pomeroy, R. S. Gorab, and M. J. Adams, “Why are total knee arthroplasties being revised?,” *Journal of Arthroplasty*, vol. 28, pp. 120–121, 9 2013.

[11] M. Bhandari, J. Smith, L. E. Miller, and J. E. Block, “Clinical and Economic Burden of Revision Knee Arthroplasty,” *Clinical Medicine Insights: Arthritis and Musculoskeletal Disorders*, vol. 5, p. CMAMD.S10859, 1 2012.

[12] S. Shankar, M. W. Tetreault, B. J. Jegier, G. B. Andersson, and C. J. Della Valle, “A cost comparison of unicompartmental and total knee arthroplasty,” *Knee*, vol. 23, no. 6, pp. 1016–1019, 2016.

[13] C. Willis-owen, K. Brust, H. Aslop, M. Miraldo, and J. P. Cobb, “Unicondylar knee arthroplasty in the UK National Health Service: An analysis of candidacy, outcome and cost efficacy,” *The Knee*, vol. 16, no. 6, pp. 473–478, 2009.

[14] H. M. Kremers, S. L. Visscher, J. P. Moriarty, M. S. Reinalda, W. K. Kremers, J. M. Naessens, and D. G. Lewallen, “Determinants of Direct Medical Costs in Primary and Revision Total Knee Arthroplasty,” *Clinical Orthopaedics and Related Research*, vol. 471, pp. 206–214, 2013.

[15] M. D. Ries, N. Lenz, G. Jerry, A. Salehi, and S. Haddock, “Is modern bicruciate retaining TKA feasible?,” *Seminars in Arthroplasty*, vol. 29, no. 1, pp. 55–57, 2018.

[16] J. C. Stoddart, O. Dandridge, A. Garner, J. Cobb, and R. J. van Arkel, “The compartmental distribution of knee osteoarthritis – a systematic review and meta-analysis,” *Osteoarthritis and Cartilage*, vol. 29, pp. 445–455, 4 2021.

[17] T. Dehn, A. Price, and R. Allum, “Management of Osteoarthritis of the Knee: The case for partial knee replacement,” *Controversial Topics in Surgery*, vol. 92, pp. 459–462, 2010.

[18] A. Garner, R. J. van Arkel, and J. Cobb, “Classification of combined partial knee arthroplasty,” *The Bone & Joint Journal*, vol. 101-B, pp. 922–928, 8 2019.

[19] M. E. Roy, L. A. Whiteside, K. K. Ly, and M. J. Gauvain, “Cobalt-chromium femoral components developed scratches and released metal debris in simulated wear whereas ceramic femoral components did not,” *The bone & joint journal*, vol. 103-B, pp. 94–101, 6 2021.

[20] A. Razak, A. D. Ebinesan, and C. P. Charalambous, “Metal Hypersensitivity in Patients with Conventional Orthopaedic Implants,” *JBJS Reviews*, vol. 2, 2 2014.

[21] X. Wang, S. Xu, S. Zhou, W. Xu, M. Leary, P. Choong, M. Qian, M. Brandt, and Y. M. Xie, “Topological design and additive manufacturing of porous metals for bone scaffolds and orthopaedic implants: A review,” *Biomaterials*, vol. 83, pp. 127–141, 3 2016.

[22] S. A. Goldstein, D. L. Wilson, D. A. Sonstegard, and L. S. Matthews, “The mechanical properties of human tibial trabecular bone as a function of metaphyseal location,” *Journal of Biomechanics*, vol. 16, pp. 965–969, 1 1983.

[23] J. Wolff, “Concept of the Law of Bone Remodelling,” in *The Law of Bone Remodelling*, Berlin, Heidelberg: Springer Berlin Heidelberg, 1986.

[24] C. Ruff, B. Holt, and E. Trinkaus, “Who’s afraid of the big bad Wolff?: “Wolff’s law” and bone functional adaptation,” *American Journal of Physical Anthropology*, vol. 129, pp. 484–498, 4 2006.

[25] L. F. Bonewald, “The amazing osteocyte,” *Journal of Bone and Mineral Research*, vol. 26, pp. 229–238, 2 2011.

[26] S. M. Perren and A. Boitzy, “La différenciation cellulaire et la biomécanique de l’os au cours de la consolidation d’une fracture,” *Anatomia Clinica*, vol. 1, pp. 13–28, 3 1978.

[27] H. M. Frost, “Bone, mass and the Mechanostat: A proposal,” *The Anatomical Record*, vol. 219, pp. 1–9, 9 1987.

[28] N. Reznikov, C. Phillips, M. Cooke, A. Garbout, F. Ahmed, and M. M. Stevens, “Functional Adaptation of the Calcaneus in Historical Foot Binding,” *Journal of Bone and Mineral Research*, vol. 32, pp. 1915–1925, 2017.

[29] J. M. García-Aznar, M. J. Gómez-Benito, M. Pérez, and M. Doblaré, “Mechanobiological Models for Bone Tissue. Applications to Implant Design,” in *Biomechanics of Hard Tissues*, pp. 123–143, Weinheim, Germany: Wiley-VCH Verlag GmbH & Co. KGaA, 11 2010.

[30] S. J. Carrington, C. C. Hernandez, D. R. Swale, O. A. Aluko, J. S. Denton, and R. D. Cone, “G protein–coupled receptors differentially regulate glycosylation and activity of the inwardly rectifying potassium channel Kir7.1,” *Journal of Biological Chemistry*, vol. 293, pp. 17739–17753, 11 2018.

[31] D. J. Hadjidakis and I. I. Androulakis, "Bone remodeling," *Annals of the New York Academy of Sciences*, vol. 1092, pp. 385–396, 2006.

[32] S. Zhao, M. Arnold, S. Ma, R. L. Abel, J. P. Cobb, U. Hansen, and O. Boughton, "Standardizing compression testing for measuring the stiffness of human bone," *Bone & Joint Research*, vol. 7, no. 8, pp. 524–538, 2018.

[33] E. F. Eriksen, F. Melsen, E. Sod, I. Barton, and A. Chines, "Effects of long-term risedronate on bone quality and bone turnover in women with postmenopausal osteoporosis," *Bone*, vol. 31, pp. 620–625, 11 2002.

[34] S. C. S. C. Cowin, *Bone mechanics handbook*. CRC Press, 2001.

[35] M. S. Rahman, N. Akhtar, H. M. Jamil, R. S. Banik, and S. M. Asaduzzaman, "TGF-β/BMP signaling and other molecular events: regulation of osteoblastogenesis and bone formation," *Bone Research 2015 3:1*, vol. 3, pp. 1–20, 4 2015.

[36] J. C. Fritton, C. T. Rubin, Y. X. Qin, and K. J. McLeod, "Whole-Body Vibration in the Skeleton : Development of a Resonance-Based Testing Device Feedback RMS-to-DC Amplifier Converter," *Annals of Biomedical Engineering*, vol. 25, pp. 831–839, 1997.

[37] E. H. Burger and J. Klein-Nulend, "Mechanotransduction in bone—role of the lacunocanalicular network," *The FASEB Journal*, vol. 13, pp. S101–S112, 5 1999.

[38] D. B. Burr, "Remodeling and the repair of fatigue damage," *Calcified tissue international*, vol. 53 Suppl 1, 2 1993.

[39] O. Verborgt, G. J. Gibson, and M. B. Schaffler, "Loss of Osteocyte Integrity in Association with Microdamage and Bone Remodeling After Fatigue In Vivo," *Journal of Bone and Mineral Research*, vol. 15, pp. 60–67, 1 2000.

[40] A. G. Robling and C. H. Turner, "Mechanical signaling for bone modeling and remodeling," *Critical Reviews in Eukaryotic Gene Expression*, vol. 19, no. 4, pp. 319–338, 2009.

[41] B. S. Noble, N. Peet, H. Y. Stevens, A. Brabbs, J. R. Mosley, G. C. Reilly, J. Reeve, T. M. Skerry, and L. E. Lanyon, "Mechanical loading: Biphasic osteocyte survival and targeting of osteoclasts for bone destruction in rat cortical bone," *American Journal of Physiology - Cell Physiology*, vol. 284, 4 2003.

[42] L. I. Plotkin, S. C. Manolagas, and T. Bellido, "Glucocorticoids Induce Osteocyte Apoptosis by Blocking Focal Adhesion Kinase-mediated

Survival: Evidence for inside-out signalling leading to a anoikis," *Journal of Biological Chemistry*, vol. 282, pp. 24120–24130, 8 2007.

[43] M. Tuncer, *Fixation of Unicondylar Knee Prostheses*. PhD thesis, 2012.

[44] N. Akkas, Y. N. Yeni, B. Turan, E. Delilbasi, and U. Gunel, "Effect of medication on biomechanical properties of rabbit bones: Heparin induced osteoporosis," *Clinical Rheumatology*, vol. 16, no. 6, pp. 585–595, 1997.

[45] V. D. Sherk and C. J. Rosen, "Senescent and apoptotic osteocytes and aging: Exercise to the rescue?," *Bone*, vol. 121, pp. 255–258, 4 2019.

[46] M. J. Mirzaali, J. J. Schwiedrzik, S. Thaiwichai, J. P. Best, J. Michler, P. K. Zysset, and U. Wolfram, "Mechanical properties of cortical bone and their relationships with age, gender, composition and microindentation properties in the elderly," *Bone*, vol. 93, pp. 196–211, 12 2016.

[47] P. J. Kelly, L. Twomey, P. N. Sambrook, and D. J. A. Eisman, "Sex differences in peak adult bone mineral density," *American Society for Bone and Mineral Research*, vol. 5, no. 11, pp. 1169–1175, 1990.

[48] H. Burger, P. L. van Daele, D. Algra, F. A. van den Ouweland, D. E. Grobbee, A. Hofman, C. van Kuijk, H. E. Schütte, J. C. Birkenhäger, and H. A. Pols, "The association between age and bone mineral density in men and women aged 55 years and over: The Rotterdam Study," *Bone and Mineral*, vol. 25, no. 1, pp. 1–13, 1994.

[49] F. Mauvais-Jarvis, N. Bairey Merz, P. J. Barnes, R. D. Brinton, J. J. Carrero, D. L. DeMeo, G. J. De Vries, C. N. Epperson, R. Govindan, S. L. Klein, A. Lonardo, P. M. Maki, L. D. McCullough, V. Regitz-Zagrosek, J. G. Regensteiner, J. B. Rubin, K. Sandberg, and A. Suzuki, "Sex and gender: modifiers of health, disease, and medicine," 8 2020.

[50] I. Hvid and S. L. Hansen, "Trabecular bone strength patterns at the proximal tibial epiphysis," *Journal of Orthopaedic Research*, vol. 3, pp. 464–472, 1 1985.

[51] F. J. Klever, R. Klumpert, J. Horenberg, H. J. Grootenboer, D. H. Van Campen, and T. Pauly, "Global Mechanical Properties of Trabecular Bone: Experimental Determination and Prediction from a Structural Model," in *Biomechanics: Current Interdisciplinary Research*, pp. 167–172, Springer Netherlands, 1985.

[52] R. B. Ashman, J. Y. Rho, and C. H. Turner, "Anatomical variation of orthotropic elastic moduli of the proximal human tibia," *Journal of Biomechanics*, vol. 22, no. 8-9, pp. 895–900, 1989.

[53] A. Odgaard, I. Hvid, and F. Linde, “Compressive axial strain distributions in cancellous bone specimens,” *Journal of Biomechanics*, vol. 22, pp. 829–835, 1 1989.

[54] T. M. Keaveny, R. E. Borchers, L. J. Gibson, and W. C. Hayes, “Trabecular bone modulus and strength can depend on specimen geometry,” *Journal of Biomechanics*, vol. 26, pp. 991–1000, 8 1993.

[55] O. Lindahl, “To cite this article: Olov Lindahl (1976) Mechanical Properties of Dried Defatted Spongy Bone,” *Acta Orthopaedica Scandinavica*, vol. 47, no. 1, pp. 11–19, 2009.

[56] A. Garg and P. S. Walker, “The effect of the interface on the bone stresses beneath tibial components,” *Journal of Biomechanics*, vol. 19, pp. 957–967, 1 1986.

[57] I. Hvid and J. Jensen, “Cancellous bone strength at the proximal human tibia,” *The Orthopaedic Hospital, Arhus, Denmark*, vol. 13, no. 1, pp. 21–25, 1984.

[58] A. Odgaard and F. Linde, “The underestimation of Young’s modulus in compressive testing of cancellous bone specimens,” *Journal of Biomechanics*, vol. 24, pp. 691–698, 1 1991.

[59] S. M. Bentzen, I. Hvid, and J. Jorgensen, “Mechanical strength of tibial trabecular bone evaluated by X-ray computed tomography,” *Journal of Biomechanics*, vol. 20, pp. 743–752, 1 1987.

[60] D. R. Carter and W. C. Hayes, “The compressive behavior of bone as a two-phase porous structure,” *Bone & Joint Research America*, vol. 59, pp. 954–962, 1 1977.

[61] M. J. Ciarelli, S. A. Goldstein, J. L. Kuhn, D. D. Cody, and M. B. Brown, “Evaluation of orthogonal mechanical properties and density of human trabecular bone from the major metaphyseal regions with materials testing and computed tomography,” *Journal of Orthopaedic Research*, vol. 9, no. 5, pp. 674–682, 1991.

[62] F. Linde and I. Hvid, “The effect of constraint on the mechanical behaviour of trabecular bone specimens,” *Journal of Biomechanics*, vol. 22, pp. 485–490, 1 1989.

[63] J. D. Johnston, S. A. Kontulainen, B. A. Masri, and D. R. Wilson, “Predicting subchondral bone stiffness using a depth-specific CT topographic mapping technique in normal and osteoarthritic proximal tibiae,” *Clinical Biomechanics*, vol. 26, pp. 1012–1018, 12 2011.

[64] F. Linde, P. Nørgaard, I. Hvid, A. Odgaard, and K. Søballe, “Mechanical properties of trabecular bone. Dependency on strain rate,” *Journal of Biomechanics*, vol. 24, pp. 803–809, 1 1991.

[65] F. Linde, I. Hvid, and F. Madsen, “The effect of specimen geometry on the mechanical behaviour of trabecular bone specimens,” *Journal of Biomechanics*, vol. 25, pp. 359–368, 4 1992.

[66] F. Linde, B. Pongsoipetch, L. H. Frich, and I. Hvid, “Three-axial strain controlled testing applied to bone specimens from the proximal tibial epiphysis,” *Journal of Biomechanics*, vol. 23, pp. 1167–1172, 1 1990.

[67] E. F. Morgan, H. H. Bayraktar, and T. M. Keaveny, “Trabecular bone modulus–density relationships depend on anatomic site,” *Journal of Biomechanics*, vol. 36, pp. 897–904, 7 2003.

[68] S. M. Nazemi, M. Amini, S. A. Kontulainen, J. S. Milner, D. W. Holdsworth, B. A. Masri, D. R. Wilson, and J. D. Johnston, “Optimizing finite element predictions of local subchondral bone structural stiffness using neural network-derived density-modulus relationships for proximal tibial subchondral cortical and trabecular bone,” *Clinical Biomechanics*, vol. 41, pp. 1–8, 1 2017.

[69] J. Rice, S. Cowin, and J. Bowman, “On the dependence of the elasticity and strength of cancellous bone on apparent density,” *Journal of Biomechanics*, vol. 21, pp. 155–168, 1 1988.

[70] L. Rincón-Kohli, P. K. Zysset, L. Rincón-Kohli, and P. K. Zysset, “Multi-axial mechanical properties of human trabecular bone,” *Biomech Model Mechanobiol*, vol. 8, pp. 195–208, 2009.

[71] Z. Tabor and E. Rokita, “Quantifying anisotropy of trabecular bone from gray-level images,” *Bone*, vol. 40, pp. 966–972, 4 2007.

[72] J. L. Williams and J. L. Lewis, “Properties and an anisotropic model of cancellous bone from the proximal tibial epiphysis,” *Journal of Biomechanical Engineering*, vol. 104, pp. 50–56, 2 1982.

[73] M. Tuncer, U. N. Hansen, and A. A. Amis, “Prediction of structural failure of tibial bone models under physiological loads: Effect of CT density–modulus relationships,” *Medical Engineering & Physics*, vol. 36, pp. 991–997, 8 2014.

[74] H. A. Gray, F. Taddei, A. B. Zavatsky, L. Cristofolini, and H. S. Gill, “Experimental validation of a finite element model of a human cadaveric tibia,” *Journal of Biomechanical Engineering*, vol. 130, p. 031016, 6 2008.

[75] A. Odgaard, J. Kabel, B. Van Rietbergen, M. Dalstra, and R. Huiskes, “Fabric and elastic principal directions of cancellous bone are closely related,” *Journal of Biomechanics*, 1997.

[76] W. J. Whitehouse, “The quantitative morphology of anisotropic trabecular bone,” *Journal of Microscopy*, vol. 101, pp. 153–168, 7 1974.

[77] T. P. Harrigan, M. Jasty, R. W. Mann, and W. H. Harris, “Limitations of the continuum assumption in cancellous bone,” *Journal of Biomechanics*, vol. 21, no. 4, pp. 269–275, 1988.

[78] G. Maquer, S. N. Musy, J. Wandel, T. Gross, and P. K. Zysset, “Bone volume fraction and fabric anisotropy are better determinants of trabecular bone stiffness than other morphological variables,” *Journal of Bone and Mineral Research*, vol. 30, no. 6, pp. 1000–1008, 2015.

[79] P. K. Zysset, “A review of morphology-elasticity relationships in human trabecular bone: theories and experiments,” *Journal of Biomechanics*, vol. 36, pp. 1469–1485, 2003.

[80] S. Chaffaı, F. Peyrin, S. Nuzzo, R. Porcher, G. Berger, and P. Laugier, “Ultrasonic characterization of human cancellous bone using transmission and backscatter measurements: relationships to density and microstructure,” *Bone*, vol. 30, pp. 229–237, 1 2002.

[81] C. M. Gdyczynski, A. Manbachi, S. M. Hashemi, B. Lashkari, and R. S. Cobbold, “On estimating the directionality distribution in pedicle trabecular bone from micro-CT images,” *Physiological Measurement*, vol. 35, no. 12, pp. 2415–2428, 2014.

[82] M. E. Kersh, P. K. Zysset, D. H. Pahr, U. Wolfram, D. Larsson, and M. G. Pandy, “Measurement of structural anisotropy in femoral trabecular bone using clinical-resolution CT images,” *Journal of Biomechanics*, vol. 46, no. 15, pp. 2659–2666, 2013.

[83] D. Larsson, B. Luisier, M. E. Kersh, E. Dall’Ara, P. K. Zysset, M. G. Pandy, and D. H. Pahr, “Assessment of Transverse Isotropy in Clinical-Level CT Images of Trabecular Bone Using the Gradient Structure Tensor,” *Annals of Biomedical Engineering*, vol. 42, no. 5, pp. 950–959, 2014.

[84] S. M. Nazemi, M. Amini, S. A. Kontulainen, J. S. Milner, D. W. Holdsworth, B. A. Masri, D. R. Wilson, and J. D. Johnston, “Prediction of local proximal tibial subchondral bone structural stiffness using subject-specific finite element modeling: Effect of selected density–modulus relationship,” *Clinical Biomechanics*, vol. 30, pp. 703–712, 8 2015.

[85] R. Moreno, Smedby, and D. H. Pahr, "Prediction of apparent trabecular bone stiffness through fourth-order fabric tensors," *Biomechanics and Modeling in Mechanobiology*, vol. 15, pp. 831–844, 2016.

[86] J. Hazrati Marangalou, K. Ito, and B. van Rietbergen, "A new approach to determine the accuracy of morphology–elasticity relationships in continuum FE analyses of human proximal femur," *Journal of Biomechanics*, vol. 45, pp. 2884–2892, 11 2012.

[87] P. K. Zysset, M. Sonny, and W. C. Hayes, "Morphology-mechanical property relations in trabecular bone of the osteoarthritic proximal tibia," *The Journal of Arthroplasty*, vol. 9, no. 2, pp. 203–216, 1994.

[88] S. C. Cowin, "The relationship between the elasticity tensor and the fabric tensor," *Mechanics of Materials*, vol. 4, pp. 137–147, 7 1985.

[89] R. Delaine-Smith, S. Burney, F. Balkwill, and M. Knight, "Experimental validation of a flat punch indentation methodology calibrated against unconfined compression tests for determination of soft tissue biomechanics," *Journal of the Mechanical Behavior of Biomedical Materials*, vol. 60, pp. 401–415, 7 2016.

[90] S. M. Nazemi, D. M. Cooper, and J. D. Johnston, "Quantifying trabecular bone material anisotropy and orientation using low resolution clinical CT images: A feasibility study," *Medical Engineering and Physics*, vol. 38, no. 9, pp. 978–987, 2016.

[91] R. Goulet, S. Goldstein, M. Ciarelli, J. Kuhn, M. Brown, and L. Feldkamp, "The relationship between the structural and orthogonal compressive properties of trabecular bone," *Journal of Biomechanics*, vol. 27, pp. 375–389, 4 1994.

[92] S. K. Everton, M. Hirsch, P. I. Stavroulakis, R. K. Leach, and A. T. Clare, "Review of in-situ process monitoring and in-situ metrology for metal additive manufacturing," *Materials & Design*, vol. 95, pp. 431–445, 4 2016.

[93] S. M. Yusuf and N. Gao, "Influence of energy density on metallurgy and properties in metal additive manufacturing," *Materials Science and Technology*, vol. 33, pp. 1269–1289, 7 2017.

[94] A. Yadollahi and N. Shamsaei, "Additive manufacturing of fatigue resistant materials: Challenges and opportunities," *International Journal of Fatigue*, vol. 98, pp. 14–31, 5 2017.

[95] M. J. Matthews, G. Guss, S. A. Khairallah, A. M. Rubenchik, P. J. Depond, and W. E. King, "Denudation of metal powder layers in laser powder bed fusion processes," *Acta Materialia*, vol. 114, pp. 33–42, 8 2016.

[96] A. Bandyopadhyay and K. D. Traxel, “Invited Review Article: Metal-additive manufacturing — Modeling strategies for application-optimized designs,” *Additive manufacturing*, vol. 22, p. 758, 8 2018.

[97] M. Franchetti and C. Kress, “An economic analysis comparing the cost feasibility of replacing injection molding processes with emerging additive manufacturing techniques,” *International Journal of Advanced Manufacturing Technology*, vol. 88, no. 9-12, pp. 2573–2579, 2017.

[98] A. Emelogu, M. Marufuzzaman, S. M. Thompson, N. Shamsaei, and L. Bian, “Additive manufacturing of biomedical implants: A feasibility assessment via supply-chain cost analysis,” *Additive Manufacturing*, vol. 11, pp. 97–113, 2016.

[99] L. Dall’Ava, H. Hothi, A. Di Laura, J. Henckel, and A. Hart, “3D printed acetabular cups for total hip arthroplasty: A review article,” *Metals*, vol. 9, no. 7, 2019.

[100] Vijay Meenaab, P. Kumara, P. Kalrab, and R. Sinha, “Additive manufacturing for metallic spinal implants: A systematic review,” *Annals of 3D Printed Medicine*, vol. 3, no. September, p. 100021, 2021.

[101] M. Niemeläinen, E. T. Skyttä, V. Remes, K. Mäkelä, and A. Eskelinen, “Total knee arthroplasty with an uncemented trabecular metal tibial component: A registry-based analysis,” *Journal of Arthroplasty*, vol. 29, pp. 57–60, 1 2014.

[102] C. Yoon, M. J. Chang, C. B. Chang, M. K. Song, J. H. Shin, and S. B. Kang, “Medial Tibial Periprosthetic Bone Resorption and Its Effect on Clinical Outcomes After Total Knee Arthroplasty: Cobalt-Chromium vs Titanium Implants,” *Journal of Arthroplasty*, vol. 33, pp. 2835–2842, 9 2018.

[103] D. S. Elliott, K. J. H. Newman, D. P. Forward, D. M. Hahn, B. Ollivere, K. Kojima, R. Handley, N. D. Rossiter, J. J. Wixted, R. M. Smith, and C. G. Moran, “A unified theory of bone healing and nonunion,” *The Bone & Joint Journal*, vol. 98-B, pp. 884–891, 7 2016.

[104] S. Ghouse, N. Reznikov, O. R. Boughton, S. Babu, K. G. Ng, G. Blunn, J. P. Cobb, M. M. Stevens, and J. R. Jeffers, “The design and in vivo testing of a locally stiffness-matched porous scaffold,” *Applied Materials Today*, vol. 15, pp. 377–388, 6 2019.

[105] M. J. Munford, K. C. G. Ng, and J. R. T. Jeffers, “Mapping the Multi-Directional Mechanical Properties of Bone in the Proximal Tibia,” *Advanced Functional Materials*, vol. 30, p. 2004323, 2020.

[106] Z. Wang, C. Wang, C. Li, Y. Qin, L. Zhong, B. Chen, Z. Li, H. Liu, F. Chang, and J. Wang, "Analysis of factors influencing bone ingrowth into three-dimensional printed porous metal scaffolds: A review," 9 2017.

[107] R. E. Laureijs, J. B. Roca, S. P. Narra, C. Montgomery, J. L. Beuth, and E. R. Fuchs, "Metal additive manufacturing: Cost competitive beyond low volumes," *Journal of Manufacturing Science and Engineering, Transactions of the ASME*, vol. 139, no. 8, pp. 1–9, 2017.

[108] P. Szymczyk-Ziółkowska, M. B. Łabowska, J. Detyna, I. Michalak, and P. Gruber, "A review of fabrication polymer scaffolds for biomedical applications using additive manufacturing techniques," *Biocybernetics and Biomedical Engineering*, vol. 40, no. 2, pp. 624–638, 2020.

[109] E. Maleki, S. Bagherifard, M. Bandini, and M. Guagliano, "Surface post-treatments for metal additive manufacturing: Progress, challenges, and opportunities," *Additive Manufacturing*, vol. 37, p. 101619, 2021.

[110] R. J. V. Arkel, S. Ghouse, P. E. Milner, and J. R. T. Jeffers, "Additive manufactured push-fit implant fixation with screwstrength pull out," vol. 36, no. 5, pp. 1508–1518, 2017.

[111] J. Will, R. Melcher, C. Treul, N. Travitzky, U. Kneser, E. Polykandriotis, R. Horch, and P. Greil, "Porous ceramic bone scaffolds for vascularized bone tissue regeneration," *Journal of Materials Science: Materials in Medicine*, vol. 19, no. 8, pp. 2781–2790, 2008.

[112] S. Ghouse, S. Babu, K. Nai, P. A. Hooper, and J. R. Jeffers, "The influence of laser parameters, scanning strategies and material on the fatigue strength of a stochastic porous structure," *Additive Manufacturing*, vol. 22, pp. 290–301, 2017.

[113] S. Ghouse, R. N. Oosterbeek, A. T. Mehmood, F. Vecchiato, D. Dye, and J. R. Jeffers, "Vacuum Heat Treatments of Titanium Porous Structures," *Additive Manufacturing*, vol. 47, p. 102262, 2021.

[114] B. Van Hooreweder, Y. Apers, K. Lietaert, and J. P. Kruth, "Improving the fatigue performance of porous metallic biomaterials produced by Selective Laser Melting," *Acta Biomaterialia*, vol. 47, pp. 193–202, 1 2017.

[115] A. Burr, T. Persenot, P. T. Doutre, J. Y. Buffiere, P. Lhuissier, G. Martin, and R. Dendievel, "A numerical framework to predict the fatigue life of lattice structures built by additive manufacturing," *International Journal of Fatigue*, vol. 139, p. 105769, 10 2020.

[116] D. Ren, S. Li, H. Wang, W. Hou, Y. Hao, W. Jin, R. Yang, R. D. K. Misra, and L. E. Murr, “Fatigue behavior of Ti-6Al-4V cellular structures fabricated by additive manufacturing technique,” *Journal of Materials Science & Technology*, vol. 35, pp. 285–294, 2 2019.

[117] D. Zhao, H. Liang, C. Han, J. Li, J. Liu, K. Zhou, C. Yang, and Q. Wei, “3D printing of a titanium-tantalum Gyroid scaffold with superb elastic admissible strain, bioactivity and in-situ bone regeneration capability,” *Additive Manufacturing*, vol. 47, p. 102223, 11 2021.

[118] D. Mahmoud, K. S. Al-Rubaie, and M. A. Elbestawi, “The influence of selective laser melting defects on the fatigue properties of Ti6Al4V porosity graded gyroids for bone implants,” *International Journal of Mechanical Sciences*, vol. 193, p. 106180, 3 2021.

[119] A. Tridello, J. Fiocchi, C. Biffi, G. Chiandussi, M. Rossetto, A. Tuissi, and D. Paolino, “Effect of microstructure, residual stresses and building orientation on the fatigue response up to 109 cycles of an SLM AlSi10Mg alloy,” *International Journal of Fatigue*, vol. 137, p. 105659, 8 2020.

[120] A. Zargarian, M. Esfahanian, J. Kadkhodapour, and S. Ziaei-Rad, “Numerical simulation of the fatigue behavior of additive manufactured titanium porous lattice structures,” *Materials Science and Engineering: C*, vol. 60, pp. 339–347, 3 2016.

[121] A. A. Zadpoor, “Mechanical performance of additively manufactured meta-biomaterials,” *Acta Biomaterialia*, vol. 85, pp. 41–59, 2019.

[122] P. Tyagi, T. Goulet, C. Riso, R. Stephenson, N. Chuenprateep, J. Schlitzer, C. Benton, and F. Garcia-Moreno, “Reducing the roughness of internal surface of an additive manufacturing produced 316 steel component by chempolishing and electropolishing,” *Additive Manufacturing*, vol. 25, pp. 32–38, 1 2019.

[123] Carlos Navarro Pintado, Jesús Vázquez, Jaime Domínguez, Antonio Periñán, Marta Herrera García, Fernando Lasagni, Simon Bernarding, Sebastian Slawik, Frank Mücklich, Francisco Boby, and Lloyd Hackel, “Effect of surface treatment on the fatigue strength of additive manufactured Ti6Al4V alloy,” *Frattura ed Integrità Strutturale*, vol. 14, pp. 337–344, 5 2020.

[124] M.-W. Wu, J.-K. Chen, B.-H. Lin, and P.-H. Chiang, “Improved fatigue endurance ratio of additive manufactured Ti-6Al-4V lattice by hot isostatic pressing,” *Materials & Design*, vol. 134, pp. 163–170, 11 2017.

[125] A. du Plessis and E. Macdonald, “Hot isostatic pressing in metal additive manufacturing: X-ray tomography reveals details of pore closure,” *Additive Manufacturing*, vol. 34, p. 101191, 8 2020.

[126] A. A. Popovich, V. S. Sufiiarov, E. V. Borisov, I. A. Polozov, D. V. Masaylo, and A. V. Grigoriev, "Anisotropy of mechanical properties of products manufactured using selective laser melting of powdered materials," *Russian Journal of Non-Ferrous Metals*, vol. 58, pp. 389–395, 7 2017.

[127] E. Maleki, S. Bagherifard, M. Bandini, and M. Guagliano, "Surface post-treatments for metal additive manufacturing: Progress, challenges, and opportunities," *Additive Manufacturing*, vol. 37, p. 101619, 1 2021.

[128] A. A. Zadpoor, "Mechanical performance of additively manufactured meta-biomaterials," *Acta Biomaterialia*, vol. 85, pp. 41–59, 2 2019.

[129] C. M. Lawrie, M. Schwabe, R. M. Nunley, R. L. Barrack, and A. Pierce, "The cost of implanting a cemented versus cementless total knee arthroplasty," *Bone and Joint Journal*, vol. 101 B, pp. 61–63, 2019.

[130] P. F. Sharkey, P. M. Lichstein, C. Shen, A. T. Tokarski, and J. Parvizi, "Why are total knee arthroplasties failing today-has anything changed after 10 years?," *Journal of Arthroplasty*, vol. 29, pp. 1774–1778, 4 2013.

[131] J. C. J. Webb and R. F. Spencer, "The role of polymethylmethacrylate bone cement in modern orthopaedic surgery," *The Journal of Bone and Joint Surgery. British volume*, vol. 89-B, pp. 851–857, 7 2007.

[132] S. Konan, M. P. Abdel, and F. S. Haddad, "Cemented versus uncemented hip implant fixation: Should there be age thresholds?," *Bone and Joint Research*, vol. 8, no. 12, pp. 604–607, 2019.

[133] K. A. Mann, M. A. Miller, C. L. Pray, N. Verdonschot, and D. Janssen, "A new approach to quantify trabecular resorption adjacent to cemented knee arthroplasty," *Journal of Biomechanics*, vol. 45, pp. 711–715, 2 2012.

[134] Y. Tyson, O. Rolfson, J. Kärrholm, N. P. Hailer, and M. Mohaddes, "Uncemented or cemented revision stems? Analysis of 2,296 first-time hip revision arthroplasties performed due to aseptic loosening, reported to the Swedish Hip Arthroplasty Register," *Acta Orthopaedica*, vol. 90, pp. 421–426, 9 2019.

[135] R. J. van Arkel, S. Ghouse, P. E. Milner, and J. R. Jeffers, "Additive manufactured push-fit implant fixation with screw-strength pull out," *Journal of Orthopaedic Research*, vol. 36, pp. 1508–1518, 5 2018.

[136] S. Campi, S. J. Mellon, D. Ridley, B. Foulke, C. A. F. Dodd, H. G. Pandit, and D. W. Murray, "Optimal interference of the tibial component of the cementless Oxford Unicompartmental Knee Replacement," *Bone & Joint Research*, vol. 7, pp. 226–231, 3 2018.

[137] S. Berahmani, D. Janssen, S. van Kessel, D. Wolfson, M. de Waal Malefijt, P. Buma, and N. Verdonschot, "An experimental study to investigate biomechanical aspects of the initial stability of press-fit implants," *Journal of the Mechanical Behavior of Biomedical Materials*, vol. 42, pp. 177–185, 2 2015.

[138] T. Hiranaka, R. Yoshikawa, K. Yoshida, K. Michishita, T. Nishimura, S. Nitta, K. Takashiba, and D. Murray, "Tibial shape and size predicts the risk of tibial plateau fracture after cementless unicompartmental knee arthroplasty in Japanese patients," *The Bone & Joint Journal*, vol. 102-B, pp. 861–867, 7 2020.

[139] J. D. Voigt and M. Mosier, "Hydroxyapatite (HA) coating appears to be of benefit for implant durability of tibial components in primary total knee arthroplasty," *Acta Orthopaedica*, vol. 82, pp. 448–459, 8 2011.

[140] K. A. Zweymuller, F. K. Lintner, and M. F. Semlitsch, "Biologic fixation of a press-fit titanium hip joint endoprosthesis," *Clinical Orthopaedics and Related Research*, no. 235, pp. 195–206, 1988.

[141] T. Masuda, P. K. Yliheikkilä, D. a. Felton, and M. S. L. F. Cooper, "Generalizations Regarding the Process and Phenomenon of Osseointegration. Part I . In Vivo Studies," *The International journal of oral maxillofacial implants*, vol. 13, no. 1, pp. 17–29, 1998.

[142] T. Albrektsson and C. Johansson, "Osteoinduction, osteoconduction and osseointegration," *European Spine Journal*, vol. 10, no. S2, pp. S96–S101, 2001.

[143] J. R. Davey and W. H. Harris, "Loosening of Cobalt Chrome Beads from a Porous-Coated Acetabular Component," *Clinical Orthopaedics and Related Research*, vol. 231, pp. 97–102, 1988.

[144] K. Mustafa, A. Wennerberg, J. Wroblewski, K. Hultenby, B. S. Lopez, and K. Arvidson, "Determining optimal surface roughness of TiO2 blasted titanium implant material for attachment, proliferation and differentiation of cells derived from human mandibular alveolar bone," *Clinical Oral Implants Research*, vol. 12, no. 5, pp. 515–525, 2001.

[145] L. Marinucci, S. Balloni, E. Becchetti, S. Belcastro, M. Guerra, M. Calvitti, C. Lull, E. M. Calvi, and P. Locci, "Effect of Titanium Surface Roughness on Human Osteoblast Proliferation and Gene Expression In Vitro.," *International Journal of Oral & Maxillofacial Implants*, vol. 21, no. 5, pp. 719–725, 2006.

[146] N. Sykaras, A. M. Iacopino, V. A. Marker, R. G. Triplett, and R. D. Woody, "Implant Materials, Designs, and Surface Topographies: Their Effect on Osseointegration. A Literature Review.," *International Journal of Oral & Maxillofacial Implants*, vol. 15, no. Sep, pp. 675–690, 2000.

[147] A. Barfeie, J. Wilson, and J. Rees, "Implant surface characteristics and their effect on osseointegration," *British Dental Journal*, vol. 218, no. 9, pp. 512–519, 2015.

[148] J. Raphel, M. Holodniy, S. B. Goodman, and S. C. Heilshorn, "Multifunctional coatings to simultaneously promote osseointegration and prevent infection of orthopaedic implants," *Biomaterials*, vol. 84, pp. 301–314, 4 2016.

[149] N. Kohli, J. C. Stoddart, and R. J. van Arkel, "The limit of tolerable micromotion for implant osseointegration: a systematic review," *Scientific Reports*, vol. 11, no. 1, pp. 1–11, 2021.

[150] L. Jones, L. Timmie Topoleski, and A. Tsao, "Biomaterials in orthopaedic implants," in *Mechanical Testing of Orthopaedic Implants*, pp. 17–32, Elsevier, 2017.

[151] I. Sanli, J. J. C. Arts, and J. Geurts, "Clinical and Radiologic Outcomes of a Fully Hydroxyapatite-Coated Femoral Revision Stem: Excessive Stress Shielding Incidence and its Consequences," *Journal of Arthroplasty*, vol. 31, no. 1, pp. 209–214, 2016.

[152] S. J. Hollister, "Porous scaffold design for tissue engineering," *Nature Materials*, vol. 4, no. 7, pp. 518–524, 2005.

[153] N. Reznikov, O. R. Boughton, S. Ghouse, A. E. Weston, L. Collinson, G. W. Blunn, J. R. Jeffers, J. P. Cobb, and M. M. Stevens, "Individual response variations in scaffold-guided bone regeneration are determined by independent strain- and injury-induced mechanisms," *Biomaterials*, vol. 194, pp. 183–194, 2 2019.

[154] L. J. Gibson and M. F. Ashby, *Cellular solids: Structure and properties, second edition*. 2014.

[155] X. Chen, T. Lian, B. Zhang, Y. Du, K. Du, N. Xiang, D.-W. Jung, G. Wang, and A. Osaka, "Design and Mechanical Compatibility of Nylon Bionic Cancellous Bone Fabricated by Selective Laser Sintering," *Materials (Basel)*, vol. 14, no. 9, p. 1965, 2021.

3 Mapping Mechanical Properties in the Tibia

Abstract

The remodeling behavior of bone is influenced by its mechanical environment. By mapping bone's mechanical properties in detail, orthopedic implants which respect its mechanobiology could harness remodeling to improve patient outcomes. Multiaxial apparent modulus and strength of cadaveric proximal tibial bone are mapped and predicted from computed tomography (CT) derived apparent density. Group differences are identified from testing order, subchondral depth, condyle and sub-meniscal bone with covariates; age and gender. Axial modulus is 1.5 times greater than the transverse modulus. Differences were quantified for density and multiaxial modulus across all subchondral depths, where 60% of transverse modulus variation was predicted by density within subgroups for each subchondral depth. Medial axial modulus was 1.3 times greater than the lateral side. Compared to the most proximal region, lateral axial modulus halves over a 25mm depth whilst remaining constant on the medial side. Density explains 75% of variation when grouped by subchondral depth and condyle. Yield strength is well-predicted across all test directions, with density predicting 81% of axial strength variation and no differences over subchondral depth. A quantified mapping of bone multiaxial modulus based on condyle and subchondral depth is shown for the first time in a clinically viable protocol using conventional CT.

Credited authors include M.J. Munford, K.C.G. Ng, J.R.T. Jeffers [1]

[1]This chapter has been published in Advanced Functional Materials, 2020, and presented at a the British Orthopaedic Research society 2020 annual meeting. This work was nominated a for the ICORS best poster award, Orthopaedic Research Society 2021.

3.1 Introduction

Bone is a remarkable dynamic material with remodelling mechanisms which are closely linked to the its strain response. These are well described as Frost's mechanostat [1], Wollf's Law and Perren's strain theory [2], all of which propose that bone mechanical properties can be controlled by its mechanical environment. This can explain desirable results such as bone formation within a scaffold [3], fracture healing [4] or undesirable results such as stress shielding and bone resorption [5]. Given the multi-axial loading of many bones in the musculoskeletal system, in order to control the mechanical environment, we must understand better whether established density modulus models capture anisotropic mechanical properties of the material. The proximal tibia is a site of popular interest for arthroplasty solutions, owing to the prevalence of osteoarthritis in the knee joint. Common successful procedures include total knee arthroplasty, partial knee arthroplasty, patellofemoral arthroplasty and tibial osteotomy. Although these procedures are all effective, none of them take advantage of the mechanoresponse of bone, indeed they do the opposite and often cause bone resorption [6, 7]. There may be an opportunity to harness bone's natural mechanoresponse by invoking the correct localised strain. In order to do this it is necessary to know and be able to predict mechanical properties, such as apparent modulus and strength, in a clinically viable workflow. Modelling the mechanical properties of bone is made difficult given its structural anisotropy and mechanical inhomogeneity [8]. With such complex behaviour it is useful to be able to simply express mechanical properties as a function of density, accounting for spatial variation and whether the bone is trabecular or cortical [9]. This can be found from quantitative quantified computed tomography (qCT) [10]. A broad range of power-law models predicting apparent modulus and strength of bone from apparent density exist in literature, however these are limited to uniaxial testing [11, 12]. Some authors have shown that consideration and quantification of orthotropic properties in the proximal tibia may be necessary [13, 14]. Comparing existing models for axial apparent modulus can yield variations in apparent modulus prediction of a factor of 15 even within the same anatomical site [15, 16]. The aim of this study is to provide a detailed map of bone apparent modulus and strength in the proximal tibia, in three anatomically relevant directions, to aid the control of remodelling and the strain response of bone. Mechanical properties will be discussed in terms of their variation across the proximal tibia and their dependencies on apparent density and other factors.

3.2 Material and Methods

3.2.1 Sample Preparation

All human tissue in this study was obtained from seven donors with no prior lower limb pathologies, traumas, surgeries or osteoarthritis. The group of donors spanned a range of ages from 34 to 65, contained 5 females and 2 males and was split with 4 left and 3 right sided specimens. Tissue was frozen within 24 hours post-mortem and denuded to the bone. Ethical permission was granted by the Imperial College Healthcare Tissue Bank Review Committee under a UK Human Tissue Authority Licence 12275.

A conventional CT scanner (SOMATOM Definition AS; SIEMENS AG) was used to image all specimens, with a 5 material calibration phantom (Model 3; Mindways Software Inc). Following scanning, 3D models of the specimens were segmented from the scan slices using image processing software (Mimics, Materialise) as in Figure 3.1a.

Each sample was optimally packed with 9mm side length cubic cores aligned to the mechanical axes of the tibial specimens using Rhinoceros 6 and Grasshopper (Robert McNeel and Associates), shown in Figures 3.1b and 3.1c [15]. The coordinate axis of each specimen was set at the centre of the tibial plateau with the X axis along the P-A (posterior-anterior) direction, the Y axis along the M-L (medial-lateral) direction and the Z axis along the D-P (distal-proximal) mechanical axis, with vectors defined as per Majstorovic et al. [15]. Specimen specific cutting guides, as in Figure 3.1d, were generated to allow the accurate removal of cubic cores from the proximal tibia over 3 subchondral depths below the tibial plateau.

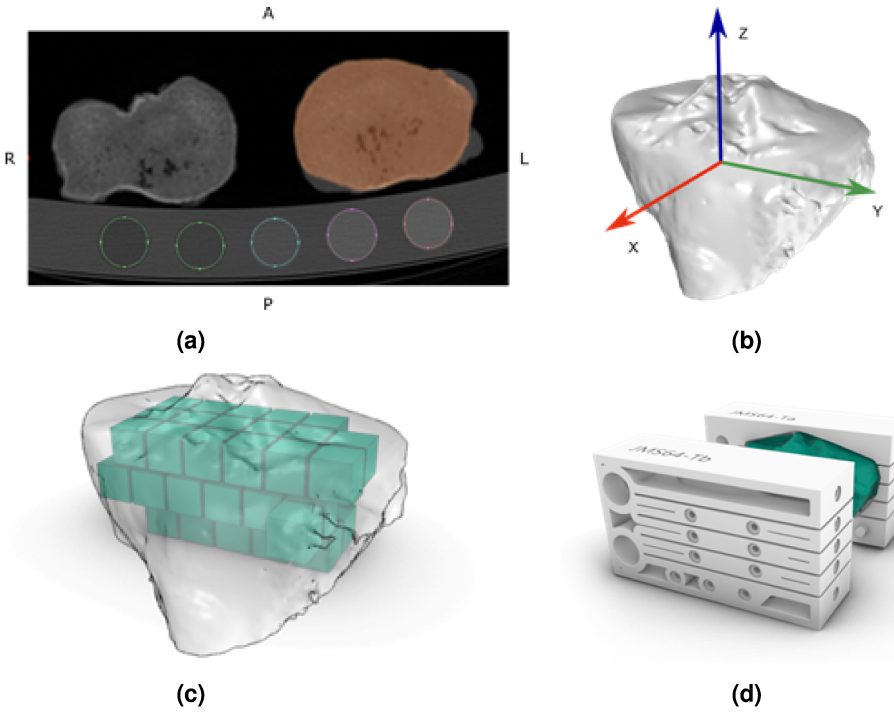


Figure 3.1: Summary of methods for measurement of bone density from CT scans. 3.1a Segmented CT scan of 2 tibia specimens with a 5 material calibration phantom. 3.1b Mechanical coordinate frame defined for each specimen with axes based on anatomical landmarks. 3.1c 3 layers of cores (green) packed within the specimen and aligned to the mechanical axes. 3.1d Specimen specific guides to secure each specimen (green) during cutting.

Cutting guides were additively manufactured in medical grade Nylon (PA 2200) using an EOS P110 (EOS, Warwick, UK). Tibial specimens were clamped in their respective cutting guides and cores cut from them with a pathology saw (Exakt, Oklahoma, US) along predetermined slots with no fine grinding. Cores were measured to have mean side lengths of 8.90mm $\pm$ 0.15mm.

In total, 195 cores were removed from the 7 specimens as per Table 3.1.

The cores had dimensions chosen to comply with existing protocols for testing porous structures. Cores were removed from both the medial and lateral sides of the proximal tibia, across 3 layers of material spanning material 30mm below the tibial plateau. Specimens were kept in gauze saturated in phosphate buffered saline (PBS), to ensure they remained hydrated at all times, and stored at -30 degrees Celsius until mechanical testing [16].

Table 3.1: Summary of the 7 donors and extracted cores. All specimens were fresh frozen with minimised freeze-thaw cycles.

Specimen	Age	Gender	Number of cores (n) for each sub-plateau depth			
			5 mm	15 mm	25 mm	Pooled
1	34	F	11	9	6	26
2	61	M	20	13	5	38
3	50	F	15	15	10	40
4	32	F	14	1	3	18
5	59	F	14	3	3	20
6	65	M	17	8	0	25
7	41	F	14	8	6	28
Total			105	57	33	195

3.2.2 Quantifying Bone Density from CT Scan

Inclusion of a phantom in the CT scans allowed for a robust calibration of qCT Hounsfield units (HU) to apparent density. This process followed the methods demonstrated by Ng et al. [6, 17, 18] whereby regression of the HU values for the phantom materials in the scan and the known densities of the phantom results in a linear relationship between HU and calibrated density (ρ_{CT}) when water content and displaced volume of phosphate in the phantom is accounted for. This calibration yields calibrated density values independent of any material settings used during imaging.

Ash density and subsequently apparent density can be determined from the calibrated density as per Equations 3.1 and 3.2 [19, 20].

$$\rho_{Ash} = 1.22\rho_{CT} + 52.6 \tag{3.1}$$

$$\rho_{App} = 1.64\rho_{Ash} + 10 \tag{3.2}$$

3.2.3 Specimen Testing

A materials testing machine (Instron 8872) with a 10kN load cell was used to perform quasi-static compression testing at an extension rate of 2 mm/min, which corresponds to a strain rate within standard limits [16].

Displacement was measured using linear variable differential transformers (LVDTs) to reduce any compliance effects from the test apparatus. A sampling rate of 30Hz was used. The platens of the machine were lubricated to reduce any frictional effects. Stress-strain curves were obtained using the individual macro dimensions of each specimen.

An initial sample of specimens were tested to failure to establish a relationship between density and yield stress of the cores. Cores were tested in all 3 orthogonal directions (x, y, z) sequentially with randomised order of test directions. The loading regime included a hysteresis loop to account for localised plastic behaviour within the porous structure. For half of the specimens this was carried out from 40% of the yield stress (σ_{40}), to 20% of the yield stress (σ_{20}) and then back to σ_{40}. Specimens were tested in this way along each test direction, with the last test of each specimen undergoing a hysteresis loop from σ_{40} to σ_{20} and then being taken to failure as per the traces in Figure 3.2.

The elastic moduli were then calculated using a linear regression analysis of the hysteresis loop. Yield strength was determined as the 1% offset stress. A preliminary dataset was compressed to 50% strain at 2mm/min to find the required reference yield stresses. Preliminary testing established that testing up to σ_{40} would not affect the results for elastic modulus or yield strength when testing subsequent directions.

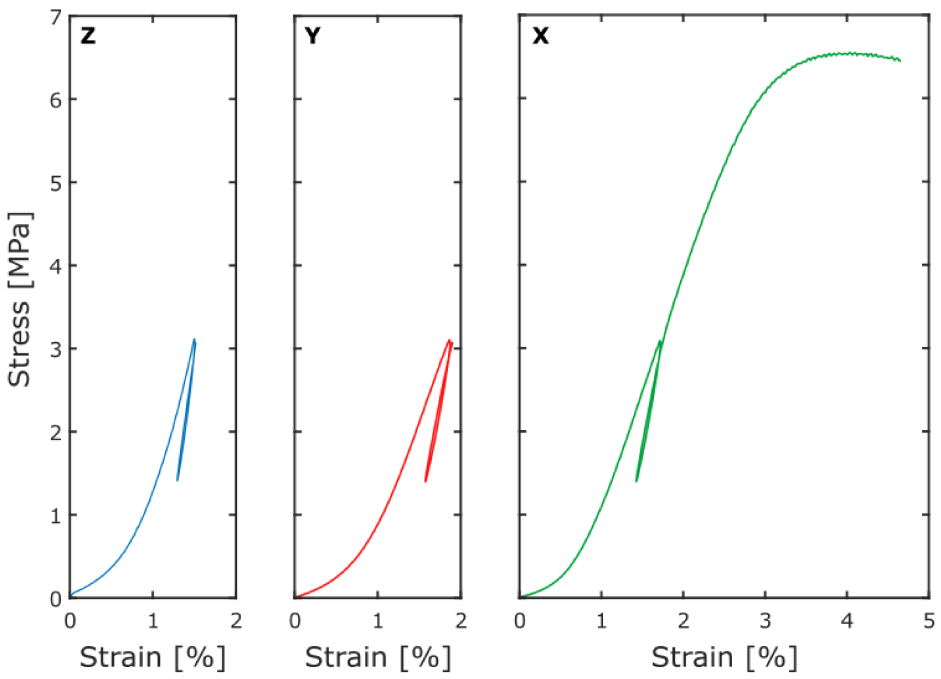


Figure 3.2: Example stress-strain traces for multiaxial sample testing. Traces for one sample tested in the order; Z, Y, X. Hysteresis loops were taken between σ_{40} and σ_{20} and the sample was yielded on the final test.

In total 343 data points were recorded for apparent modulus, 100 tested in the X direction, 101 in the Y direction and 142 tested in the Z direction. Similarly for yield

stress, 183 data points were recorded, 76 in the X direction, 74 in the Y direction and 33 in the Z direction.

3.2.4 Statistical Analysis and Model Fitting

One-way analysis of variance (ANOVA) tests were performed to determine which group factors significantly affected the target variables [21]. The group factors considered were specimen age, gender, order of testing, subchondral bone depth, which condyle the specimen was taken from and its location in the metaphyseal cortex. Target variables were the apparent density and both apparent modulus and strength in the X, Y and Z direction. Independent sample t-tests were used to determine whether the differences in the target variables, apparent modulus and strength in the X, Y and Z directions, were statistically significant. Holm-Bonferroni post-hoc tests were applied to correct significance values. Significance was indicated by a p value < 0.05, with partial eta squared values to indicate small (μ^2 > 0.01), medium (μ^2 > 0.06), and large (μ^2 > 0.14) effect sizes.

Of the 195 extracted cores, sequential testing of each direction resulted in 100, 101 and 142 data points for apparent modulus in the X, Y and Z directions respectively. Similarly, for yield strength, 76, 74 and 33 data points were collected in the X, Y and Z directions respectively. Based on this data, the commonly implemented power law relationships predicting apparent modulus and strength in terms of apparent density were fit for each test direction, grouped by those variables which proved to be significant in the ANOVA.

3.3 Results

3.3.1 Mechanical Data for Apparent Modulus and Strength

A total of 195 measurements were collected for apparent modulus and 194 measurements were collected for yield strength across all 3 test directions, with the range of values summarised in Table 3.2. Observed apparent density ranged from 106 to 957 $mgcm^3$.

Table 3.2: Summary of the calculated apparent density and measured apparent moduli for all cores. Mean ± standard deviation (SD).

Mechanical Property	Density Range [mg/cm3]	n	Test Direction		
			X	Y	Z
Apparent Modulus [MPa]	106 – 957	195	53 - 1302	21 - 1490	81 - 1500
Yield Strength [MPa]		194	0.188 – 4.60	0.139 – 3.53	0.257 – 15.9

3.3.2 Apparent Modulus

Performing T-tests between all combinations of the 3 test directions for the apparent modulus data (summarised in Table 3.3) showed that the mean apparent modulus in the Z direction is 68% greater than that in the X direction ($p < 0.001$) and 40% greater than that in the Y direction ($p < 0.001$). No difference was observed between mean apparent modulus in the X and Y direction ($p = 0.07$).

Table 3.3: Observed apparent modulus for each test direction. Mean $\pm$ standard deviation (SD).

Test Direction		X	Y	Z
N		100	101	142
Apparent Modulus [GPa]	Mean	0.304	0.362	0.509
	SD	0.260	0.300	0.257

For data along all 3 directions, regression analysis showed that power-law models fit between apparent density and apparent modulus had good correlation, with at least 52% of variation explained by apparent density and root mean square error (RMSE) of at most 0.05 MPa. Apparent modulus in the Z direction was most accurately predicted by apparent density for the observed data (n = 139) with R^2 = 0.57 and RMSE of 0.042 MPa. These models are summarised in Table A.1.

Analysis of variance

The ANOVA indicated that the apparent density and apparent modulus in all three tested directions differed across subchondral depths (Table 3.4). Similarly, whether the specimen was taken from the medial or lateral condyle had an effect on the apparent modulus in the Z direction. This data is summarised in Table 3.4. We did not detect an effect of specimen age, order of testing and whether the bone was beneath the menisci on the bone apparent density or apparent modulus across any test direction (Table 3.4).

Table 3.4: Statistical significance and effect sizes for each group factor on each target variable. Green indicates statistical significance ($p < 0.05$). Effect sizes: *$\mu^2 > 0.06$ and **$\mu^2 > 0.14$.

Factor	Apparent Density	Apparent Modulus		
		X	Y	Z
Subchondral Depth	<0.001**	<0.001**	<0.001**	0.001**
Condyle	0.111	0.381	0.228	0.011*
Sub Menisci	0.094	0.482	0.331	0.270
Gender	0.447	0.680	0.235	0.055
Age	0.802	0.546	0.458	0.121
Order of testing	-	0.524	0.607	0.303

Regression Modelling: All test directions by subchondral depth

Mean apparent modulus in the X direction of bone in the most proximal slice was 2.7 times greater than bone 10 mm more distal and 3.1 times greater than that taken 25 mm below the tibial plateau. Mean apparent modulus in the Y direction of bone in the most proximal slice was 1.3 times greater than bone 10 mm more distal and 3.5 times greater than that taken 25 mm below the tibial plateau. Mean apparent modulus in the Z direction of bone in the most proximal slice was 1.59 times greater than bone 10 mm more distal and 1.6 times greater than that taken 25 mm below the tibial plateau (Figure 3.3). Within the data for each subchondral depth, apparent density was well correlated to the apparent modulus as per Figure 3.4 and the statistics in Tables A.2 A2 and A.3.

Apparent density-modulus relationships were formed for the collected data for X, Y and Z apparent modulus, grouped by the significant factor, subchondral depth. Apparent density correlated well with Apparent modulus across all test directions, as shown in Figure 3.3. Relationships for the X and Y directions explained at least 42% and 49% of the variations in apparent moduli in the respective directions. When grouped by subchondral depth, correlation coefficients increased to an average of 52% and 57%, indicated in Figure 3.3. For both transverse test directions RMSE were comparable to models in literature. The models are summarised in Tables A.2 A2 and A.3.

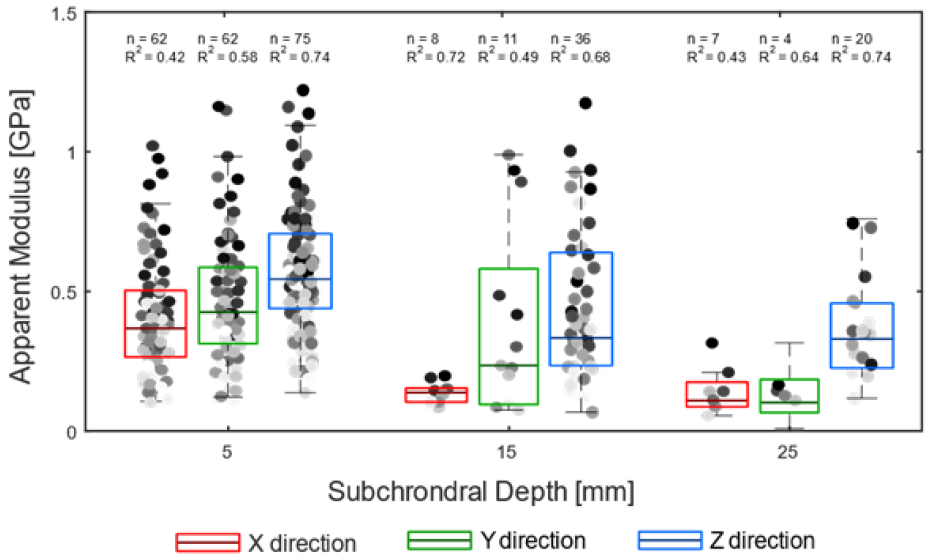


Figure 3.3: Multiaxial apparent modulus with subchondral depth. Boxplots for apparent modulus across all 3 test directions grouped by subchondral depth, with modulus mean and quartiles indicated. Marker colours correspond to apparent density, ranging from low (white) to high (black) density. n and R^2 values are indicated for density-modulus correlation.

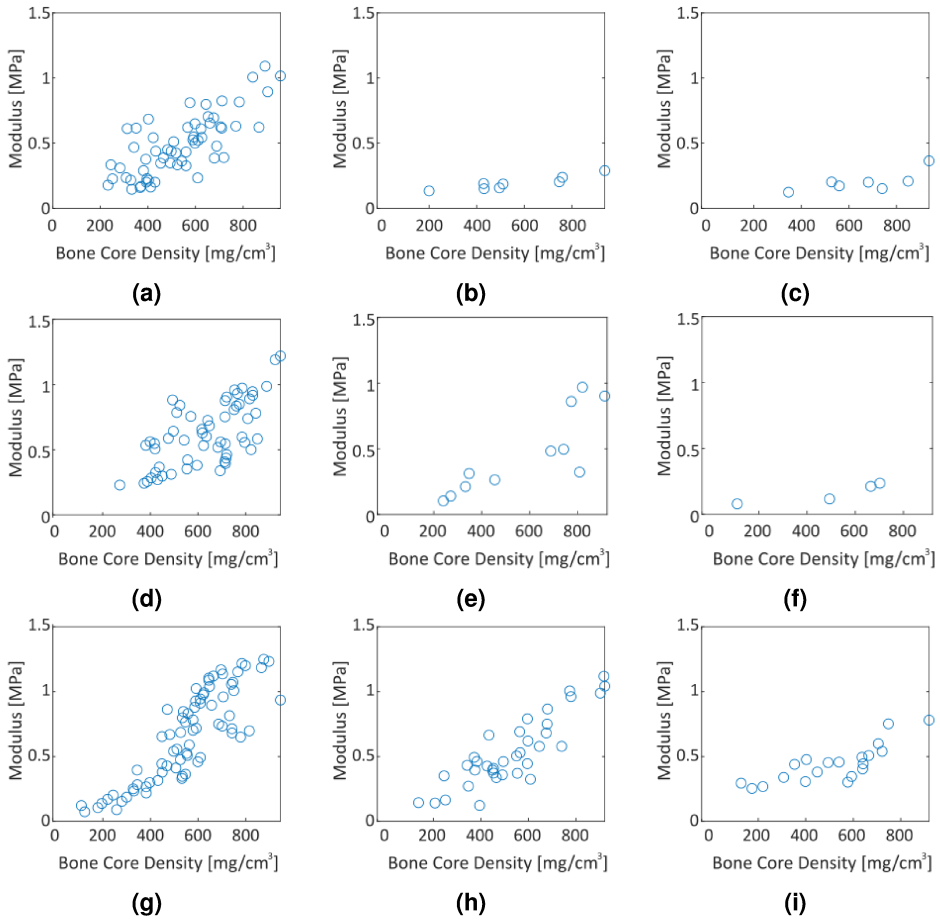


Figure 3.4: Multiaxial apparent modulus with subchondral depth correlated with bone density. Boxplots for X (3.4a, 3.4b and 3.4c), Y (3.4d, 3.4e and 3.4f) and Z (3.4g, 3.4h and 3.4i) apparent modulus grouped by subchondral depth. The first, second and third columns indicate cores taken from a subchondral depth of 5mm, 10mm and 15mm respectively. This data corresponds to the black and white shaded points in Figure 3.3.

Regression Modelling: Z direction by subchondral depth and condyle

Bone beneath the medial condyle proved on average to have an apparent modulus in the Z direction 33% more than bone of the same density beneath the lateral condyle ($p = 0.03$). Mean apparent modulus was observed to be relatively consistent in the medial condyle, with bone in the most proximal slice being 7% greater than bone 10 mm more distal and 15% greater than bone 25 mm more distal (Figure 3.5a). For the lateral condyle, mean apparent modulus in the Z direction of bone in the most proximal slice was 64% greater than bone 10 mm more distal and 93% greater than bone 25 mm more distal (Figure 3.5b).

Within these subgroups, apparent density was very well correlated to the apparent modulus as per the statistics in Figure 3.5, plots in Figure 3.6 and Table A.4.

Apparent density-modulus relationships were formed for the collected data, grouped by the significant factors; subchondral depth and condyle. These relationships explained at least 64% of the variation in data with root mean squared errors (RMSE) comparable to models in literature. Details of these models are summarised in Table A.4.

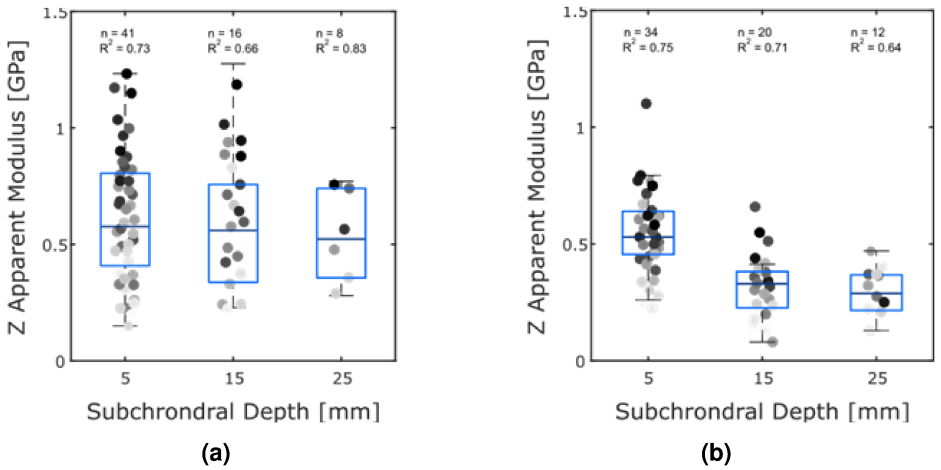


Figure 3.5: Medial and lateral axial apparent modulus. Boxplots for Z apparent modulus grouped by subchondral depth for the medial (3.5a) and lateral (3.5b) condyles, with modulus mean and quartiles indicated. Marker colours correspond to core apparent density, ranging from low (white) to high (black) density. n and R^2 values are indicated for density-modulus correlation.

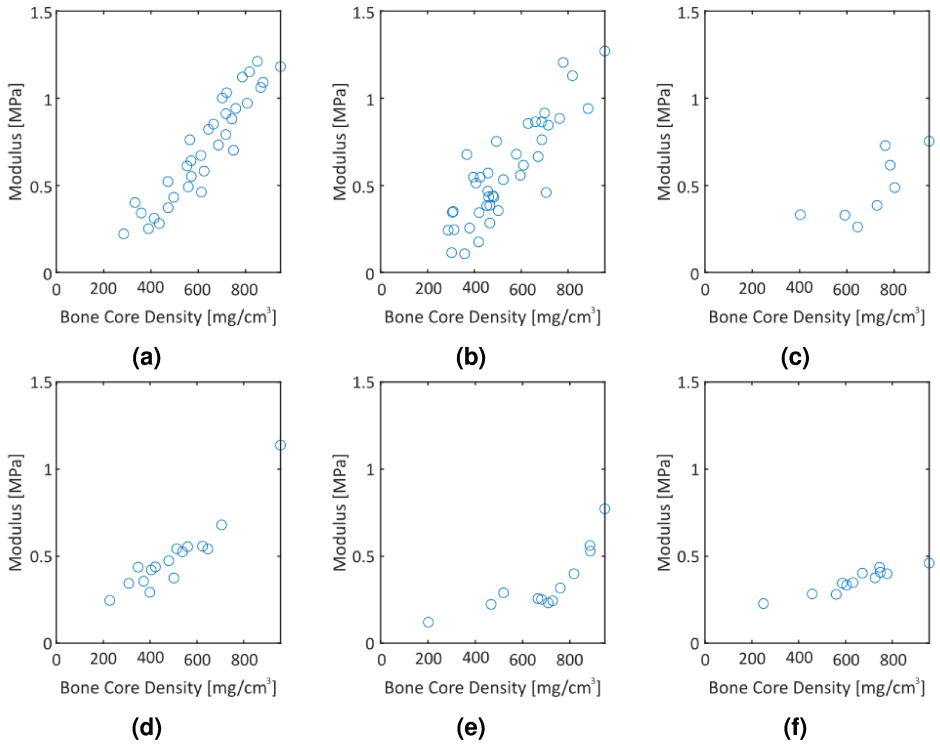


Figure 3.6: Medial and lateral axial apparent modulus correlated with bone density. Boxplots for Z apparent modulus grouped by subchondral depth for the medial (3.6a, 3.6b and 3.6c) and lateral (3.6d, 3.6e and 3.6f) condyles. The first, second and third columns indicate cores taken from a subchondral depth of 5mm, 10mm and 15mm respectively. This data corresponds to the black and white shaded points in Figure 3.5.

3.3.3 Yield Strength

None of the factor groups available in this study proved significant in explaining any variation between subgroups in the data for strength in X, Y and Z directions. Yield strength was predicted in all 3 test directions, with at least 65% of variation explained by apparent density and RMSE of at most 3.2 MPa (Figure 3.7). Apparent modulus in the Z direction was most accurately predicted by apparent density for the observed data (n = 33) with R^2 = 0.81 and RMSE of 3.2 MPa. The power law relationships in Figure 3.7 provided good models and had the model parameters in Table A.5.

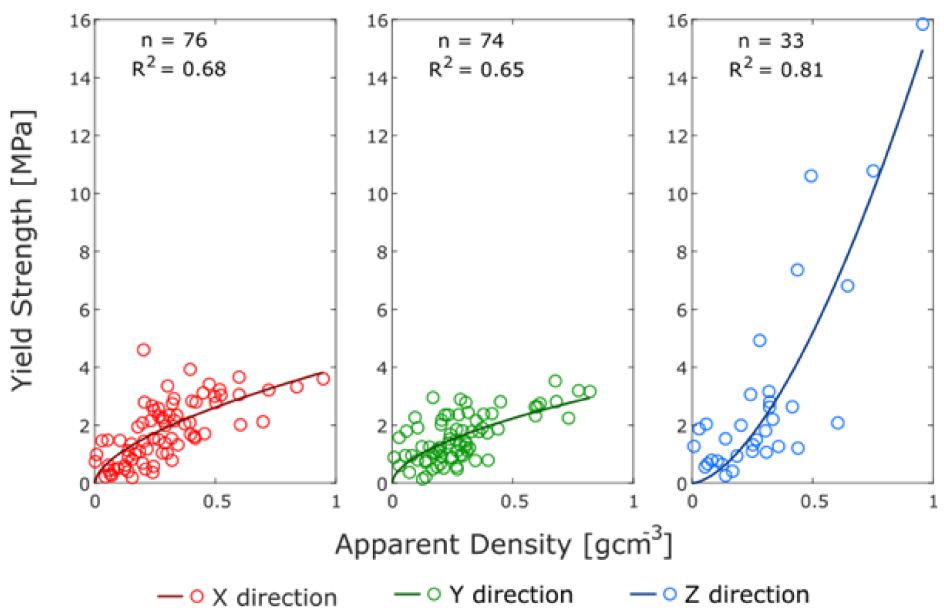


Figure 3.7: Multiaxial yield strength against apparent density. Data collected from testing across X, Y and Z directions.

3.4 Discussion

3.4.1 Summary of Results

This study quantified the distribution of cancellous bone mechanical properties in the proximal tibia. The most important finding was the material has orthotropic modulus and strength properties that depend on the location within the bone. Average apparent modulus and strength were 1.7 and 3 times respectively higher in the axial direction compared to the transverse directions. In the dominant axial direction, the bone was 1.3 times stiffer in the medial condyle than the lateral condyle. This was because the proximal cancellous bone in the medial condyle had an elastic modulus of 610 MPa that only decreased by about 10% over a 25 mm distal distance. In contrast, the proximal cancellous bone in the lateral condyle had an elastic modulus of 562 MPa that decreased by 50% over the same 25 mm distal distance. This map of cancellous bone apparent modulus and strength in axial and transverse directions is required in order to design implantable devices that can safely harness the exciting potential of bone's mechanoresponse.

This study also quantified the relationship between density and mechanical properties for cancellous bone in the proximal tibia. The best relationships were found in the axial direction where a power law relationship between apparent modulus and density yielded an R^2 coefficient of 0.75, but this required a different

power law for the medial and lateral condyle. A good power law relationship between density and yield strength in the axial direction was measured with an R^2 coefficient of 0.81. These density/modulus and density/strength relationships enable mechanical properties to be calculated from conventional clinical CT scans in order to tailor any implantable device to influence the local strain distribution in the cancellous bone surrounding the device, whilst not exceeding its strength. Such a device could then take advantage of mechanoresponse to actively increase the strength and modulus of the bone into which it is implanted.

3.4.2 Comparison to Literature

Numerous prior studies have reported power law relationships between bone density and apparent modulus, and our data compares well with prior work. We used the power law relationships of seven previous studies to predict axial modulus from our CT measured density values (Figure 3.8, Table 3.5). These predicted the apparent modulus value with R^2 correlation coefficients between 0.53 and 0.57 and RMSE between 106 MPa and 5,500 MPa. This is similar to our own data – if we used a single power law to describe the entire axial modulus/density relationship we get an R^2 value of 0.57 and RSME of 42 MPa. However, we improved this relationship by generating different power laws for the medial and lateral condyle to get an R^2 of 0.75 and RSME of 34 MPa for the medial side and R^2 of 0.74 and RSME of 14 MPa for the lateral side. These data, and those of the seven previous studies indicate that factors which cannot be detected in CT scans, such as bone collagen content, gait and diet affect these properties. Bone apparent density, trabecular volume, modulus, strength and strain energy are all affected by medication [22]. Furthermore, bone's ability to remodel changes with protein content and age, as osteocytes become senescent, which is likely to further contribute to the variation in properties observed in the data here [23].

It is noted that the majority of models in literature suggest a power-law with an exponent greater than 1, whereas the majority of models which has been fit here have an exponent less than 1. Porous material theory suggests that power-law relationships with an exponent less than 1 is indicative of axial deformation being dominant over bending deformation [7, 11]. Relationships of the yield strength of bone based on apparent density have not been documented extensively in literature, however, the range of values observed for strength are consistent with those recorded by Goldstein et al. [24]. Furthermore the relationships in Section 3.3.2 are again consistent with Wolff's law and bone remodelling [25, 26].

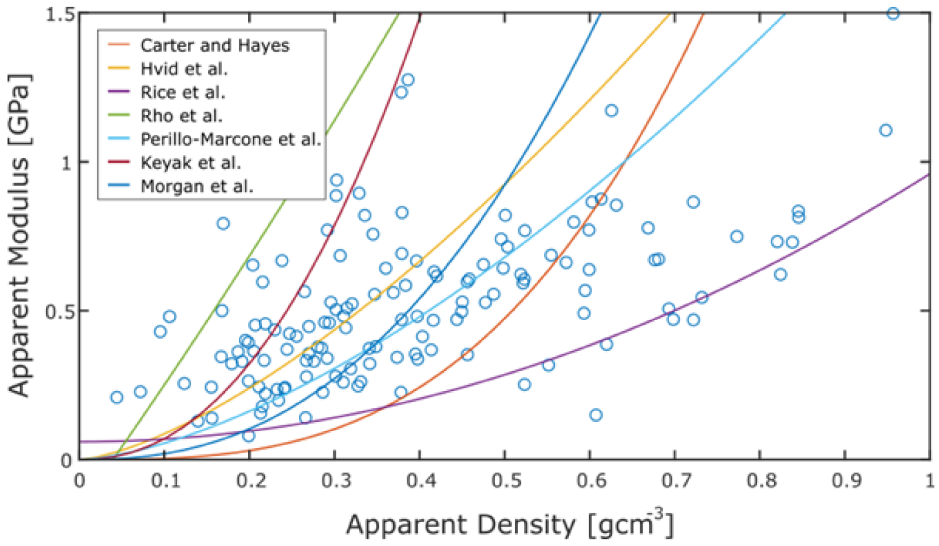


Figure 3.8: Comparison of data with existing literature. Models for observed bone apparent modulus data provide improved prediction compared to 7 commonly used power-law models.

Table 3.5: Comparison of power-law models found in literature to the data observed here. Values for the present study refer to grouped data for each condyle and subchondral depth.

Source	R^2	**RMSE** [MPa]
Carter and Hayes 1977	0.53	287
Hvid et al. 1989	0.56	207
Rice et al. 1988	0.55	126
Rho et al. 1993	0.57	1953
Perillo-Marone et al. 2003	0.56	106
Keyak et al. 1994	0.55	5500
Morgan et al. 2003	0.54	611
Present study	0.64-0.75	6-32

Relatively few studies have mapped cancellous bone apparent modulus and strength differences in regions across the tibia. Studies by Hvid and Hansen, Goldstein et al., Klever et al. and Ashman et al. observed modulus changes across the proximal tibia and these also found increased modulus in the medial condyle. The trends observed here suggest that the ratio of peak medial to lateral modulus ranges from 1.1 at the most proximal slice to 1.8 more distally, with a mean ratio of 1.3. This agrees with literature values for peak medial-lateral

ratio (averaged over all depths) of 1.7, 1.1 and 1.4 [24, 27–29]. Odgaard et al. observed an increase in strain response for bone more proximal in the tibia, which agrees with trends observed here [30]. Similarly, Goldstein et al., Klever et al. and Ashman et al. also imply a decrease in axial apparent modulus moving distally, but to a lesser extent as was found in this study. The results in this study agree with literature and are the first to quantify and show statistical differences between subchondral depths.

Axial (Z) apparent modulus of the proximal tibia has been recorded by numerous authors with values ranging from 2.5 - 3780 MPa, as per Table 2.1 [4, 31]. The range of apparent modulus values recorded in this study are well supported by those in the similar studies in literature summarised in Table 2.1). It is noted that a number of studies, such as Garg and Walker, Goldstein, Hvid and Jensen and Lindahl et al., report apparent modulus to be significantly less than that in this study [31–33]. Similarly, studies such as those from Odgaard and Linde, Keveany et al. and Ashman et al. report apparent modulus values which are significantly greater than those shown here [4, 29, 34]. These values may be larger due to differences in experimental method, small samples sizes of predominantly young males or inclusion of cortical bone regions within cores. Studies such as those by Johnston et al., Nazemi et al. and Ashman et al. have found apparent modulus from alternative methods such as indentation testing, FE combined with neural networks or ultrasound testing. In all cases, the range of results was similar to that found here with from compression testing, although values from Nazemi et al. and Ashman et al. were slightly less and greater, respectively, than those in this study [29, 35, 36].

Most previous studies have assumed isotropic properties for bone [8], however, the data collected here suggests that an orthotropic relationship is more suitable. Works by Williams and Lewis, Klever et al., Linde et al., Ciarelli et al. and Ashman et al. have also quantified orthogonal properties of the proximal tibia [28, 29, 37–39]. All such studies, apart from that by Rincon-Kohli et al., suggest an orthotropic modulus [40]. In previous work, apparent modulus in the transverse directions is reported between 51 and 553 MPa with a degree of anisotropy ranging from 1.1 to 4.3 which is not analysed for variation across the tibial plateau. The anisotropy and transverse moduli data observed here agrees broadly with that in literature, as well as indicating that average anisotropy is greater on the medial side than the lateral side (1.9 compared to 1.4). Relationships for transverse moduli in terms of apparent density from CT are also shown here for the first time. In addition, this study suggests that transverse apparent modulus varies with subchondral depth, a new finding. This work is the first to show a statistical comparison and quantification of the transverse and axial moduli.

Other examples of analysis of anisotropy in the proximal tibia have utilised micro-FE and fabric methods with results for average anisotropy between 1.3

and 2.8 [41–44], agreeing broadly with those shown here. Concerning fabric based methods in literature, some authors suggest that anisotropy in mechanical properties of bone correlate with micro-CT derived fabric tensor data [45, 46]. The fabric methods from Munford et al. [47] were modified for clinical CT data, however no such correlation between mechanical properties in 3 orthogonal directions and corresponding fabric data was observed here. This difference with literature is likely due to the reduced resolution of fabric data which is available from clinical CT compared to micro computed tomography (μCT).

3.4.3 Considerations

Results for apparent modulus and yield strength observed in this study are in the smaller range of what is seen in literature, however, no values are outside the acceptable range. This may be explained by the strain rate applied during testing being less than physiological loading. The strain rate used is indicative of quasi-static loading and comparable to that used in similar studies.

Testing here was performed on cadaveric specimens, resulting in no bone remodelling and possibly some variation in mechanical properties. The level of mechanical testing and investigation performed here would not currently be possible without cadaveric testing. Similarly, specimens had to be frozen once sliced into cores and thawed before testing, however, the effects of this were mitigated by ensuring that the minimum number of freeze-thaw cycles were used and that all cores from a given specimen were tested in the same testing session.

It is possible that there were some errors in how the cores were cut from the specimens, although these are likely negligible given the errors in core dimensions were $\pm$ 1.7%. The efforts in using specimen specific cutting guides to relate CT scan, CAD and specimen core data appear to have been effective in mitigated any risks concerned with this. Consistency of the observed data from this study and that results from literature suggests that the measures taken to generate specimen specific cutting guides were effective.

Previous studies have suggested that the mechanical properties of bone vary between males and females [48, 49]. Although no such relationship was found in this study, it is noted that the effect of gender on the Z apparent modulus resulting from the ANOVA shown in Table 3.4 may be underpowered (p = 0.055) as the number of male donors was low compared to female donors. Post hoc power analysis was performed on the full factorial model to determine the difference between mean modulus of bone cores from female and male donors and showed a statistical power of 62%. This indicates that the study was indeed under-powered with regards to donor sex.

Previous literature suggests that apparent modulus and strength of bone correlate with fabric tensor data for the micro-structure [50], however no correlation between

mechanical properties in the 3 orthogonal directions and corresponding fabric data was observed. In literature these correlations have been found from high resolution micro-CT methods, whereas fabric methods, modified from Munford et al. [47], for lower resolution clinical CT were applied here. This reduced resolution of fabric data may explain this difference.

3.4.4 Clinical Significance

Knowledge of the spatial variation of multi-axial properties of bone within the proximal tibia allows for improved prediction of bone mechanical properties and strain. This is a crucial part of the development of implants with apparent modulus matched to their surrounding bone, which will allow for improved bone fixation via control of bone mechanobiology and strain response. Such treatments could be particularly useful for early intervention treatments that are likely to be revised in the patient's lifetime. The nature of the design and use of materials in knee implants means that there is greater potential for optimised porous structures in the tibial component than the femoral component, so enhanced knowledge of the mechanical properties in the proximal tibia is essential.

The analysis shown here demonstrates that apparent modulus varies in ways beyond that which is described by apparent density according to a CT scan. As well as improving on the prediction errors of previous literature, this study quantifies for the first time the average effect of the anatomical location of bone within the tibia. The quantification and prediction of mechanical anisotropy of bone in the proximal tibia provides a base for improved FE modelling and implant design.

3.4.5 Conclusion

Trabecular bone mechanical properties in the proximal tibia have been quantified in 3 anatomically relevant directions. The most important finding was that trabecular bone apparent modulus is orthotropic and depends on location within the bone. Yield strength is similarly orthotropic but does not depend on anatomical location. It can be concluded that all models, both in the work studied here and literature, for mechanical properties which have been discussed here provide good predictions and that the some of the variability between these models can be described by factors other than apparent density. This suggests that apparent density alone is not a suitable predictor of apparent modulus in the proximal tibia. Furthermore, accurate prediction of bone mechanical properties within locations in the proximal tibia, as well as quantification of variation between load direction

and other factors, is possible based on this research and will aid the design of implants which are able to control bone's mechanoresponse.

3.5 Bibliography

[1] H. M. Frost, "Bone, mass and the Mechanostat: A proposal," *The Anatomical Record*, vol. 219, pp. 1–9, 9 1987.

[2] R. Huiskes, H. Weinans, and B. van Rietbergen, "The relationship between stress shielding and bone resorption around total hip stems and the effects of flexible materials.," *Clinical orthopaedics and related research*, vol. 274, no. Jan, pp. 124–134, 1992.

[3] C. H. Turner, M. R. Forwood, J. ho, and T. Yoshikawa, "Mechanical loading thresholds for lamellar and woven bone formation," *Journal of Bone and Mineral Research*, vol. 9, no. 1, pp. 87–97, 1994.

[4] T. M. Keaveny, R. E. Borchers, L. J. Gibson, and W. C. Hayes, "Trabecular bone modulus and strength can depend on specimen geometry," *Journal of Biomechanics*, vol. 26, pp. 991–1000, 8 1993.

[5] D. R. Carter and W. C. Hayes, "The compressive behavior of bone as a two-phase porous structure," *Bone & Joint Research America*, vol. 59, pp. 954–962, 1 1977.

[6] K. C. Ng, G. Mantovani, M. Lamontagne, M. R. Labrosse, and P. E. Beaulé, "Cam FAI and Smaller Neck Angles Increase Subchondral Bone Stresses during Squatting: A Finite Element Analysis," in *Clinical Orthopaedics and Related Research*, 2019.

[7] L. J. Gibson and M. F. Ashby, *Cellular solids: Structure and properties, second edition*. 2014.

[8] M. Tuncer, U. N. Hansen, and A. A. Amis, "Prediction of structural failure of tibial bone models under physiological loads: Effect of CT density–modulus relationships," *Medical Engineering & Physics*, vol. 36, pp. 991–997, 8 2014.

[9] L. Peng, J. Bai, X. Zeng, and Y. Zhou, "Comparison of isotropic and orthotropic material property assignments on femoral finite element models under two loading conditions," *Medical Engineering and Physics*, vol. 28, pp. 227–233, 4 2006.

[10] J. H. Keyak, I. Y. Lee, and H. B. Skinner, "Correlations between orthogonal mechanical properties and density of trabecular bone: Use of different densitometric measures," *Journal of Biomedical Materials Research*, vol. 28, pp. 1329–1336, 11 1994.

[11] E. F. Morgan, H. H. Bayraktar, and T. M. Keaveny, “Trabecular bone modulus–density relationships depend on anatomic site,” *Journal of Biomechanics*, vol. 36, pp. 897–904, 7 2003.

[12] J. Rice, S. Cowin, and J. Bowman, “On the dependence of the elasticity and strength of cancellous bone on apparent density,” *Journal of Biomechanics*, vol. 21, pp. 155–168, 1 1988.

[13] C. Yoon, M. J. Chang, C. B. Chang, M. K. Song, J. H. Shin, and S. B. Kang, “Medial Tibial Periprosthetic Bone Resorption and Its Effect on Clinical Outcomes After Total Knee Arthroplasty: Cobalt-Chromium vs Titanium Implants,” *Journal of Arthroplasty*, vol. 33, pp. 2835–2842, 9 2018.

[14] J. T. Deen, T. B. Clay, D. A. Iams, M. B. Horodyski, and H. K. Parvataneni, “Proximal tibial resorption in a modern total knee prosthesis,” *Arthroplasty Today*, vol. 4, pp. 244–248, 6 2018.

[15] V. Majstorovic, M. Trajanovic, N. Vitkovic, and M. Stojkovic, “Reverse engineering of human bones by using method of anatomical features,” *CIRP Annals*, vol. 62, pp. 167–170, 1 2013.

[16] S. Zhao, M. Arnold, S. Ma, R. L. Abel, J. P. Cobb, U. Hansen, and O. Boughton, “Standardizing compression testing for measuring the stiffness of human bone,” *Bone & Joint Research*, vol. 7, no. 8, pp. 524–538, 2018.

[17] K.-C. G. Ng, “The Effects of Cam Femoroacetabular Impingement on Mechanical Hip Joint Loading,” tech. rep., 2017.

[18] K. C. Ng, G. Mantovani, M. Lamontagne, M. R. Labrosse, and P. E. Beaulé, “Increased Hip Stresses Resulting From a Cam Deformity and Decreased Femoral Neck-Shaft Angle During Level Walking,” *Clinical Orthopaedics and Related Research*, 2017.

[19] J. H. Keyak, I. Y. Lee, and H. B. Skinner, “Correlations between orthogonal mechanical properties and density of trabecular bone: Use of different densitometric measures,” *Journal of Biomedical Materials Research*, vol. 28, pp. 1329–1336, 11 1994.

[20] B. Helgason, E. Perilli, E. Schileo, F. Taddei, S. Brynjólfsson, and M. Viceconti, “Mathematical relationships between bone density and mechanical properties: A literature review,” *Clinical Biomechanics*, vol. 23, pp. 135–146, 2 2008.

[21] The MathWorks Inc., “MATLAB,” 2018.

[22] N. Akkas, Y. N. Yeni, B. Turan, E. Delilbasi, and U. Gunel, “Effect of medication on biomechanical properties of rabbit bones: Heparin induced osteoporosis,” *Clinical Rheumatology*, vol. 16, no. 6, pp. 585–595, 1997.

[23] V. D. Sherk and C. J. Rosen, “Senescent and apoptotic osteocytes and aging: Exercise to the rescue?,” *Bone*, vol. 121, pp. 255–258, 4 2019.

[24] S. A. Goldstein, D. L. Wilson, D. A. Sonstegard, and L. S. Matthews, “The mechanical properties of human tibial trabecular bone as a function of metaphyseal location,” *Journal of Biomechanics*, vol. 16, pp. 965–969, 1 1983.

[25] D. S. Elliott, K. J. H. Newman, D. P. Forward, D. M. Hahn, B. Ollivere, K. Kojima, R. Handley, N. D. Rossiter, J. J. Wixted, R. M. Smith, and C. G. Moran, “A unified theory of bone healing and nonunion BHN THEORY,”

[26] J. Wolff, “Concept of the Law of Bone Remodelling,” in *The Law of Bone Remodelling*, Berlin, Heidelberg: Springer Berlin Heidelberg, 1986.

[27] I. Hvid and J. Jensen, “Cancellous bone strength at the proximal human tibia,” *The Orthopaedic Hospital, Arhus, Denmark*, vol. 13, no. 1, pp. 21–25, 1984.

[28] F. J. Klever, R. Klumpert, J. Horenberg, H. J. Grootenboer, D. H. Van Campen, and T. Pauly, “Global Mechanical Properties of Trabecular Bone: Experimental Determination and Prediction from a Structural Model,” in *Biomechanics: Current Interdisciplinary Research*, pp. 167–172, Springer Netherlands, 1985.

[29] R. B. Ashman, J. Y. Rho, and C. H. Turner, “Anatomical variation of orthotropic elastic moduli of the proximal human tibia,” *Journal of Biomechanics*, vol. 22, no. 8-9, pp. 895–900, 1989.

[30] A. Odgaard, I. Hvid, and F. Linde, “Compressive axial strain distributions in cancellous bone specimens,” *Journal of Biomechanics*, vol. 22, pp. 829–835, 1 1989.

[31] O. Lindahl, “To cite this article: Olov Lindahl (1976) Mechanical Properties of Dried Defatted Spongy Bone,” *Acta Orthopaedica Scandinavica*, vol. 47, no. 1, pp. 11–19, 2009.

[32] A. Garg and P. S. Walker, “The effect of the interface on the bone stresses beneath tibial components,” *Journal of Biomechanics*, vol. 19, pp. 957–967, 1 1986.

[33] I. Hvid and S. L. Hansen, “Trabecular bone strength patterns at the proximal tibial epiphysis,” *Journal of Orthopaedic Research*, vol. 3, pp. 464–472, 1 1985.

[34] A. Odgaard and F. Linde, “The underestimation of Young’s modulus in compressive testing of cancellous bone specimens,” *Journal of Biomechanics*, vol. 24, pp. 691–698, 1 1991.

[35] J. D. Johnston, S. A. Kontulainen, B. A. Masri, and D. R. Wilson, "Predicting subchondral bone stiffness using a depth-specific CT topographic mapping technique in normal and osteoarthritic proximal tibiae," *Clinical Biomechanics*, vol. 26, pp. 1012–1018, 12 2011.

[36] S. M. Nazemi, M. Amini, S. A. Kontulainen, J. S. Milner, D. W. Holdsworth, B. A. Masri, D. R. Wilson, and J. D. Johnston, "Optimizing finite element predictions of local subchondral bone structural stiffness using neural network-derived density-modulus relationships for proximal tibial subchondral cortical and trabecular bone," *Clinical Biomechanics*, vol. 41, pp. 1–8, 1 2017.

[37] J. L. Williams and J. L. Lewis, "Properties and an anisotropic model of cancellous bone from the proximal tibial epiphysis," *Journal of Biomechanical Engineering*, vol. 104, pp. 50–56, 2 1982.

[38] F. Linde, B. Pongsoipetch, L. H. Frich, and I. Hvid, "Three-axial strain controlled testing applied to bone specimens from the proximal tibial epiphysis," *Journal of Biomechanics*, vol. 23, pp. 1167–1172, 1 1990.

[39] M. J. Ciarelli, S. A. Goldstein, J. L. Kuhn, D. D. Cody, and M. B. Brown, "Evaluation of orthogonal mechanical properties and density of human trabecular bone from the major metaphyseal regions with materials testing and computed tomography," *Journal of Orthopaedic Research*, vol. 9, no. 5, pp. 674–682, 1991.

[40] L. Rincón-Kohli, P. K. Zysset, L. Rincón-Kohli, and P. K. Zysset, "Multi-axial mechanical properties of human trabecular bone," *Biomech Model Mechanobiol*, vol. 8, pp. 195–208, 2009.

[41] H. A. Gray, F. Taddei, A. B. Zavatsky, L. Cristofolini, and H. S. Gill, "Experimental validation of a finite element model of a human cadaveric tibia," *Journal of Biomechanical Engineering*, vol. 130, p. 031016, 6 2008.

[42] A. Odgaard, J. Kabel, B. Van Rietbergen, M. Dalstra, and R. Huiskes, "Fabric and elastic principal directions of cancellous bone are closely related," *Journal of Biomechanics*, 1997.

[43] W. J. Whitehouse, "The quantitative morphology of anisotropic trabecular bone," *Journal of Microscopy*, vol. 101, pp. 153–168, 7 1974.

[44] T. P. Harrigan, M. Jasty, R. W. Mann, and W. H. Harris, "Limitations of the continuum assumption in cancellous bone," *Journal of Biomechanics*, vol. 21, no. 4, pp. 269–275, 1988.

[45] G. Maquer, S. N. Musy, J. Wandel, T. Gross, and P. K. Zysset, “Bone volume fraction and fabric anisotropy are better determinants of trabecular bone stiffness than other morphological variables,” *Journal of Bone and Mineral Research*, vol. 30, no. 6, pp. 1000–1008, 2015.

[46] P. K. Zysset, “A review of morphology-elasticity relationships in human trabecular bone: theories and experiments,” *Journal of Biomechanics*, vol. 36, pp. 1469–1485, 2003.

[47] M. J. Munford, K. C. G. Ng, and J. R. T. Jeffers, “Mapping the Multi-Directional Mechanical Properties of Bone in the Proximal Tibia,” *Advanced Functional Materials*, vol. 30, p. 2004323, 2020.

[48] M. J. Mirzaali, J. J. Schwiedrzik, S. Thaiwichai, J. P. Best, J. Michler, P. K. Zysset, and U. Wolfram, “Mechanical properties of cortical bone and their relationships with age, gender, composition and microindentation properties in the elderly,” *Bone*, vol. 93, pp. 196–211, 12 2016.

[49] P. J. Kelly, L. Twomey, P. N. Sambrook, and D. J. A. Eisman, “Sex differences in peak adult bone mineral density,” *American Society for Bone and Mineral Research*, vol. 5, no. 11, pp. 1169–1175, 1990.

[50] S. M. Nazemi, M. Amini, S. A. Kontulainen, J. S. Milner, D. W. Holdsworth, B. A. Masri, D. R. Wilson, and J. D. Johnston, “Prediction of local proximal tibial subchondral bone structural stiffness using subject-specific finite element modeling: Effect of selected density–modulus relationship,” *Clinical Biomechanics*, vol. 30, pp. 703–712, 8 2015.

4 Predicting Anisotropy in Porous Materials

Abstract

Additive manufacturing (AM) methods present opportunities for structures to have tailored mechanical anisotropy by integrating controlled lattice structures into their design. The ability to predict anisotropic mechanical properties of such lattice structures would help tailor anisotropy and ensure adequate off-axis strength at an early stage in the design process. A method is described for the development of a model to predict apparent modulus and strength based on structure density and fabric, taken from Computer-aided design (CAD) data. The model utilises a tensorial form of well-founded power-law relationships for these variables and is fit to mechanical test data for properties in the principal directions of manufactured titanium stochastic lattices and nylon rhombic dodecahedron structures. The results are validated against mechanical testing across at least 7 additional off-axis directions. For stochastic structures, apparent modulus is predicted in 10 directions with a mean error of 13% and strength predicted with a mean error of 10%. For rhombic dodecahedron structures apparent modulus and strength are predicted in 15 directions with mean errors of 4.2% and 5.1% respectively. This model is the first to predict the anisotropic apparent modulus and strength of structures based on lattice density and fabric tensors and will be highly useful in the mechanical design of lattice structures.

Credited authors include M.J. Munford, U. Hossain, S. Ghouse, J.R.T. Jeffers [1]

[1]This chapter has been published in the Journal of Additive Manufacturing, 2020. I have presented the related content at the Orthopaedic Research Society Annual Meeting, 2020, February, Phoenix, Arizona.

4.1 Introduction

Development of AM methods has enabled fine control of lattice properties when producing porous lattice structures [1–3]. In this way the internal architecture of an AM component can be assessed and optimised for specific mechanical performance, such as custom modulus and strength properties, porosity and novel surface features [4–6]. The use of lattice structures has been widely expanded across industries such as orthopaedics, aeronautics and defence due to the efficiency of mass distribution in the structure [7–10].

Orthopaedic implants are traditionally manufactured from materials with bulk modulus significantly greater than that of bone, thus changing the load transfer in bone from the physiological norm [11]. AM lattice structures are a viable route to achieve implants which match the mechanical properties of bone and thus maintain physiological load transfer [12, 13]. In aerospace applications, lattice structures manufactured from carbon-fibre-reinforced plastics have been commonly used for interstage structures in launch vessels due to high axial compressive strength-to-weight ratio [9]. Military unmanned aerial vehicles have been developed utilising optimised lattice structures so that components can have optimal elastic modulus and natural frequencies [10, 14]. In all cases, components would benefit from either being isotropic or having designed mechanical anisotropy, potentially dissimilar to their repeating unit cell. AM enables such components, but understanding the anisotropy is a new requirement in the design stage of lattice structures.

Examples of methods for controlling lattice properties include optimising lattice porosity for minimum bone resorption and interface failure [15, 16]. Graded lattices for bone scaffold applications have been created using various initial unit cells, with elastic moduli comparable to bone when tested in one direction [17]. However, the repeating unit cell design of these lattices means they have an intrinsic anisotropy [3]. The apparent modulus of a cubic lattice structure can vary by a factor of over 5 depending on the orientation [3, 18], whilst the apparent modulus of other unit cells can vary by over 6 times at different orientations [19]. This is not ideal because such lattices are often used as ‘space-filling’ geometry within a component and thus create hidden axes of high stiffness. Theoretical unit cells have addressed this issue, however these models do not account for AM printing limitations and are absent of multi-direction mechanical confirmatory testing [20]. An alternative repeating structure based on a tetradecahedral unit cell has demonstrated isotropic behaviour in both theoretical models and mechanical testing, but the surface structure may not be suitable for a bone ingrowth orthopaedic application [21].

A lot of these problems are overcome by pseudo-random, or stochastic, lattice architectures which do not have hidden peaks of high stiffness at certain

orientations. Little data exists on the observed or predicted mechanical anisotropy of such structures when printed using powder bed fusion (PBF), however the methods to predict this exist. Predictions of bone mechanical properties based on isotropic power laws between apparent modulus and density are well founded [22]. Some more recent literature on this topic has sought to incorporate the concept of fabric into such models [23–25]. Fabric is a statistical measure of material directionality and helps to model a lattice or trabecular structured material as a bulk material with directional bias in properties [26]. Fabric based methods have not yet been applied to the analysis of PBF printed lattice structures.

The aim of the paper is to develop a method for predicting the anisotropy in mechanical properties of a stochastic lattice structure, based on CAD data. The model predicts anisotropic apparent modulus and strength in terms of density (ρ), fabric (M) and fabric eigen values (m), inspired by previous methods of measuring bone anisotropy [27]. This method would be highly useful to predict the apparent modulus and anisotropy of lattice structures in order to tailor anisotropy and ensure adequate off-axis strength at an early stage in the design process.

4.2 Material and Methods

4.2.1 Specimen Design and Manufacture

Two lattice structures were investigated, one stochastic and one repeating cell rhombic dodecahedron. Specimens for each lattice type were designed and manufactured as follows.

Stochastic Structure

The stochastic structure was created by populating a volume with pseudo-random points using a Poisson disk algorithm, maintaining a specific minimum proximity. These points were then joined with lines to achieve a certain connectivity. This method, which uses Rhinoceros 5.0 and Grasshopper (Robert McNeel and Associates) is described by Ghouse et. al. [28]. The density of the structure was 4.06 struts/mm^3 and with an average connectivity at each node of 5.80. Lines at an angle of less than 30° inclination to the x-y plane were culled to allow for AM manufacturing.

Solid STL geometry is usually printed using a single exposure printing strategy [28]. For this small scale line geometry, this method was used to melt the required cross section of each strut, also described by Ghouse et. al. [28]. Slice data (build files) were generated at 50 μm layer thickness using Material Engine (Betatype Ltd).

All specimens were printed using a Renishaw AM250 PBF AM system (Renishaw, Wooton Under Edge, UK). Titanium (ELI) spherical powder of particle size range

10–45 μm was used, supplied by LPW Technology (Widnes, UK). The build chamber was vacuumed to -960 mbar and then back filled with 99.995% pure Argon to 10 mbar with an O content of 0.1%. Laser power was constant at 50W whilst exposure times varied from 600 to 1700 μs to maintain a constant strut thickness.

Specimens were removed from the buildplate by electro-discharge machining, ensuring that the wire path preserved the intended part geometry, then cleaned using ultrasonic bath and air jet. Each specimen was individually measured thrice in each dimension using Vernier callipers, and dry weighed thrice at normal atmospheric conditions. The relative density was then calculated by dividing the specimen weight by the bulk weight of the metal that corresponds to the specimen macro volume, assuming a density of 4.43 g/cm^3 for Ti6Al4V.

Rhombic Dodecahedron Structure

The rhombic dodecahedron structure was created using a lattice plugin for Rhinoceros 5.0 and Grasshopper. No lines were culled in this design. The rhombic dodecahedron specimens were 3D printed in medical grade Nylon (PA 2200) using an EOS P110 (EOS, Warwick, UK). Nylon was used as it is a viable material to manufacture low modulus implants which maintain native homeostasis in bone and invoke positive remodelling strains [29]. Using Nylon alongside titanium alloy in this study also helped to explore whether the fabric based methods used here were suitable for a range of modulus values and structures.

Structure Orientation

For both the stochastic and rhombic dodecahedron structures, cuboid compression specimens were generated containing the structure aligned in different directions to the testing axis, as per the spherical coordinates in Tables 4.1a and 4.1b. This allows testing of modulus/strength in multiple axes. Figure 4.1 illustrates how the spherical coordinates were used to determine specimen orientation and print direction. For the stochastic specimens, five specimens were tested per direction, with dimensions 10 x 10 x 12mm and for the rhombic dodecahedron cell specimens, two specimens were tested per direction with dimensions 15 x 15 x 20.5mm. All specimens conformed to ISO 13314:2011 [30].

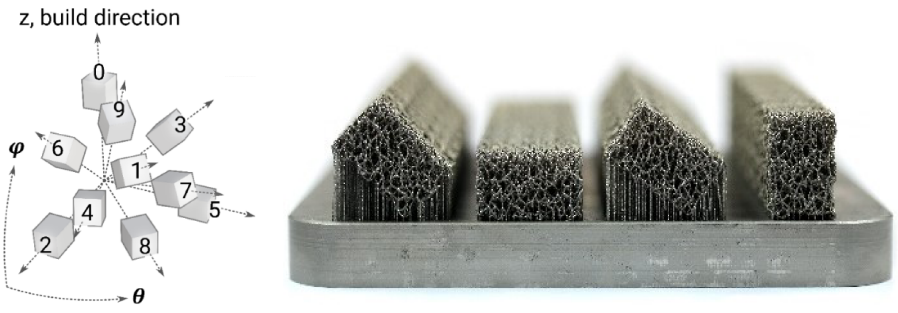
Table 4.1: Spherical coordinates of structure test directions. Definitions given for (4.1a) stochastic specimens and (4.1b) rhombic dodecahedron specimens.

(a)

Direction	θ	ϕ
0	0	90
1	45	35
2	0	0
3	90	45
4	20	19
5	90	0
6	0	45
7	70	19
8	45	0
9	45	63

(b)

Direction	θ	ϕ
0	0	0
1	30	0
2	45	0
3	60	0
4	30	30
5	30	45
6	30	60
7	45	30
8	45	45
9	45	60
10	60	30
11	60	45
12	60	60
13	90	0
14	0	90



(a) **(b)**

Figure 4.1: Manufacture of titanium stochastic structures for testing directional properties. (4.1a) Stochastic specimen orientations for all 10 test directions based on spherical coordinates in Table 4.1 and (4.1b) the corresponding printed specimens.

4.2.2 Calculation of Fabric Tensors and Fitting of Predictive Model

Directional data of the generated structure was extracted from the CAD model and used to determine a fabric moment tensor from a list of direction vectors based

on mean intercept length (MIL) methods as follows [31]:

A list of the vectors describing all of the struts in the CAD line file in Figure 4.2a were exported from Rhino 6 into MATLAB. The distribution of vectors shown in Figure 4.2b illustrates how all struts below $30^{/circ}$ inclination to the x-y plane have been removed. The fabric moment tensor ellipsoid representation in Figure 4.2c has the expected characteristic hourglass shape of an orthotropic structure. The fabric tensor is a second order symmetric tensor with eigen values $(\lambda_1, \lambda_2, \lambda_3)$ and eigen vectors $(\lambda_1, \lambda_2, \lambda_3)$ which describe the magnitude and direction of the structure principal directions indicated in Figure 4.2c.

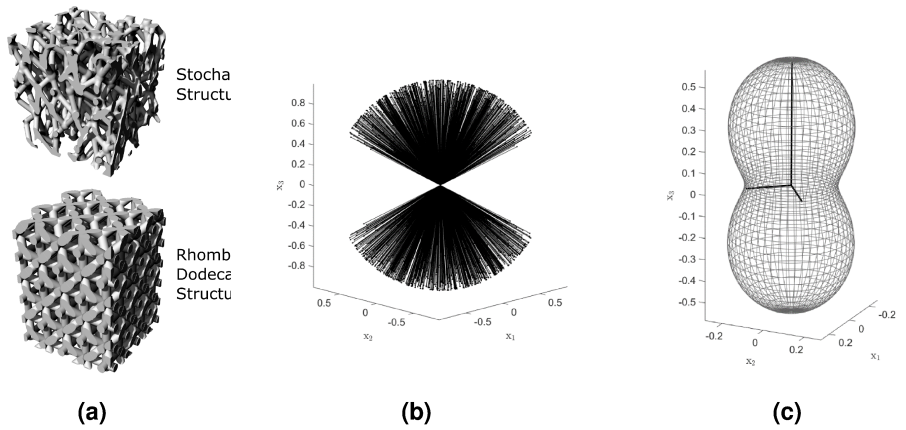


Figure 4.2: Summary of data extracted from CAD strut vectors. (4.2a) CAD line structure file for the stochastic and rhombic dodecahedron structures built as in Section. (4.2b) Directional data for the 2155 line vectors comprising the stochastic structure in 4.2a. (4.2c) Ellipsoid representation (grey) and weighted principal directions for the fabric moment tensor for the stochastic structure in 4.2a.

This process was repeated for the rhombic dodecahedron structure to yield a different symmetric second order fabric tensor to describe the distribution of material orientation in the rhombic dodecahedron lattice.

The predictive model for lattice apparent modulus was based on a tensorial form of Cowin's fabric-elasticity equations, similar to that described by Zysset-Curnier [24]. This model allowed conversion from lattice density and fabric data to orthotropic elastic properties. This model builds upon the commonly used density-modulus power law relationship stated by Gibson and Ashby [32] $(\lambda\rho^k)$ by introducing power terms which include the eigenvalues (m(i)). The use of a different power term for each fabric eigenvalue (l(i)) differentiates this model from similar models in literature.

$$\mathbf{S} = \Sigma_{i,j=1}^{i,j=3} \lambda(i,j) \rho^k m(i)^{l(i)} m(j)^{l(j)} |\boldsymbol{M_i} \otimes \boldsymbol{M_j}|^2 \tag{4.1}$$

Multivariate linear regression was performed to fit the data for density and fabric eigenvalues to the experimentally measured apparent modulus in the three orthogonal principal directions only (described in Section 4.2.1), to form the theoretical model described by Equation 4.1 (see Table 4.2). This was repeated to fit the density and fabric eigenvalues to the strength data. In this manner, orthotropic compliance and stress tensors were formed from the observed apparent modulus and strength along principal directions (Table 4.2). To generate the parameters defining the model for apparent modulus, components of the orthotropic tensor were aligned in a vector y. A log transformation was applied to the density, fabric eigenvalues, mechanical property values and regression coefficients to obtain a multiple linear regression model of the form y = Xc + e, whereby X is a 10 x n matrix containing the density and fabric information for the model, c is a vector containing the constants which define Equation 1 and e is the vector of the residuals. A complete form of this equation is given in Appendix A.2. This system of equations was then solved for the 10 model parameters contained in the vector c as per Equation 4.2.

$$\mathbf{c} = [ln(\lambda_{1,1}) \quad ln(\lambda_{2,2}) \quad ln(\lambda_{3,3}) \quad ln(\lambda_{1,2}) \quad ln(\lambda_{1,3}) \quad ln(\lambda_{2,3}) \quad \rho \quad l_1 \quad l_2 \quad l_3]' \tag{4.2}$$

This process was repeated with the elements of vector y replaced by components of the orthotropic stress tensor to determine coefficients for the strength model. The variables in c define Equation 4.1 to yield anisotropic tensors for apparent modulus and strength in terms of the known density, ρ, fabric eigenvalues m_i and fabric eigenvector dyadic M_i. The fabric dyadics are defined by Equation 4.3.

$$\mathbf{M_i} = \lambda_\mathbf{i} \otimes \lambda_\mathbf{i} \tag{4.3}$$

The apparent density could not be accurately recorded for the nylon specimens due to the presence of semi-sintered and loose powder from the manufacturing process. The density term (ρ) in Equation 1 was therefore neglected and k set to 0 so that the models for predicting apparent modulus and strength of nylon lattice structures were based on fabric from CAD data and not density.

4.2.3 Mechanical Measurement of Anisotropic Properties

A materials testing machine (Instron 8872) with a 10kN load cell was used to perform quasi-static compression testing at an extension rate of 2 mm/min, which corresponds to a strain rate within standard limits.

Displacement was measured using LVDTs to reduce any compliance effects from the test apparatus. A sampling rate of 30Hz was used. The platens of the machine were lubricated to reduce any frictional effects. Stress-strain curves were obtained using the individual macro dimensions of each specimen.

The loading regime includes a hysteresis loop to account for localised yielding within the porous structure. This was carried out from 70% of the yield stress (σ_{70}), to 20% of the yield stress (σ_{20}) and then the specimen is fully compressed to a high strain [33]. The elastic moduli were then calculated using a linear regression analysis of the hysteresis loop. A preliminary specimen was compressed to 50% strain at 2mm/min to find the required reference stresses. Figure 4.3 illustrates how the apparent modulus, yield and peak strength were determined for the Titanium stochastic structures, where yield stress was taken as the plateau stress from 20 to 30% strain. Testing of preliminary specimens suggested that the peak and yield stress were almost identical for these specimens, peak stress was therefore measured as an indicator of lattice strength. For the nylon rhombic dodecahedron specimens, the 1% offset stress was used as an indicator of strength.

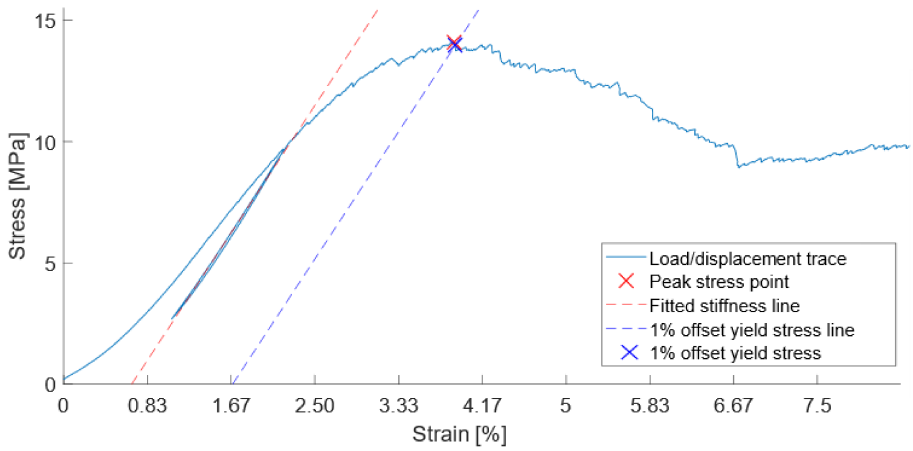


Figure 4.3: Typical load-displacement curve for a stochastic titanium structure. Mechanical properties determined as apparent modulus = 0.66 GPa, peak stress = 14 7 MPa and 1% offset yield stress = 14.51 MPa

For each structure type, all structures were generated from the same lattice CAD file so therefore had the same fabric tensor, as indicated in Table 4.2. Eigenvalue decomposition for the titanium stochastic structures yields the equivalent Eigenvalues (λ) and Eigenvectors (λ) for this tensor as:

Table 4.2: Summary of specimen build direction, density, fabric and mechanically tested apparent modulus and peak strength data. Data given for the orthogonal axes stochastic and rhombic dodecahedron lattice structures.

	Build Dir.	n	Apparent Density [gcm^{-3}]	M	Apparent Modulus [MPa]	Peak Strength [MPa]
Titanium	0	5	698 – 704	$\begin{bmatrix}0.21 & 0.00 & 0.00\\ 0.00 & 0.21 & 0.00\\ 0.00 & 0.00 & 0.58\end{bmatrix}$	2920 – 2980	37.7 – 39.5
	2	5	694 – 700		740 – 790	15.9 – 16.7
	5	5	672 – 685		610 – 670	14.1 – 14.8
Nylon	0	2	Not Applicable	$\begin{bmatrix}0.36 & 0.00 & 0.00\\ 0.00 & 0.36 & 0.00\\ 0.00 & 0.00 & 0.27\end{bmatrix}$	159 - 160	5.47 – 5.51
	14	2			99.6 – 121	3.94 – 4.24
	15	2			99.6 - 121	3.94 – 4.24

$$\begin{bmatrix}\lambda_1\\ \lambda_2\\ \lambda_3\end{bmatrix} = \begin{bmatrix}0.204\\ 0.213\\ 0.583\end{bmatrix} \text{ and } \begin{bmatrix}\boldsymbol{\lambda_1} & \boldsymbol{\lambda_2} & \boldsymbol{\lambda_3}\end{bmatrix} = \begin{bmatrix}0.631 & 0.776 & 0.007\\ -0.776 & 0.631 & 0.010\\ 0.004 & -0.012 & 1.000\end{bmatrix}$$

Similarly, eigenvalue decomposition for the nylon rhombic dodecahedron structures yields the equivalent Eigenvalues (λ) and Eigenvectors (λ) for this tensor as:

$$\begin{bmatrix}\lambda_1\\ \lambda_2\\ \lambda_3\end{bmatrix} = \begin{bmatrix}0.272\\ 0.361\\ 0.367\end{bmatrix} \text{ and } \begin{bmatrix}\boldsymbol{\lambda_1} & \boldsymbol{\lambda_2} & \boldsymbol{\lambda_3}\end{bmatrix} = \begin{bmatrix}0.002 & -0.791 & -0.612\\ 0.007 & 0.612 & -0.791\\ 1 & -0.003 & 0.006\end{bmatrix}$$

4.3 Results

The regression methods described in Section 4.2.2 define the model parameters λ, l and k for prediction of apparent modulus and peak strength for both lattice types as in Table 4.3.

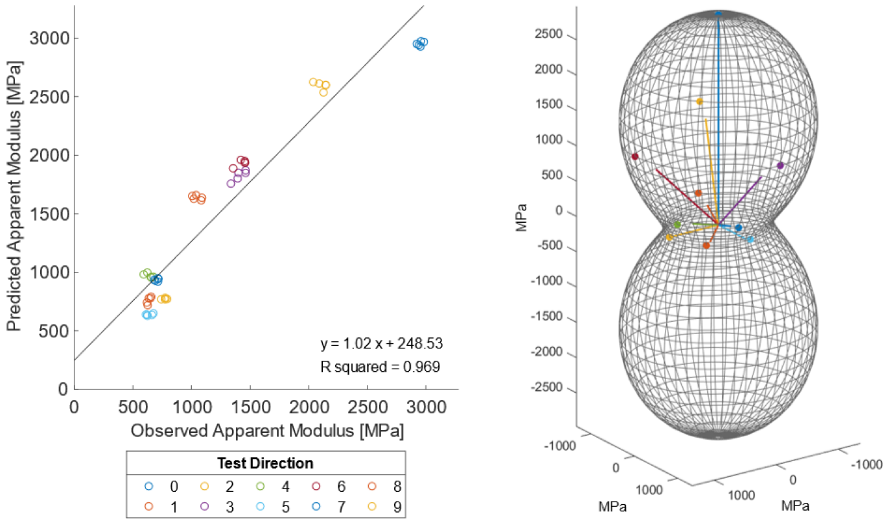
4.3.1 Stochastic Lattice Results

The model for the titanium stochastic lattice predicted the apparent modulus of the structure across all 10 orientations (Figure 4.4a). A linear relationship between the measured and predicted values was found (R^2=0.969, when the relationship

Table 4.3: Parameters defining prediction models for both apparent modulus and strength of the stochastic lattice and the rhombic dodecahedron lattice. Parameters refer to Equation 4.2.

Lattice	Parameter	λ	l	k
Stochastic	Apparent Modulus	$\begin{bmatrix} 1 & 0.10 & 0.42 \\ 0.10 & 1 & 0.51 \\ 0.42 & 0.51 & 1 \end{bmatrix}$	$\begin{bmatrix} 1.3 \\ 1.4 \\ 2.8 \end{bmatrix}$	1.6
	Strength	$\begin{bmatrix} 1 & 0.11 & 1.85 \\ 0.11 & 1 & 2.22 \\ 1.85 & 2.22 & 1 \end{bmatrix}$	$\begin{bmatrix} 2.7 \\ 2.8 \\ 7.4 \end{bmatrix}$	1.7
Rhombic Dodecahedron	Apparent Modulus	$\begin{bmatrix} 1 & 0.06 & 0.08 \\ 0.06 & 1 & 0.12 \\ 0.08 & 0.12 & 1 \end{bmatrix}$	$\begin{bmatrix} 1.8 \\ 2.3 \\ 2.5 \end{bmatrix}$	-
	Strength	$\begin{bmatrix} 1 & 0.07 & 0.08 \\ 0.07 & 1 & 0.11 \\ 0.08 & 0.11 & 1 \end{bmatrix}$	$\begin{bmatrix} 0.5 \\ 0.6 \\ 0.8 \end{bmatrix}$	-

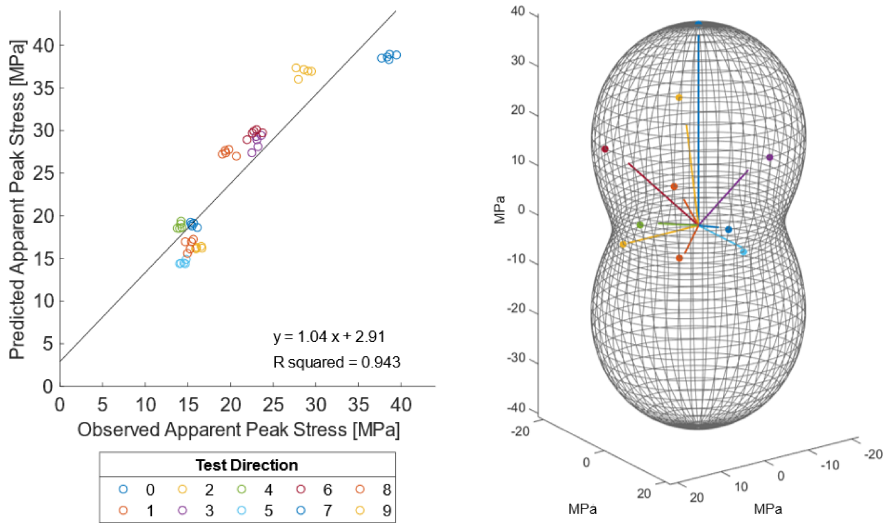
was not forced through the origin), with a 0.2 GPa offset indicating the model slightly over-predicted the apparent modulus of the off-axis directions. When the linear relationship was forced to go through the origin, the correlation coefficient was R^2=0.942. The linear relationship was left floating and not forced through the origin so that any error/systematic offset could be observed. This process was followed for the data shown in Figures 4.4a, 4.5a, 4.7a and 4.8a. The predicted and measured anisotropy both generated the hour-glass shape for three dimensional modulus (Figure 4.4b). The closest prediction was for orthogonal directions 0, 2 and 5 which was expected as the experimental values from these directions were used to define the model. The model overpredicted modulus in directions 1, 3, 6 and 9 by 16 to 23%. In directions 4, 7 and 8 the model over predicted by between 12 and 16%.



(a) (b)

Figure 4.4: Model predictions for titanium stochastic structure anisotropic apparent modulus. 4.4a Predicted apparent modulus against their corresponding observed apparent modulus along each of the 10 tested vector directions for the purely predictive model for titanium stochastic structures. 4.4b Predicted anisotropic apparent modulus ellipsoid (grey), mean observed apparent modulus in each of the 10 directions (coloured lines) and predicted apparent modulus along those 10 directions (coloured dots). Legend applies to both figures and refers to the test directions in Table 4.1a.

The model predicted the peak strength of the structure across all 10 orientations (Figure 4.5a). A linear relationship between the measured and predicted values was found (R^2=0.943, when the relationship was not forced through the origin), with a 2.9 MPa offset indicating the model also slightly overpredicted the peak strength of the off-axis directions. When the linear relationship was forced to go through the origin, the correlation coefficient was R^2=0.912. The predicted and measured anisotropy both generated the hour-glass shape for three dimensional modulus (Figure 4.5b). As with the apparent modulus model, the closest prediction was for orthogonal directions 0, 2 and 5 which was expected as the experimental values from these directions were used to define the model. The model overpredicted strength in directions 1, 3, 6 and 9 by 14 to 18%. In directions 4, 7 and 8 the model over predicted by between 8 and 16%.



(a) (b)

Figure 4.5: Model predictions for titanium stochastic structure anisotropic peak strength. 4.5a Predicted peak strength against the corresponding observed peak strength along each of the 10 tested vector directions for the purely predictive model for titanium stochastic structures. 4.5b Predicted anisotropic strength ellipsoid (grey), mean observed strength in each of the 10 directions (coloured lines) and predicted strength along those 10 directions (coloured dots). Legend applies to both figures and refers to the test directions in 4.1a.

The predictive model provided a close apparent modulus-strength relationship to the measured relationship (Figure 4.6). For a given modulus, the model slightly over predicted the strength, but by less than 8% across the 0.5 – 3 GPa test range. Both predicted and measured relationships had a power relationship with R^2 = 0.99.

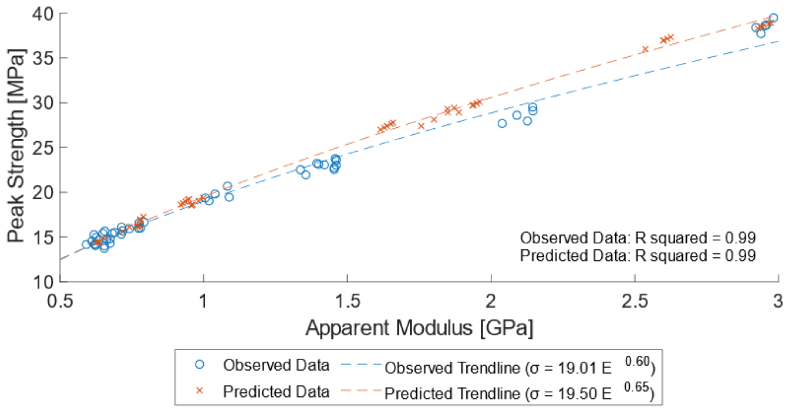
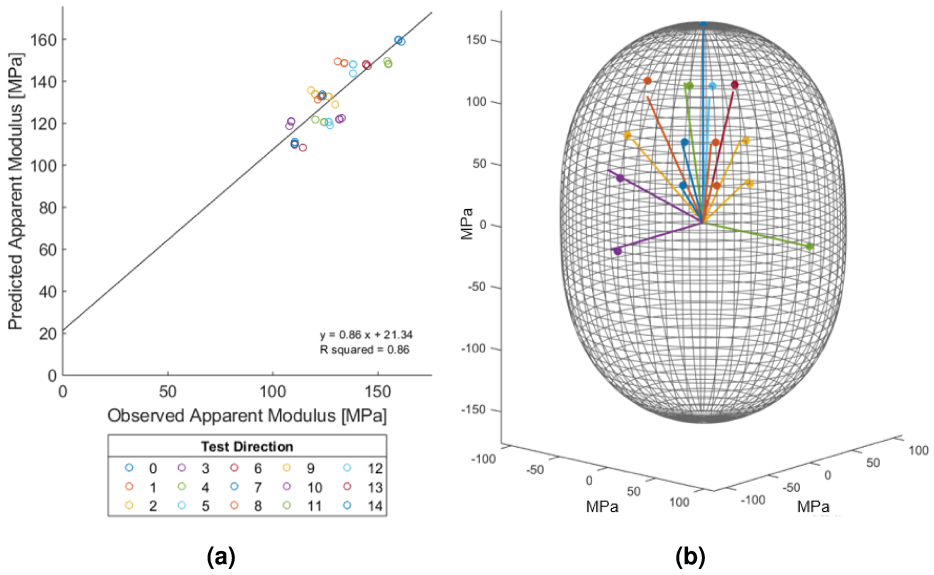


Figure 4.6: Peak strength against apparent modulus for titanium stochastic structures. Comparing observed data with and model predictions.

4.3.2 Rhombic Dodecahedron Lattice Results

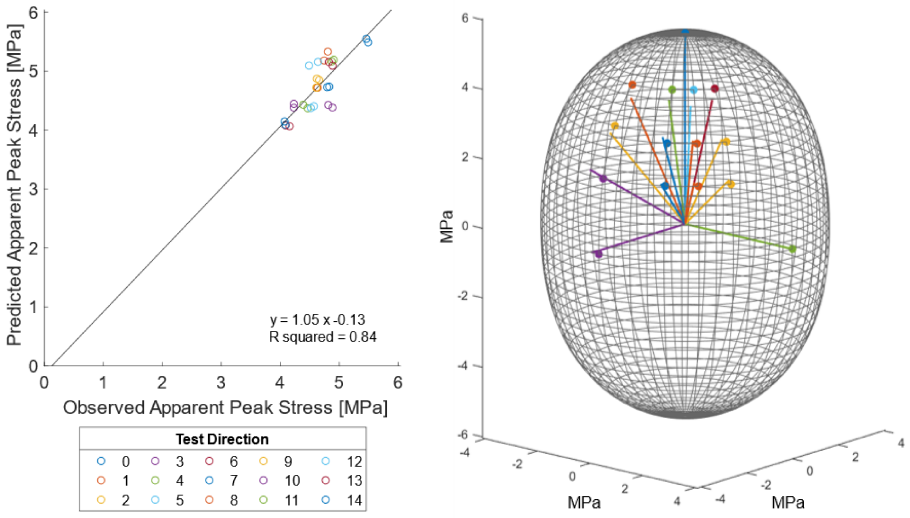
The model for the nylon rhombic dodecahedron lattice predicted the apparent modulus of the structure across all 15 orientations (Figure 4.7). A linear relationship between the measured and predicted values was found (R^2=0.86, when the relationship was not forced through the origin), with a 21.3 MPa offset indicating the model slightly overpredicted the apparent modulus of the off-axis directions. When the linear relationship was forced to go through the origin, the correlation coefficient was R^2=0.85. The predicted and measured anisotropy both generated the ellipsoid for 3 dimensional modulus (Figure 4.7b). The closest prediction was for orthogonal directions 0, 13 and 14 which was expected as the experimental values from these directions were used to define the model. On average, the model underpredicted apparent modulus in directions which were inclined 30 degrees to the horizontal (directions 1, 4, 5 and 6) with a mean absolute error of 7%. For directions 2, 7, 8 and 9 which are inclined at 45 degrees to the horizontal the model consistently underpredicted values to within 8.9%. Across directions 3, 10, 12 and 13, which are 60 degrees to the horizontal, the model predicted apparent modulus values to within 7.6%.



(a) (b)

Figure 4.7: Model predictions for nylon rhombic-dodecahedron structure anisotropic apparent modulus. 4.7a Predicted apparent modulus against the corresponding observed apparent modulus along each of the 10 tested vector directions for the purely predictive model for Nylon rhombic-dodecahedron structures. 4.7b Predicted anisotropic strength ellipsoid (grey), mean observed modulus in each of the 10 directions (coloured lines) and predicted modulus along those 10 directions (coloured dots). Legend applies to both figures and refers to the test directions in Table 4.1b.

The model predicted the strength of the structure across all 15 orientations (Figure 4.8). A linear relationship between the measured and predicted values was found (R^2=0.840, when the relationship was not forced through the origin), with -0.13 MPa offset indicating the model also slightly underpredicted the strength of the off-axis directions. When the linear relationship was forced to go through the origin, the correlation coefficient was R^2=0.82. The predicted and measured anisotropy both generated the ellipsoid shape for 3 dimensional modulus (Figure 4.8b). As with the apparent modulus model, the closest prediction was for orthogonal directions 0, 13 and 14 which was expected as the experimental values from these directions were used to define the model. The model underpredicted peak stress across all directions which were inclined 30 degrees to the horizontal (directions 1, 4, 5 and 6) with a mean absolute error of 8.8%. For directions 2, 7, 8 and 9 which are inclined at 45 degrees to the horizontal the model predicted values to within 5%. Across directions 3, 10, 12 and 13, which are 60 degrees to the horizontal, the model predicted apparent modulus values to within 5.9% absolute error.



(a) (b)

Figure 4.8: Model predictions for nylon rhombic-dodecahedron structure anisotropic peak strength. 4.8a Predicted peak strength against the corresponding observed peak strength along each of the 10 tested vector directions for the purely predictive model. 4.8b Predicted anisotropic strength ellipsoid (grey), mean observed strength in each of the 10 directions (coloured lines) and predicted strength along those 10 directions (coloured dots). Legend applies to both figures and refers to the test directions in Table 4.1b.

The predictive models for nylon rhombic dodecahedron structures provided a close apparent modulus-strength relationship to the measured relationship (Figure 4.9). For a given modulus, the model slightly underpredicted the strength for lower moduli and overpredicted strength for larger moduli values, always within 10.2% across the 0.1 – 0.16 GPa test range. Both predicted and measured relationships had a power relationship with R^2 = 0.99.

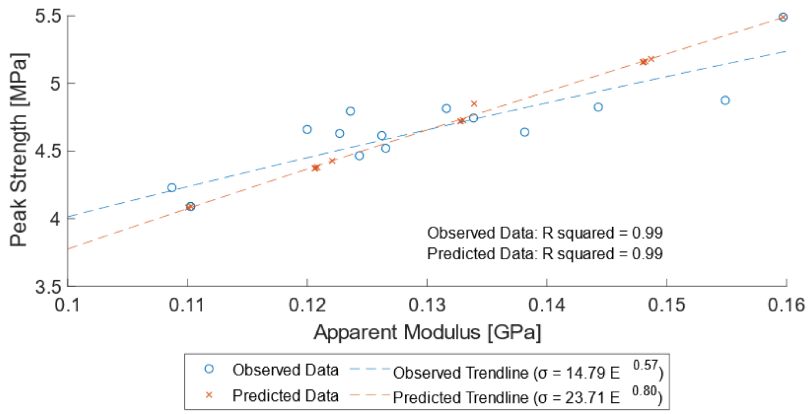


Figure 4.9: Peak strength against apparent modulus for nylon rhombic-dodecahedron specimens. Comparing observed data with and model predictions.

4.4 Discussion

4.4.1 Summary of Results

This study demonstrates that the off-axis apparent modulus and strength of lattice structures can be predicted with good accuracy using fabric/elasticity equations. This is a highly useful tool, enabling the strength and anisotropy of lattices to be determined while the component is at an early stage in the design process. It does not eliminate the need for testing but provides an opportunity for design iteration prior to part manufacture which can reduce development time and costs. Our approach is an alternative to finite element analysis but has the advantage that it doesn't need specialist and expensive software, no complex mesh is required, nor convergence problems are encountered. The stochastic structure used in our study was anisotropic with the highest apparent modulus of 2.9 GPa measured in the build direction and lowest apparent modulus of 0.6 – 0.8 GPa measured perpendicular to the build direction. The anisotropy was caused by the removal of low angle struts relative to the build direction, but it may be possible to generate more isotropic structures, for example by increasing the diameter of the lower angle struts or by decreasing the culling angle. The peak strength of this structure was highest in the build direction (40 MPa) and lowest in the direction perpendicular to the build direction (15-18 MPa).

The rhombic dodecahedron structure proved to be almost isotropic, with apparent modulus ranging from 110 MPa to 160 MPa and strength ranging from 4.1 MPa to 5.5 MPa. As for the stochastic specimens, for both apparent modulus and

Table 4.4: Summary of existing models for apparent modulus prediction in literature Literature models predict apparent modulus and strength along a limited set of axes [34–36].

Author	Lattice Type	Material	Modulus [GPa]	Strength [MPa]
Souza et al.	BCC/FCC	Stainless steel	0.01-14	0.1-110
McGregor et al.	Hexagonal	Polymers	0.004-0.610	0.04-34
Ferrigno et al.	Octet	Ti-6Al-4V	76-111.3	281-955

strength, the highest values were in the build direction and lowest values were perpendicular to the build direction. The nylon rhombic dodecahedron specimens had mechanical anisotropy of 1.5 for apparent modulus and 1.3 for strength.

Incorporation of lattice structures into load bearing components is possible, but consideration must be made for the different strength and failure mechanisms of lattice structures compared to the parent material. The proposed mathematical calculations provide a rapid way to assess strength in all loading axes at an early stage in component design.

4.4.2 Comparison to Literature

Previous methods for the prediction of mechanical properties have been based on either FEA or analytical methods, with all approaches focussing on repeating cells (Table 4.4).

Souza et al reported an apparent modulus of between 0.01 and 14 GPa for steel repeating cell meshes, with a corresponding strength of 0.1 – 110 MPa [34]. Ferringo et al predicted an apparent modulus between 76-111 GPa for Ti-6Al-4V lattices. Both studies used models that overpredicted the apparent modulus and strength, within the same tolerance as the model presented in our paper. They attributed the overestimate to inaccurate modelling of shear properties and geometric imperfections in the printed specimens [34]. Few previous studies have validated models for mechanical properties of AM structures with mechanical testing or accounted for limitations of AM printing, instead studies have employed computational methods for repeating cells, less suitable for stochastic structures, to validate their findings [20, 34, 37]. Although Souza et al provide good data for structures designed with a range of apparent moduli and strengths suitable for use in bone implants, the presence of horizontal and low angle struts relative to the build direction complicate these reliable manufacture of the structures [34]. The results presented by McGregor et al also demonstrate good prediction of properties over a suitable range, with mechanical validation, but the repeating unit hexagonal cell structures means hidden off-axis stiffness peaks will be present

[35]. Ferrigno et al provide another good model for apparent modulus and strength prediction with mechanical validation in one direction, however their range of apparent moduli and strengths lie outside of that required for the application of bone implants [36].

The relationships between predicted apparent modulus and strength across all test directions exhibited a power law trend for both structure types ($\sigma = 19.5E^{0.65}$ for stochastic specimens and $\sigma = 23.71E^{0.8}$ for rhombic dodecahedron specimens), as in Figures 4.6 and 4.9. This relationship is similar for both the predicted and observed data. Furthermore, the presence of a power law between strength and apparent modulus is consistent with findings in literature where models with a range of coefficients and powers can be found [28, 32].

4.4.3 Considerations

Torsional stiffness and strength have been neglected when fitting the described model to the mechanical data. This limits this model to non-torsional analysis only, however, this has no detrimental effect on the results presented here as the orthotropic and torsional apparent modulus elements in the stiffness matrix are uncoupled. This method predicts static apparent modulus and strength whereas fatigue mechanical properties may be more suitable design considerations in some applications, particularly in bone implants [38]. We also tested at a fixed load rate which was less than physiological loading. However, previous studies have found relationships between dynamic and static mechanical properties which suggests that this model would be equally applicable to dynamic data. The method presented here requires an initial set of specimens to be manufactured and mechanically tested in orthogonal directions to determine apparent modulus and strength before any predictions of the mechanical properties of future structures can be tested. This is not necessary in FE methods, which can return structural mechanical data based on only material properties. Although it is time intensive, the use of mechanical data to form the models shown in this study means that the returned model has been validated and gave greater confidence in the model predictions. The effect of anisotropic microstructure of AM components is not accounted for in this model. Build orientation can cause a highly orientated microstructure resulting in inherent mechanical anisotropy in AM components even if the geometry is isotropic.

4.4.4 Clinical Significance

The stochastic structures presented here have the potential to be used as a base lattice in the orthopaedic industry because their properties and anisotropy are similar to those of human bone. Both structures may also be useful for light-weight applications where a space-filling isotropic lattice with specific properties is required for load bearing or impact conditions. The deployment of such lattice structures requires a greater analysis of anisotropy than has historically been necessary for solid isotropic materials. Our method of predicting off axis stiffness and strength based on data from the orthogonal directions is a reliable and rapid way to assess these data and can be performed on CAD models which enables an early opportunity to control mechanical anisotropy.

4.5 Conclusion

Our model is the first to predict the anisotropic apparent modulus and strength of stochastic and rhombic dodecahedron structures based on lattice density and fabric tensors and will be highly useful in the mechanical design of lattice structures.

4.6 Bibliography

[1] S. Tsopanos, R. A. W. Mines, S. McKown, Y. Shen, W. J. Cantwell, W. Brooks, and C. J. Sutcliffe, "The Influence of Processing Parameters on the Mechanical Properties of Selectively Laser Melted Stainless Steel Microlattice Structures," *Journal of Manufacturing Science and Engineering*, 2010.

[2] Cyganik, M. Binkowski, G. Kokot, T. Rusin, P. Popik, F. Bolechała, R. Nowak, Z. Wróbel, and A. John, "Prediction of Youngs modulus of trabeculae in microscale using macro-scales relationships between bone density and mechanical properties," *Journal of the Mechanical Behavior of Biomedical Materials*, vol. 36, pp. 120–134, 8 2014.

[3] V. J. Challis, X. Xu, L. C. Zhang, A. P. Roberts, J. F. Grotowski, and T. B. Sercombe, "High specific strength and stiffness structures produced using selective laser melting," *Materials and Design*, vol. 63, pp. 783–788, 2014.

[4] P. Zhang, J. Toman, Y. Yu, E. Biyikli, M. Kirca, M. Chmielus, and A. C. To, "Efficient Design-Optimization of Variable-Density Hexagonal Cellular

Structure by Additive Manufacturing: Theory and Validation," *Journal of Manufacturing Science and Engineering*, 2015.

[5] S. J. Carrington, C. C. Hernandez, D. R. Swale, O. A. Aluko, J. S. Denton, and R. D. Cone, "G protein–coupled receptors differentially regulate glycosylation and activity of the inwardly rectifying potassium channel Kir7.1," *Journal of Biological Chemistry*, vol. 293, pp. 17739–17753, 11 2018.

[6] J. Martínez, J. Dumas, and S. Lefebvre, "Procedural voronoi foams for additive manufacturing," *ACM Transactions on Graphics*, 2016.

[7] X. Wang, S. Xu, S. Zhou, W. Xu, M. Leary, P. Choong, M. Qian, M. Brandt, and Y. M. Xie, "Topological design and additive manufacturing of porous metals for bone scaffolds and orthopaedic implants: A review," *Biomaterials*, vol. 83, pp. 127–141, 3 2016.

[8] V. Petrovic, J. Vicente, J. Ramn, and L. Portols, "Additive Manufacturing Solutions for Improved Medical Implants," in *Biomedicine*, 2012.

[9] A. Hou and K. Gramoll, "Design and Fabrication of CFRP Interstage Attach Fitting for Launch Vehicles," *Journal of Aerospace Engineering*, vol. 12, pp. 83–91, 7 1999.

[10] S. K. Moon, Y. E. Tan, J. Hwang, and Y. J. Yoon, "Application of 3D printing technology for designing light-weight unmanned aerial vehicle wing structures," *International Journal of Precision Engineering and Manufacturing - Green Technology*, 2014.

[11] D. S. Elliott, K. J. H. Newman, D. P. Forward, D. M. Hahn, B. Ollivere, K. Kojima, R. Handley, N. D. Rossiter, J. J. Wixted, R. M. Smith, and C. G. Moran, "A unified theory of bone healing and nonunion BHN THEORY,"

[12] A. L. Jardini, M. A. Larosa, C. A. de Carvalho Zavaglia, L. F. Bernardes, C. S. Lambert, P. Kharmandayan, D. Calderoni, and R. Maciel Filho, "Customised titanium implant fabricated in additive manufacturing for craniomaxillofacial surgery: This paper discusses the design and fabrication of a metallic implant for the reconstruction of a large cranial defect," *Virtual and Physical Prototyping*, 2014.

[13] K. C. Wong, S. M. Kumta, K. H. Chiu, K. W. Cheung, K. S. Leung, P. Unwin, and M. C. Wong, "Computer assisted pelvic tumor resection and reconstruction with a custom-made prosthesis using an innovative adaptation and its validation," *Computer Aided Surgery*, 2007.

[14] C. Imediegwu, R. Murphy, R. Hewson, and M. Santer, "Multiscale structural optimization towards three-dimensional printable structures," *Structural and Multidisciplinary Optimization*, pp. 1–13, 2019.

[15] W. Li, J. Chen, C. Rungsiyakull, M. V. Swain, and Q. Li, “Multiscale Remodelling and Topographical Optimisation for Porous Implant Surface Morphology Design,” 2016.

[16] S. Arabnejad Khanoki and D. Pasini, “Multiscale Design and Multiobjective Optimization of Orthopedic Hip Implants with Functionally Graded Cellular Material,” *Journal of Biomechanical Engineering*, 2012.

[17] M. Dumas, P. Terriault, and V. Brailovski, “Modelling and characterization of a porosity graded lattice structure for additively manufactured biomaterials,” *Materials and Design*, 2017.

[18] E. Sallica-Leva, A. L. Jardini, and J. B. Fogagnolo, “Microstructure and mechanical behavior of porous Ti-6Al-4V parts obtained by selective laser melting,” *Journal of the Mechanical Behavior of Biomedical Materials*, vol. 26, pp. 98–108, 2013.

[19] V. Weißmann, R. Bader, H. Hansmann, and N. Laufer, “Influence of the structural orientation on the mechanical properties of selective laser melted Ti6Al4V open-porous scaffolds,” *Materials and Design*, vol. 95, pp. 188–197, 4 2016.

[20] S. Xu, J. Shen, S. Zhou, X. Huang, and Y. M. Xie, “Design of lattice structures with controlled anisotropy,” *Materials & Design*, vol. 93, pp. 443–447, 3 2016.

[21] A. Takezawa, K. Yonekura, Y. Koizumi, X. Zhang, and M. Kitamura, “Isotropic Ti–6Al–4V lattice via topology optimization and electron-beam melting,” *Additive Manufacturing*, vol. 22, pp. 634–642, 8 2018.

[22] M. Tuncer, U. N. Hansen, and A. A. Amis, “Prediction of structural failure of tibial bone models under physiological loads: Effect of CT density–modulus relationships,” *Medical Engineering & Physics*, vol. 36, pp. 991–997, 8 2014.

[23] S. M. Nazemi, M. Amini, S. A. Kontulainen, J. S. Milner, D. W. Holdsworth, B. A. Masri, D. R. Wilson, and J. D. Johnston, “Prediction of local proximal tibial subchondral bone structural stiffness using subject-specific finite element modeling: Effect of selected density–modulus relationship,” *Clinical Biomechanics*, vol. 30, pp. 703–712, 8 2015.

[24] P. K. Zysset, “A review of morphology-elasticity relationships in human trabecular bone: theories and experiments,” *Journal of Biomechanics*, vol. 36, pp. 1469–1485, 2003.

[25] J. Hazrati Marangalou, K. Ito, M. Cataldi, F. Taddei, and B. van Rietbergen, “A novel approach to estimate trabecular bone anisotropy using a database approach,” *Journal of Biomechanics*, vol. 46, pp. 2356–2362, 9 2013.

[26] S. C. Cowin, “The relationship between the elasticity tensor and the fabric tensor,” *Mechanics of Materials*, vol. 4, pp. 137–147, 7 1985.

[27] P. K. Zysset, R. W. Goulet, and S. J. Hollister, “A Global Relationship Between Trabecular Bone Morphology and Homogenized Elastic Properties,” *Journal of Biomechanical Engineering*, 2008.

[28] S. Ghouse, S. Babu, K. Nai, P. A. Hooper, and J. R. Jeffers, “The influence of laser parameters, scanning strategies and material on the fatigue strength of a stochastic porous structure,” *Additive Manufacturing*, vol. 22, pp. 290–301, 2017.

[29] X. Chen, T. Lian, B. Zhang, Y. Du, K. Du, N. Xiang, D.-W. Jung, G. Wang, and A. Osaka, “Design and Mechanical Compatibility of Nylon Bionic Cancellous Bone Fabricated by Selective Laser Sintering,” *Materials (Basel)*, vol. 14, no. 9, p. 1965, 2021.

[30] International Standard, *ISO 13314 - Mechanical testing of metals, ductility testing, compression test for porous and cellular metals*. 2011.

[31] M. Moesen, L. Cardoso, and S. C. Cowin, “A symmetry invariant formulation of the relationship between the elasticity tensor and the fabric tensor,” *Mechanics of Materials*, 2012.

[32] L. J. Gibson, “The mechanical behaviour of cancellous bone,” *Journal of Biomechanics*, 1985.

[33] International Standard, *ISO 13314 - Mechanical testing of metals, ductility testing, compression test for porous and cellular metals*. 2011.

[34] J. Souza, A. Großmann, and C. Mittelstedt, “Micromechanical analysis of the effective properties of lattice structures in additive manufacturing,” *Additive Manufacturing*, vol. 23, pp. 53–69, 10 2018.

[35] D. J. McGregor, S. Tawfick, and W. P. King, “Mechanical properties of hexagonal lattice structures fabricated using continuous liquid interface production additive manufacturing,” *Additive Manufacturing*, vol. 25, pp. 10–18, 1 2019.

[36] A. Ferrigno, F. Di Caprio, R. Borrelli, F. Auricchio, and A. Vigliotti, “The mechanical strength of Ti-6Al-4V columns with regular octet microstructure manufactured by electron beam melting,” *Materialia*, vol. 5, p. 100232, 3 2019.

[37] O. Rehme, “Cellular Design for Laser Freeform Fabrication, Schriftenreihe Lasertechnik,” *Cuvillier Verlag*, vol. 4, no. 1st edition, 2010.

[38] S. Ghouse, N. Reznikov, O. R. Boughton, S. Babu, K. G. Ng, G. Blunn, J. P. Cobb, M. M. Stevens, and J. R. Jeffers, “The design and in vivo testing of a locally stiffness-matched porous scaffold,” *Applied Materials Today*, vol. 15, pp. 377–388, 6 2019.

5 Implants that Generate Remodeling Strains in Bone

Abstract

An increase in strain between 1 and 10% compared to homeostasis can trigger bone formation. We aim to create an orthopedic implant using clinically established imaging and manufacturing methods that induces this strain control in human bone. Titanium scaffolds were manufactured with multiaxial apparent modulus tailored to the mechanical properties of bone defined from computed tomography scans of cadaver human tibiae. Five bone cubes were tested with corresponding titanium scaffolds by loading under compression, which is similar to the implanted tibia loading condition. Bone strain was precisely controlled by varying the scaffold modulus, from 0 to 15% bone strain increase. This strain increase is the magnitude reported to invoke bone's positive remodeling. Axial modulus was closely matched between titanium scaffolds and bone, ranging from 48-728 MPa and 81-800 MPa respectively, whereby scaffold axial modulus was within 2% of nominal target values. Fine control of multiaxial moduli resulted in transverse modulus that matched bone well; ranging from 42-648 MPa and 47-585 MPa in scaffolds and bone respectively. The scaffold manufacturing material and method are already used in the orthopedic industry. This study has significant clinical implications as it enables the design of implants which positively harness bone's natural mechanoresponse and respect bone's mechanical anisotropy and heterogeneity.

Credited authors include M.J. Munford, D. Xaio, J.R.T. Jeffers [1]

[1]This chapter has been published in the Journal for Orthopaedic Research, 2021, and presented as a podium presentation at the Orthopaedic Research Society annual meeting 2021.

5.1 Introduction

Bone exhibits a complex and dynamic behavior whereby biological and structural properties are influenced by a constant remodeling process. During this process, bone formation and resorption are controlled by osteoblast and osteoclast cell activity, each stimulated by multiple factors including localized strain gradient [1–3]. Many models explain how this mechanism influences the distribution of mechanical properties, most commonly to negative effect as in stress shielding and bone resorption after joint replacement surgery [4]. However the same remodeling process could be harnessed in a positive way, such as maintaining or increasing bone density after joint replacement surgery, if it were possible to increase the strain experienced by bone by between 1% and 8% of that seen under homeostasis [1, 5].

Porous scaffolds provide a promising opportunity in regenerative medicine to control the strain experienced by bone and thus induce positive remodeling. Such scaffolds have been explored in a variety of materials, structures and manufacturing methods to achieve a control of pore size, anisotropy and mechanical properties [6, 7]. Controlled modulus scaffolds have been manufactured in both metal and polymer materials in literature [8–13]. Furthermore, combinations of such materials and cell structures have produced varying mechanical anisotropies [14, 15]. In animal models, these scaffolds generate improved ingrowth and increased density of bone compared to solid metal controls [8, 11, 16, 17]. Similar studies have also observed that induced bone strain correlates with regeneration and remodeling [8, 15, 17].

Computational methods, such as topology optimization, allow the design of minimal surfaces to vary scaffold modulus as well as subsequent improvements in osseointegration and bone remodeling [6, 18]. Similarly, structures optimized for increased fluid flow and surface area provide good computational results for fixation and ingrowth [19, 20]. Bone remodeling appears to be its most effective when scaffold elastic tensor matches or is slightly higher than that of the host bone [6]. These studies demonstrate the theory of strain controlled bone remodeling, but this technology is yet to be demonstrated in an experimental human model.

The proximal tibia is a site of popular interest for orthopedic surgery, owing to the prevalence of osteoarthritis in the knee joint. Common successful procedures include total knee replacement, partial knee replacement and tibial osteotomy. These are well established successful procedures that use a metal implant to reconstruct the joint. These implants are made from solid Titanium or Cobalt Chrome alloy, many times stiffer than the bone into which they are placed. They therefore modify the strain distribution in the bone, leading to bone loss over time [21, 22]. Recent advances in manufacturing Titanium alloy in a scaffold format means it is now possible to make load bearing scaffolds with an apparent modulus

in the range of human bone [10]. For the proximal tibia, the modulus of the bone is well understood and can be predicted from quantified computed tomography (qCT) derived apparent density [14, 23–25]. Thus, it should now be possible to create tibial orthopedic implants that generate a strain gradient to maintain or improve the quality of the bone in the proximal tibia [1].

Loading in the proximal tibia is predominantly compressive and along the anatomical axis so controlling bone axial strain is a priority. Implants with apparent modulus designed to control bone mechanobiology would benefit from an improved understanding of how strain fields in bone can be controlled by implants in parallel loading. This could be particularly useful for early intervention treatments that are likely to be revised in the patient's lifetime. In order to do this, it is necessary to understand how porous structures with custom anisotropy can be designed to control multiaxial bone strain within a clinically viable workflow.

The focus of this study is to demonstrate how a Titanium scaffold implant can control bone strain in human proximal tibia bone. In addition to controlling bone strain in the dominant loading direction, a secondary focus is to match the transverse modulus of the bone in the off-axis directions.

5.2 Materials and Methods

5.2.1 Bone property measurement and prediction

Ethical permission was granted by the Imperial College Healthcare Tissue Bank Review Committee under a UK Human Tissue Authority License 12275. Our previous study reports the harvesting of 195 human bone cubes (9mm side length) from the proximal tibias of 7 fresh-frozen cadavers with no prior lower limb pathologies, traumas, surgeries or osteoarthritis (age = 34-65 years, sex = 5 females, 2 males, side = 4 left knees, 3 right knees). From the 195 cubes, 5 were selected to represent the variability in density of bone in the proximal tibia. Multiaxial apparent modulus was predicted for each cube from qCT with a calibration phantom using the methods described by Munford et al [14] These data were used as a target for the apparent modulus of the titanium scaffolds.

5.2.2 Titanium Lattice

Structure Generation

The stochastic structure was created by populating a 10mm side length cube with pseudo-random points using a Poisson disk algorithm, maintaining a specific minimum proximity. These points were then joined with lines to achieve a certain connectivity. This method, which uses Rhinoceros 6.0 and Grasshopper (Robert McNeel and Associates) is described by Ghouse et al. [10]. The density of the structure was 4.2 $struts/mm^3$ and with an average connectivity at each node of

5.3. Lines at an angle of less than 25° inclination to the x-y plane were kinked, as per the methods described by Hossain et al. to allow for additive manufacturing (AM) [26].

Control of Lattice Anisotropy

Scaffold mechanical anisotropy was controlled by selectively thickening struts based on their inclination angle to the x-y plane with 3 segments: 25-35°, 35-55° and 55-90°, which each contained 50.1%, 38% and 11.9% of total struts respectively. Specimens were designed with uniform strut thickness and all combinations of strut thicknesses of 200 μm, 300 μm and 400 μm allocated for each angular segment. Solid STL geometry is usually printed using a single exposure printing strategy [15]. To achieve the desired mechanical modulus throughout the structure in this small scale line geometry, this method was used to melt the required cross section of each strut, also described by Ghouse et al. [15]. Slice data (build files) were generated at 50 μm layer thickness using an in house slicing engine.

All specimens were printed using a Renishaw AM250 PBF AM system (Renishaw, Wooton Under Edge, UK). Commercially pure titanium (cpTi) spherical powder of particle size range 10–45 μm was used, supplied by Carpenter Additive (Pennsylvania, USA). The build chamber was vacuumed to -960 mbar and then back filled with 99.995% pure Argon to 10 mbar with an O content of 0.1%. Laser power was constant at 50W whilst exposure times varied from 600 to 1700 μs to maintain a constant strut thickness. All build plates were heat treated under vacuum at $750^{\circ}C$.

Specimens were removed from the buildplate by electro-discharge machining, ensuring that the wire path preserved the intended part geometry, then cleaned using ultrasonic bath and air jet. Specimens were cut down to 9mm side length cubes once support material had been removed.

Characterising Lattice Mechanical Properties

A materials testing machine (Instron 8872) with a 10-kN load cell was used to perform quasi-static compression testing at an extension rate of 2 mm/min, which corresponds to a strain rate within standard limits [19].

Displacement was measured using linear variable differential transformers (LVDTs), attached to the testing platens to reduce any compliance effects from the test apparatus. A sampling rate of 30 Hz was used. The platens of the machine were lubricated to reduce any frictional effects. Stress-strain curves were obtained using the individual macro dimensions of each specimen.

Specimens were tested in the axial and transverse directions sequentially with order of test directions randomized. The loading regime included a hysteresis loop to account for settling in behavior of the initial toe region within the porous

structure. For half of the cubes, this was carried out from 70% of the cube's yield stress (σ_{70}), to 20% of its yield stress (σ_{20}) and then back to σ_{70}. Specimens were tested in this way along three orthogonal test directions. All compression testing was done with lubricated platens to remove frictional artefacts. The elastic moduli were then calculated using a linear regression analysis of the hysteresis loop. Apparent modulus of specimens in both the axial and transverse directions were characterized in terms of the strut thickness distribution across each angular segment.

Mechanical Testing of Bone-Lattice Pairs

Each bone specimen was compression tested alongside a corresponding titanium scaffold following the same protocol as in Section 5.2.1 (Figure 5.1). Bone-scaffold pairs were compressed to a load corresponding to an induced stress of 1.5 MPa and the resulting strain measured. Prior to testing, specimens were trimmed with a Buehler precision saw (Germany) to ensure even distribution of load between the bone and scaffold at neutral loading.

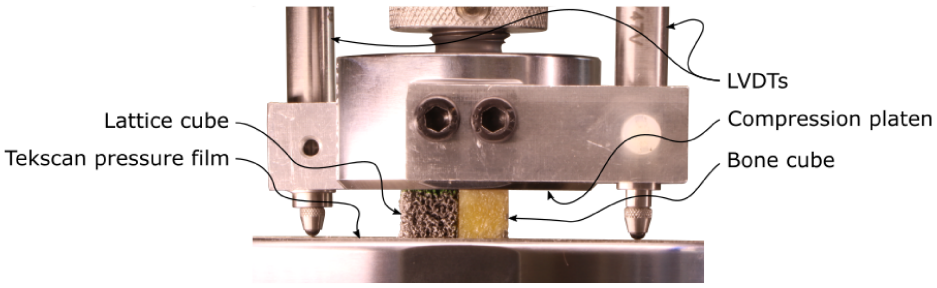


Figure 5.1: Mechanical parallel compression testing set up. Loading of a bone cube and corresponding lattice, with parallel platens, LVDTs and pressure film.

Prior to testing, Tekscan pressure sensors were equilibrated (800 N) and calibrated (2-point calibration) with a custom ball joint fixture to account for any machine misalignment (Appendix A.3). Equilibration allows equitable gain between sensels and calibration allows accurate calculation of force from the sensor's voltage readings. For each test, the Tekscan pressure sensor was single use. Prelimary testing showed that the sensors undergo a decay process between successive cycles, with the sensors reading inconsistent pressure magnitudes for successive loading. This was tested up to 15 cycles as shown in Figure 5.2 and a drop of 55% in pressure was observed. This was mitigated by equilibrating and calibrating each pressure sensor, then using it once for testing.

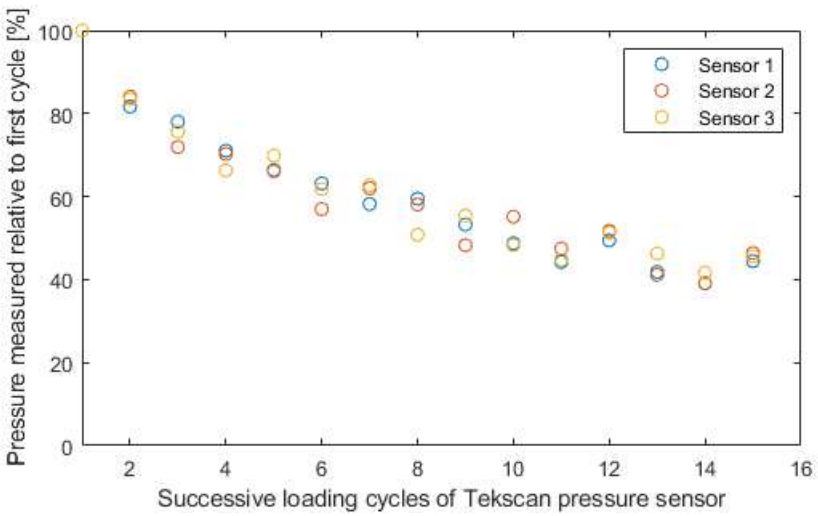


Figure 5.2: Tekscan pressure sensor decay. Succesive loading of a single pressure sensor with the same load applied resulted in errors and misreadings of the pressure applied. Pressure measured with each cycle is shown as a percentage of the pressure measured on the first cycle.

FE Modelling

For 4 bone cubes and their predicted moduli, 5 titanium lattices were manufactured with strut thicknesses assigned to have transverse modulus equal to predictions for the bone cubes and axial modulus scaled over a range based on the bone cube predictions. Lattice axial and transverse modulus was determined as in Section 5.2.1 (Table S1). The extremities of lattice axial modulus were always within 50% of bone axial modulus.

For 4 bone cubes and their predicted moduli, 5 titanium scaffolds were manufactured with strut thicknesses assigned to have transverse modulus equal to predictions for the bone cubes and axial modulus scaled over a range based on the bone cube predictions. Scaffold axial and transverse modulus was determined as in Section 5.2.1. Loading of each bone cube was modelled in parallel with their 5 corresponding scaffolds. Identical base constraints with a rigid top plate applied uniform loading up to 1.5 MPa compression via a frictionless surface contact constrained in the transverse plain. The bone-implant interface was modelled as a frictionless contact. 8-noded brick elements with a quadratic shape function were used and the mesh was varied linearly from coarse to fine elements at the interface. A mesh convergence was done which yielded a mesh consisting of an element density of 8000, N^2 of 1.15x10^{10} and a computational time 2233 times the most coarse mesh considered (element density 125 to validate convergence).

5.3 Control of Bone Strain

Strain in human proximal tibia bone was precisely controlled with titanium modified stochastic scaffold implant structures. Matching implant and bone modulus induced no change in bone strain for either mechanical testing or Finite Element (FE) models. A 13.3% reduction in implant modulus compared to the bone induced the target 10% increase in bone strain. Implant modulus and change in bone strain were linearly related (Figure 5.3, Table 5.1). Data from FE simulation was in strong agreement with results from mechanical testing.

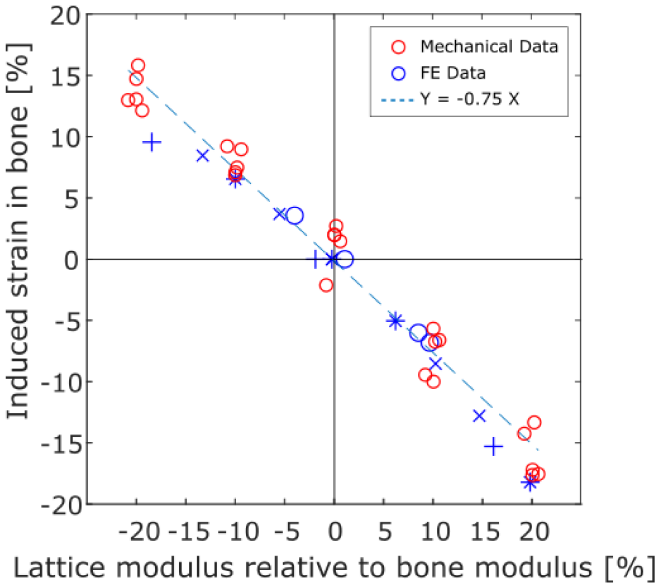


Figure 5.3: Induced strain response of bone as a function of change in lattice implant modulus. Mechanical compression testing in parallel (red) and FE data (blue) with trendline indicated. Bone cubes (n=5) had modulus ranging from 160-761 MPa.

Similarly, contact stress beneath the bone cube was controlled by varying implant modulus. A 10.4% increase in stress was induced in bone by reducing scaffold modulus by 20% (nominal) relative to the bone modulus (Figure 5.4, Table 5.2). These data indicate, under simple loading, an implant can create the appropriate strain in human bone for positive bone remodeling to occur.

Table 5.1: Induced bone strain for bone cubes and each corresponding lattice. Lattices aimed to achieve nominal relative moduli of -20%, -10%, 0%, 10% and 20%.

Bone Modulus [MPa]	Relative Lattice Modulus Change [%]				
	-20	-10	0	+10	+20
160	17.1	8.21	1.25	-8.30	-14.4
325	18.0	8.00	0.35	-8.89	-14.8
484	15.5	8.39	-0.81	-8.48	-12.2
627	12.4	10.0	2.70	-5.50	-17.1
761	13.40	6.34	0.91	-9.85	-13.8

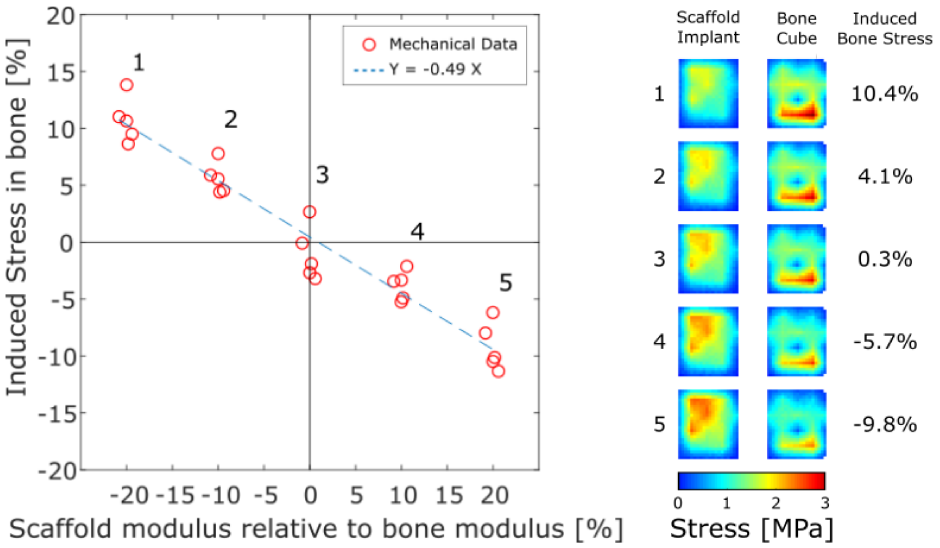


Figure 5.4: Relative stress induced in bone as a function of change in lattice implant modulus. Mechanical compression testing in parallel (red) with trend line indicated. Pressure maps and corresponding induced bone stress are shown for a given bone cube. Bone cubes (n=5) had modulus ranging from 160-761 MPa.

A non-homogeneous distribution of stress was observed at the Tekscan pressure film, this can be seen in Figure 5.4. This was shown to correlate well with the distribution of density within the bone cube, with a correlation coefficient of 0.87. For the bone cube shown in Figure 5.4, each sensel of Tekscan pressure film, the corresponding bone density, measured from CT data was compared (Figure 5.5). In this cube, the density ranged from 181 mg/cm^3 to 485 mg/cm^3 and the stress

at its surface ranged from 0.1 MPa to 3.1 MPa. This demonstrates that there were no significant effects of the bone cube shape from cutting on induced stresses.

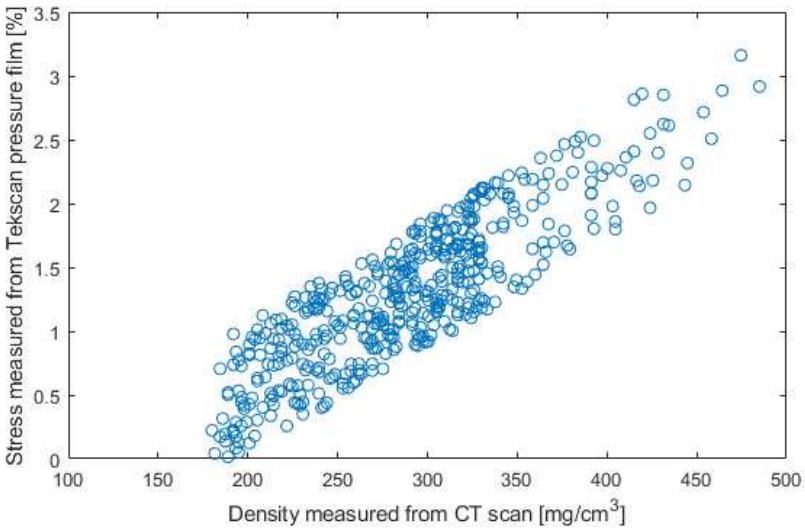


Figure 5.5: Stress distribution across the surface of bone cubes correlated with density distribution across the bone cube surface. Data shown for the bone cube in row 3 of Figure 5.4. For each sensel of Tekscan pressure film, the corresponding bone density, measured from CT data was compared. The stress across the bone cube and density had a correlation coefficient of 0.87.

Table 5.2: Induced bone stress for bone cubes and each corresponding lattice when loaded to 1 kPa. Lattices aimed to achieve nominal relative moduli of -20%, -10%, 0%, 10% and 20%.

Bone Modulus [MPa]	**Relative Lattice Modulus Change** [%]				
	-20	-10	0	+10	+20
160	10.2	6.46	0.50	-3.17	-7.80
325	12.9	6.99	-0.52	-3.83	-10.2
484	9.08	6.10	-0.12	-4.95	-7.57
627	11.7	5.90	1.59	-3.40	-8.66
761	10.4	4.10	0.30	-5.73	-9.8

Table 5.3: Bone-lattice axial modulus variation. Modulus for titanium lattices relative to their corresponding predicted bone modulus. Lattices aimed to achieve nominal relative moduli of -20%, -10%, 0%, 10% and 20%.

Bone Modulus	**Relative Lattice Modulus Change** [%]				
[MPa]	-20	-10	0	+10	+20
160	-21.0	-11.0	-1.04	8.96	19
325	-20.3	-10.2	-0.29	9.71	19.7
484	-19.8	-9.75	0.25	10.2	20.2
627	-20.3	-10.3	-0.3	9.70	19.7
761	-19.8	-9.77	0.23	10.2	20.2

5.4 Control of Lattice Anisotropy

Mechanical properties of the titanium lattice specimens were defined based on clinical CT scans of the intact tibia bone specimens. This method produced parts of the desired nominal modulus, with small errors across a range of modulus values (Table 5.3). When designed to match the bone modulus, the modulus of the Titanium scaffold structures were within 1% of their target value.

Control of strut thickening by angular segments allowed manufacture of structures with anisotropy in the range 1.1-5.1 (Table 5.4, Table 5.5). This was controlled by thickening struts by their inclination to the transverse plane. Anisotropy was controlled such that transverse modulus of the Titanium scaffold structures (42-648 MPa) matched that of the human tibia bone (47-585 MPa). Anisotropy ranged from 1.4-3.4 and 1.1-5.1 in bone and scaffolds respectively. For a given bone cube, scaffolds were manufactured to have axial and transverse moduli within 2% and 12% respectively of their nominal values, based on CT predictions.

A strong power-law correlation was found between apparent modulus and uniform strut thickness. When the structure was thickened uniformly from 200 μm to 400 μm the relationship could be fitted well with a trend which achieved an R^2 of 0.99.

5.5 Discussion

5.5.1 Summary of Results

The most important outcome of this study was the that the axial strain experienced by human proximal tibia trabecular bone could be controlled by titanium scaffold structures whose modulus was defined from clinical CT scans. The resulting strain response in bone was controlled by an inverse linear relationship with the titanium scaffold structure's apparent modulus. The titanium scaffold structures were manufactured with apparent modulus within 2% and 12% of target axial

Table 5.4: Bone-lattice transverse modulus variation. Transverse modulus for bone and each corresponding lattice with varied axial modulus.

Bone Transverse Modulus	**Lattice Transverse Modulus** [MPa]				
[MPa]	-20	-10	0	+10	+20
47.1	63.2	33.6	31.6	70.1	73.2
120	121.8	135.3	145.7	155.8	137.3
255	282.4	284.4	282.2	286.9	270
369	404.4	390.7	403	390.9	408.7
585	637.9	643	628.1	664.6	654.5

Table 5.5: Bone-lattice anisotropy variation. Anisotropy for bone and each corresponding lattices with varied axial modulus.

Bone Anisotropy	**Lattice Anisotropy**				
Axial modulus change	-20	-10	0	+10	+20
3.4	2.0	4.3	5.1	2.5	2.6
2.7	2.1	2.2	2.2	2.3	2.8
1.9	1.4	1.5	1.7	1.9	2.2
1.7	1.2	1.4	1.6	1.8	1.8
1.3	1.1	1.1	1.2	1.3	1.4

and transverse modulus based on CT predictions of the bone apparent modulus. These data indicate that a proximal tibial knee replacement implant could be made from a titanium scaffold structure to control the strain in the proximal tibial bone after knee replacement surgery. This is an important step towards the vision of implants that can maintain natural bone homeostasis or even improve the bone's mechanical properties throughout the life of the implant.

5.5.2 Comparison to Literature

Our data compare well with animal models that have observed the relationship between bone strain and regeneration in vivo [8, 15, 17]. In particular, load sharing implants have been shown to be beneficial for ingrowth and scaffolds with a lower modulus have been shown to increase ingrowth [8]. This supports the trends found in our study, where scaffolds of a lower modulus induced greater bone strains. Furthermore, repeating cell polymer scaffolds of a 220 MPa modulus induced ingrowth as high as 21% [27]. This corresponds well to our findings; where scaffolds with modulus between 128 and 609 MPa (20% less than surrounding bone) increased the strain by between 12.4% and 18%.

Scaffolds with apparent modulus in the range of 0.6-3.6 GPa for titanium alloys

and 0.15-7.1 GPa for polymer structures have been previously reported, similar to our study [8–15]. Many studies have also demonstrated a range of mechanical anisotropies in porous scaffolds [14, 15]. The methods shown here provide a good development to existing literature, allowing axial modulus to be designed between 132 and 913 MPa while controlling anisotropy such that transverse modulus can be designed to within 12% or 64 MPa of its target value. Our method of controlling anisotropy was to modify the scaffolds based on strut inclination angles. Similar results in literature suggest topology optimization of minimal surfaces can modify scaffold modulus over the range 1.2 to 8 with subsequent variations in bone remodeling [6, 18]. Bone remodeling appears to be its most effective when scaffold elastic tensor matches or is slightly higher than that of the host bone, which is reflected in our data [6].

Controlled strains between 50 and 4000 microstrain have been recorded in animal models using external fixators, whole body vibration and strain gauges which allow in-situ measurements of loading and strain [28, 29]. Our study adds to literature further, inducing between 1800 and 3600 microstrain, depending on the designed scaffold modulus. Bone adaptation is threshold driven and influenced by strain magnitude, strain rate and waveform and loading distribution [30]. Literature suggests that bone formation (34% increase in bone density) can be achieved even at low level strains (5 microstrain, 0.5% delta strain) providing frequent periods of high frequency strain (30 Hz) [29]. Previous work has shown the benefits of load sharing bone scaffolds and reduced modulus implants as well as the opportunity of varying bone strain in-vivo. Our findings support prior work by allowing fine control of strain for positive and negative deviations from homeostasis for the first time in human bone in a way which could be utilized in an implant.

5.5.3 Considerations

A limitation of the study was that compression testing was done quasi-statically which neglects dynamic loading. This does not reflect physiological loading which is often cyclic, however quasi-static testing allowed comparison of modulus values with literature and has been shown to correlate well with cyclic loading results [31]. Another limitation is that the loading configuration was a simplified loading configuration of the proximal tibial bone construct, but we chose this model because the dominant strains are in the axial direction, similar to the proximal tibia. The finite element model also assumed simple continuum linear elastic material properties which is only valid in the linear elastic range, but nevertheless matched the experimental data in this range with errors less than 8%, with an average of 2%. The final limitation was that bone strain was controlled with scaffolds in only 5 specimens, however, specimens were chosen such that their axial modulus spanned a representative range of values and the resulting data trend was clear

and statistically significant.

5.5.4 Clinical Significance

This study is clinically relevant because follow up data indicate implants with reduced modulus can influence outcome. For example, in a randomized controlled trial, a tantalum trabecular metal tibial implant had improved radiological outcome compared to a solid tibial implant over a period of 15 years [32]. Another example is that the likelihood of a complex revision is reduced if the primary implant is a low modulus all polyethylene design compared to a conventional solid metal backed design[33]. Our method builds on these findings by allowing precise control of bone strain, using a manufacturing method that has already been deployed in over 1 million knee replacement implants. The workflow for generating stiffness matched implants which control bone strain response is therefore closer to clinical use than most regenerative technology. The ability to harness bone's natural mechanoresponse has the potential to revolutionize the orthopedic industry with implants that actively improve the quality of the bone into which they are placed.

5.6 Conclusion

Precise control of strain in bone could be beneficial for joint replacement implant designs. In a simplified model of implanted bone, Titanium lattice structures could control the strain in bone from +0% to +15% strain compared to the native bone. This range of strain increase is within the range to invoke bone's positive remodeling stimulus.

5.7 Bibliography

[1] D. S. Elliott, K. J. H. Newman, D. P. Forward, D. M. Hahn, B. Ollivere, K. Kojima, R. Handley, N. D. Rossiter, J. J. Wixted, R. M. Smith, and C. G. Moran, "A unified theory of bone healing and nonunion BHN THEORY,"

[2] G. M. Pagnotti, M. Styner, G. Uzer, V. S. Patel, L. E. Wright, K. K. Ness, T. A. Guise, J. Rubin, and C. T. Rubin, "Combating osteoporosis and obesity with exercise: leveraging cell mechanosensitivity," *Nature Reviews Endocrinology*, vol. 15, no. 6, pp. 339–355, 2019.

[3] C. T. Rubin and L. E. Lanyon, "Regulation of bone formation by applied dynamic loads," *Thr Journal of Bone and Joint Surgery*, vol. 66, no. April, pp. 397–402, 1984.

[4] R. Huiskes, H. Weinans, and B. van Rietbergen, “The relationship between stress shielding and bone resorption around total hip stems and the effects of flexible materials.,” *Clinical orthopaedics and related research*, vol. 274, no. Jan, pp. 124–134, 1992.

[5] C. H. Turner, M. R. Forwood, J. ho, and T. Yoshikawa, “Mechanical loading thresholds for lamellar and woven bone formation,” *Journal of Bone and Mineral Research*, vol. 9, no. 1, pp. 87–97, 1994.

[6] S. Sturm, S. Zhou, Y. W. Mai, and Q. Li, “On stiffness of scaffolds for bone tissue engineering-a numerical study,” *Journal of Biomechanics*, vol. 43, no. 9, pp. 1738–1744, 2010.

[7] L. Zhu, D. Luo, and Y. Liu, “Effect of the nano/microscale structure of biomaterial scaffolds on bone regeneration,” *International Journal of Oral Science*, vol. 12, no. 1, pp. 1–15, 2020.

[8] N. Reznikov, O. R. Boughton, S. Ghouse, A. E. Weston, L. Collinson, G. W. Blunn, J. R. Jeffers, J. P. Cobb, and M. M. Stevens, “Individual response variations in scaffold-guided bone regeneration are determined by independent strain- and injury-induced mechanisms,” *Biomaterials*, vol. 194, pp. 183–194, 2 2019.

[9] S. Naghieh, M. R. Karamooz Ravari, M. Badrossamay, E. Foroozmehr, and M. Kadkhodaei, “Numerical investigation of the mechanical properties of the additive manufactured bone scaffolds fabricated by FDM: The effect of layer penetration and post-heating,” *Journal of the Mechanical Behavior of Biomedical Materials*, vol. 59, pp. 241–250, 2016.

[10] S. Ghouse, N. Reznikov, O. R. Boughton, S. Babu, K. G. Ng, G. Blunn, J. P. Cobb, M. M. Stevens, and J. R. Jeffers, “The design and in vivo testing of a locally stiffness-matched porous scaffold,” *Applied Materials Today*, vol. 15, pp. 377–388, 6 2019.

[11] R. Wauthle, J. Van Der Stok, S. A. Yavari, J. Van Humbeeck, J. P. Kruth, A. A. Zadpoor, H. Weinans, M. Mulier, and J. Schrooten, “Additively manufactured porous tantalum implants,” *Acta Biomaterialia*, vol. 14, pp. 217–225, 3 2015.

[12] J. Wieding, T. Lindner, P. Bergschmidt, and R. Bader, “Biomechanical stability of novel mechanically adapted open-porous titanium scaffolds in metatarsal bone defects of sheep,” *Biomaterials*, vol. 46, pp. 35–47, 4 2015.

[13] H. Spece, T. Yu, A. Law, M. Marcolongo, and S. Kurtz, “3D printed porous PEEK created via fused filament fabrication for osteoconductive orthopaedic surfaces,” *Journal of the Mechanical Behavior of Biomedical Materials*, vol. 109, p. 103850, 2020.

[14] M. J. Munford, K. C. G. Ng, and J. R. T. Jeffers, “Mapping the Multi-Directional Mechanical Properties of Bone in the Proximal Tibia,” *Advanced Functional Materials*, vol. 30, p. 2004323, 2020.

[15] S. Ghouse, S. Babu, R. J. Van Arkel, K. Nai, P. A. Hooper, and J. R. Jeffers, “The influence of laser parameters and scanning strategies on the mechanical properties of a stochastic porous material,” *Materials and Design*, pp. 498–508, 2017.

[16] J. Henkel, M. A. Woodruff, D. R. Epari, R. Steck, V. Glatt, I. C. Dickinson, P. F. M. Choong, M. A. Schuetz, and D. W. Hutmacher, “Bone Regeneration Based on Tissue Engineering Conceptions — A 21st Century Perspective,” *Bone Research*, vol. 1, pp. 216–248, 2014.

[17] A.-M. Pobloth, S. Checa, H. Razi, A. Petersen, J. C. Weaver, K. Schmidt-Bleek, M. Windolf, A. Tatai, C. P. Roth, K.-D. Schaser, G. N. Duda, and P. Schwabe, “Mechanobiologically optimized 3D titanium-mesh scaffolds enhance bone regeneration in critical segmental defects in sheep.,” *Science translational medicine*, vol. 10, 1 2018.

[18] E. Sallica-Leva, A. L. Jardini, and J. B. Fogagnolo, “Microstructure and mechanical behavior of porous Ti-6Al-4V parts obtained by selective laser melting,” *Journal of the Mechanical Behavior of Biomedical Materials*, vol. 26, pp. 98–108, 2013.

[19] S. Zhao, M. Arnold, S. Ma, R. L. Abel, J. P. Cobb, U. Hansen, and O. Boughton, “Standardizing compression testing for measuring the stiffness of human bone,” *Bone & Joint Research*, vol. 7, no. 8, pp. 524–538, 2018.

[20] C. Perier-Metz, G. N. Duda, and S. Checa, “Mechano-Biological Computer Model of Scaffold-Supported Bone Regeneration: Effect of Bone Graft and Scaffold Structure on Large Bone Defect Tissue Patterning,” *Frontiers in Bioengineering and Biotechnology*, vol. 8, no. November, pp. 1–15, 2020.

[21] C. Yoon, M. J. Chang, C. B. Chang, M. K. Song, J. H. Shin, and S. B. Kang, “Medial Tibial Periprosthetic Bone Resorption and Its Effect on Clinical Outcomes After Total Knee Arthroplasty: Cobalt-Chromium vs Titanium Implants,” *Journal of Arthroplasty*, vol. 33, pp. 2835–2842, 9 2018.

[22] J. T. Deen, T. B. Clay, D. A. Iams, M. B. Horodyski, and H. K. Parvataneni, “Proximal tibial resorption in a modern total knee prosthesis,” *Arthroplasty Today*, vol. 4, pp. 244–248, 6 2018.

[23] E. F. Morgan, H. H. Bayraktar, and T. M. Keaveny, “Trabecular bone modulus–density relationships depend on anatomic site,” *Journal of Biomechanics*, vol. 36, pp. 897–904, 7 2003.

[24] D. R. Carter and W. C. Hayes, “The compressive behavior of bone as a two-phase porous structure,” *Bone & Joint Research America*, vol. 59, pp. 954–962, 1 1977.

[25] F. Linde, B. Pongsoipetch, L. H. Frich, and I. Hvid, “Three-axial strain controlled testing applied to bone specimens from the proximal tibial epiphysis,” *Journal of Biomechanics*, vol. 23, pp. 1167–1172, 1 1990.

[26] U. Hossain, S. Ghouse, K. Nai, and J. Jeffers, “Mechanical and morphological properties of additively manufactured SS316L and Ti6Al4V micro-struts as a function of build angle,” *Additive Manufacturing*, vol. 46, p. 102050, 5 2021.

[27] A. Trepczynski, I. Kutzner, P. Schütz, J. Dymke, R. List, P. von Roth, P. Moewis, G. Bergmann, W. R. Taylor, and G. N. Duda, “Author Correction: Tibio-Femoral Contact Force Distribution is Not the Only Factor Governing Pivot Location after Total Knee Arthroplasty (Scientific Reports, (2019), 9, 1, (182), 10.1038/s41598-018-37189-z),” 12 2019.

[28] J. C. Fritton, C. T. Rubin, Y. X. Qin, and K. J. McLeod, “Whole-Body Vibration in the Skeleton : Development of a Resonance-Based Testing Device Feedback RMS-to-DC Amplifier Converter,” *Annals of Biomedical Engineering*, vol. 25, pp. 831–839, 1997.

[29] C. Rubin, A. S. Turner, S. Bain, C. Mallinckrodt, and K. McLeod, “Low mechanical signals strengthen long bones,” *Nature*, vol. 412, no. 6847, pp. 603–604, 2001.

[30] M. R. Forwood and C. H. Turner, “Skeletal adaptations to mechanical usage: results from tibial loading studies in rats,” *Bone*, vol. 17, pp. 197–205, 10 1995.

[31] S. Ghouse, S. Babu, K. Nai, P. A. Hooper, and J. R. Jeffers, “The influence of laser parameters, scanning strategies and material on the fatigue strength of a stochastic porous structure,” *Additive Manufacturing*, vol. 22, pp. 290–301, 2017.

[32] M. Hampton, J. Mansoor, J. Getty, and P. M. Sutton, “Uncemented tantalum metal components versus cemented tibial components in total knee arthroplasty: 11- to 15-year outcomes of a single-blinded randomized controlled trial,” *The Bone & Joint Journal*, vol. 102-B, pp. 1025–1032, 8 2020.

[33] C. E. Scott, F. A. Wade, R. Bhattacharya, D. MacDonald, P. Pankaj, and R. W. Nutton, “Changes in Bone Density in Metal-Backed and All-Polyethylene Medial Unicompartmental Knee Arthroplasty,” *Journal of Arthroplasty*, vol. 31, pp. 702–709, 3 2016.

6 Implants that Maintain Native Tibial Load Transfer

Abstract

Unicompartmental and total knee arthroplasty (UKA and TKA) are successful treatments for osteoarthritis, but the solid metal implants disrupt the natural distribution of stress and strain which can lead to bone loss over time. This generates problems if the implant needs to be revised. This study investigates whether titanium lattice UKA and TKA implants can maintain natural load transfer in the proximal tibia. In a cadaveric model, UKA and TKA procedures were performed on 8 fresh-frozen knee specimens, using conventional (solid) and titanium lattice tibial implants. Stress at the bone-implant interfaces were measured and compared to the native knee. Titanium lattice implants were able to restore the mechanical environment of the native tibia for both UKA and TKA designs. Maximum stress at the bone-implant interface ranged from 1.2-3.3 MPa compared to 1.3-2.7 MPa for the native tibia. The conventional solid UKA and TKA implants reduced the maximum stress in the bone by a factor of 10 and caused >70% of bone surface area to be underloaded compared to the native tibia. Titanium lattice implants maintained the natural mechanical loading in the proximal tibia after UKA and TKA, but conventional solid implants did not. This is an exciting first step towards implants that maintain bone health, but such implants also have to meet fatigue and micromotion criteria to be clinically viable.

Credited authors include M.J. Munford, J.C. Stoddart, A.D. Liddle, J.P. Cobb, J.R.T. Jeffers [1]

[1] This chapter has been published in Bone and Joint Research, 2022, and presented at a podium presentation at the International Society for technology in Arthroplasty, 2022.

6.1 Introduction

Knee arthroplasty procedures are highly successful interventions for the relief of pain and improvement in function of patients with osteoarthritis; worldwide, 1.5 million procedures are performed annually. Conventional arthroplasty implants are made from solid metal, usually titanium or cobalt-chromium alloys. These alter the forces applied to the metaphyseal bone which in turn disrupts the bone's natural distribution of stress and strain, causing a detectable loss of bone quality as soon as 2 years post-surgery [1, 2]. This loss of bone quality and density in the tibia following arthroplasty is undesirable but nevertheless tolerated because current generation implants have excellent rates of survival, with typically 95% of cases recorded in joint registries surviving more than 10 years [3]. However, for patients under the age of 60, one in three will need a revision at some point in their life [4]. An improvement to this status quo could be achieved for these patients if the periprosthetic bone density and strength were maintained throughout the life of the primary implant.

The problem of bone resorption is a consequence of the natural mechanical loading environment being disrupted by the presence of the implant [5]. Bone formation and resorption are controlled by osteoblast and osteoclast cell activity, each stimulated by multiple factors including localised strain gradient [6–8]. Models within the literature, such as Frost's mechanostat, Wolff's law and Perren's strain theory explain how this mechanism influences the complex and dynamic distribution of mechanical properties in bone [6, 9, 10]. It may be possible to harness this remodelling process to maintain bone density after joint replacement surgery. This would require implants with material properties which do not disturb the bone's natural mechanical loading environment [6, 11].

Additive manufacture (AM) is a viable route to manufacture orthopaedic implants and allows the creation of titanium lattices that control the strain experienced by bone and thus induce positive remodelling. Such lattices have been explored in a variety of materials, structures and manufacturing methods to achieve control of pore size, anisotropy and mechanical properties [12–18]. Furthermore, combinations of such materials and structures have produced varying mechanical anisotropies [19, 20]. In animal models, these lattices can accelerate bone formation and increase bone density compared to solid metal controls [13, 16, 21, 22]. AM titanium structures have also been shown to offer improved long-term fixation which could prove beneficial in cementless arthroplasty [23, 24]. These findings indicate the huge potential of AM technology in orthopaedics, but have yet to be applied to an orthopaedic implant in a human model.

This study aimed to demonstrate that UKA and TKA tibial implants made from titanium lattice material could replace the tibial condyle surface while minimising disruption of the bone's natural mechanical loading environment. A secondary

aim was to determine whether a titanium lattice implant with a graded modulus throughout the implant would generate a more natural load transfer than one with a uniform modulus. This study was conducted in a human cadaveric model.

6.2 Methods

6.2.1 Implant Design and Manufacture

The study includes uncemented medial unicompartmental knee arthroplasty (UKA) and total knee arthroplasty (TKA) tibial implants manufactured from conventional solid titanium and titanium lattice material. In all cases a fixed bearing polyethylene bearing surface was used. The TKA implant had a keel spanning the distance between each condyle's dwell points.

The conventional solid UKA and TKA tibial implants were called M0 and T0 respectively. The titanium lattice UKA and TKA tibial implants were called M1-M4 and T1-T4 respectively (Table 6.1). M1 and T1 had a uniform axial modulus of 0.6 GPa. M2 and T2 had an axial modulus of 0.6 GPa and transverse modulus of 0.45 GPa. M3 and T3 had a uniform axial modulus of 3.3 GPa. M4 and T4 had a graded axial modulus of 0.4-0.7 GPa to match the stiffness gradient in the proximal tibia measured in a previous study [19].

Table 6.1: Description of implant variants tested. Where mechanical properties of the proximal tibia have been matched, values were taken from existing literature [19].

Implant	Description	Mechanical Modulus
T0, M0	Conventional solid implant	E_{Axial} = 113 GPa
T1, M1	Uniform axial modulus matched to the mean value in the proximal tibia.	E_{Axial} = 0.6 GPa
T2, M2	Uniform axial and transverse modulus matched to the mean value in the proximal tibia.	E_{Axial} = 0.6 GPa $E_{Transverse}$ = 0.45 GPa
T3, M3	Uniform axial modulus set similar to that in the proximal tibia.	E_{Axial} = 3.3 GPa
T4, M4	Graded axial modulus graded across the implant to replicate differences found across native condyles and subchondral depth, with a solid cortical rim.	E_{Axial} = 0.4-0.7 GPa

Titanium lattice tibial components were made by filling component geometry with a stochastic structure. This method uses Rhinoceros 6 and Grasshopper (Robert McNeel and Associates) and is described in literature [25].

All implants were manufactured using a Renishaw AM250 PBF additive manufacturing system (Renishaw, Wotton Under Edge, UK) with commercially pure titanium ASTM B348 grade 2 spherical powder (15–45 μm diameter), supplied by Carpenter Additive (Philadelphia, USA). Laser power was constant at 50W whilst exposure times varied from 100-1200 μs to achieve the desired apparent modulus. Specimens were heat treated at 750°C.

6.2.2 Surgical Planning and Specimen Preparation

Cadaveric human tissue was obtained from 8 donors with no prior lower limb pathologies, traumas or surgeries (age: 66-72 years, sex: 8 male). Ethical permission was granted and investigations conformed with the research principles and study protocol as approved by the institution's research ethics boards. Tissue was frozen within 24 hours post-mortem. Once thawed, all tissues apart from the extensor mechanism, collaterals, cruciates, capsule and menisci were removed prior to surgical procedure. Each specimen underwent the same schedule of freeze-thaw cycles, seeking to minimise the number of cycles. The samples went through a cycle of freezing and thawing in each of the following stages, totalling 4 cycles:

- Shipping from supplier
- CT scan imaging
- Performing UKA surgery and conducting UKA testing (same day)
- Performing TKA surgery and conducting TKA testing (same day)

This study design minimised the number of freeze-thaw cycles, randomised testing order of repeated-measures and tested in order of increasing invasiveness, as suggested by literature [26–29]. In particular, this study design ensured surgeries were performed on the same day as the specimens were tested.

A conventional computed tomography (CT) scanner (SOMATOM Definition AS; SIEMENS AG) was used to image all specimens using a clinical imaging protocol (512 × 512 resolution, 120 kVp, 0.6 mm slice thickness, 0.5 mm pixel spacing) with a 5-material calibration phantom (Model 3; Mindways Software Inc) for bone mineral densitometry. Following scanning, 3D models of the specimens were segmented from the scan slices (Mimics, Materialise), Figure 6.1a.

Surgeries were planned on the basis of the preoperative CT to recreate mechanical alignment and constitutional varus (0-3°), Figure 6.1b. Surgeries

were conducted by a board-certified consultant orthopaedic knee reconstruction surgeon (ADL). First, a medial UKA was performed as planned using conventional instrumentation (Oxford Microplasty instruments, Zimmer Biomet, Bridgend, UK). Following the UKA tests, the surgeon performed TKA on the same specimens using specimen specific cutting guides, Figure 6.1c.

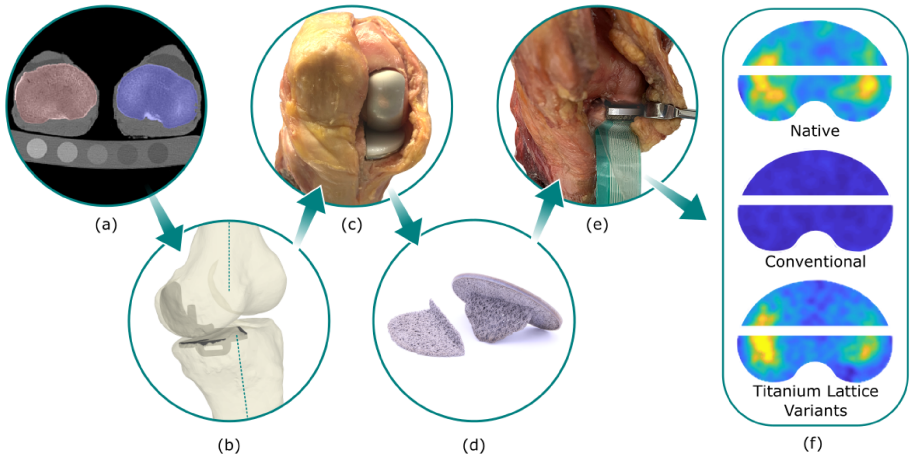


Figure 6.1: Summary of the methods for planning surgeries, preparing and testing cadaveric specimens. (a) CT scan of specimens with calibration phantom. (b) Surgical plans made based on specimen geometry and anatomical axes. (c) Surgeries conducted and implants fit by a consultant surgeon. (d) Additive manufactured UKA and TKA tibial implants. (e) Pressure film was placed at the bone-implant interface. (f) Pressure maps were found for the native case, conventional implants and titanium lattice implant variants.

6.2.3 Knee loading

The proximal femur and distal tibia were potted in fixtures aligned to their anatomical axes using intramedullary rods to align in the sagittal and coronal planes. To ensure a natural alignment for each specimen, there were three rotational degrees of freedom on the femoral fixture (Figure 6.2a), two translational degrees of freedom (AP and ML) on the tibial fixture (Figure 6.2b) and the third translational degree of freedom (axial) was the direction of the actuator of the materials testing machine (Instron 8872, 10kN load cell). All degrees of freedom were released, specimens were placed in 0° flexion and an axial load of 700N was applied to find the natural position of the tibia relative to the femur. This moved the femur into 5°-7° varus relative to the tibia. For each specimen, once this position was found, all degrees of freedom were fixed to ensure the same loading was applied to that specimen for native, UKR and TKR cases. Loading was applied in position control at 2 mm/min to a magnitude of 700N where it

was then held in load control and contact pressure data captured immediately to minimise any viscoelastic effects. The 700N load is representative of the contact force during two legged stance (Figure 6.1d). In addition, the extensor mechanism was tensioned at 21N to provide an upward force from the tibial tubercle [30].

Contact stress at the tibial bone-implant interface was measured with pressure film sensors (Tekscan, MA, USA) following a similar method to Verstraete et al. [31]. The UKA tibial bone cuts were made, bone fragment kept in place, a single pressure sensor (I-scan 4011) placed in the transverse cut and contact pressure captured under the applied load. The femoral bone cuts were then made and the femoral component inserted. Each of the five UKR tibial components (M0-M4) were subsequently implanted in randomised order and contact pressures again captured under the same applied load. The TKR tibial bone cuts were then made and the process repeated for the TKA implants except 2 sensors (I-scan 5011) were used anterior and posterior to the tibial keel respectively (Figure 6.1d, Figure 6.1e and Figure 6.1f). To check that contact pressure for the native case was not affected by the necessary sagittal cut to accommodate the pressure sensor we performed a finite element analysis of the intact tibia vs. one with the transverse cut made and contact pressures were within 3% for all cases.

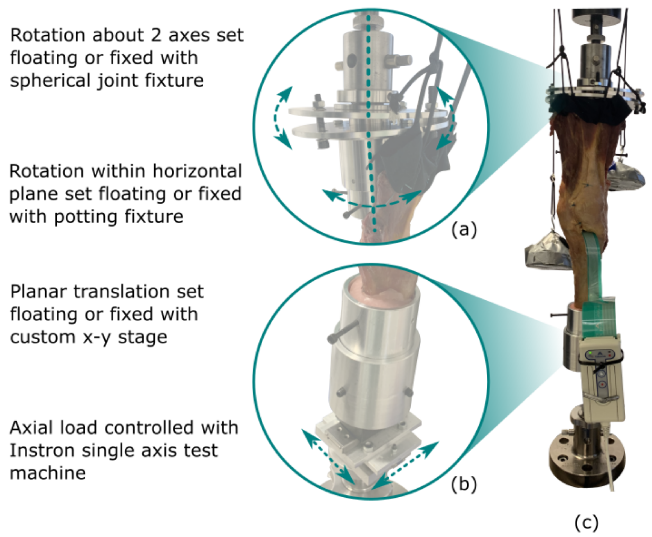


Figure 6.2: Test setup and constraining of the knee Native alignment and condylar dwell points were found with custom fixtures to set (a) rotational degrees of freedom and (b) translational degrees of freedom floating or fixed before (c) testing specimens in extension under body weight axial loading.

6.2.4 Analysis of Data

A histogram plot of the pressure sensor data was captured to allow comparison between the natural, UKR and TKR cases. Similarity of the bone-implant interface stress distribution between each implant and the native case was measured as the Jaccard similarity (S) which is defined as the intersection of stress surfaces divided by the union of stress surfaces [32]. The percentage of interface area underloaded (A) relative to native bone was calculated directly from the pressure sensor histogram data. One-way ANOVAs with Bonferoni post-hoc tests were performed on the Jaccard similarity and maximum stress in each condyle, with implant variant as a factor group. For TKA maximum stress data, both condyles were considered separately with T-tests performed to determine any differences between them.

6.3 Results

6.3.1 UKA Results

Stress Distribution

The titanium lattice implants (M1-M4) replicated the native stress distribution in the medial condyle, Figure 6.3. Stress at the bone-implant interface was at least 71.2% similar to the native case, with less than 5% of interface area underloaded, Table 6.2. For the conventional implant (M0), stress distribution was only 19.8% similar to the native case. This resulted in bone beneath the dwell point being comparatively underloaded. This underloaded bone covered 71% of the bone-implant interface area.

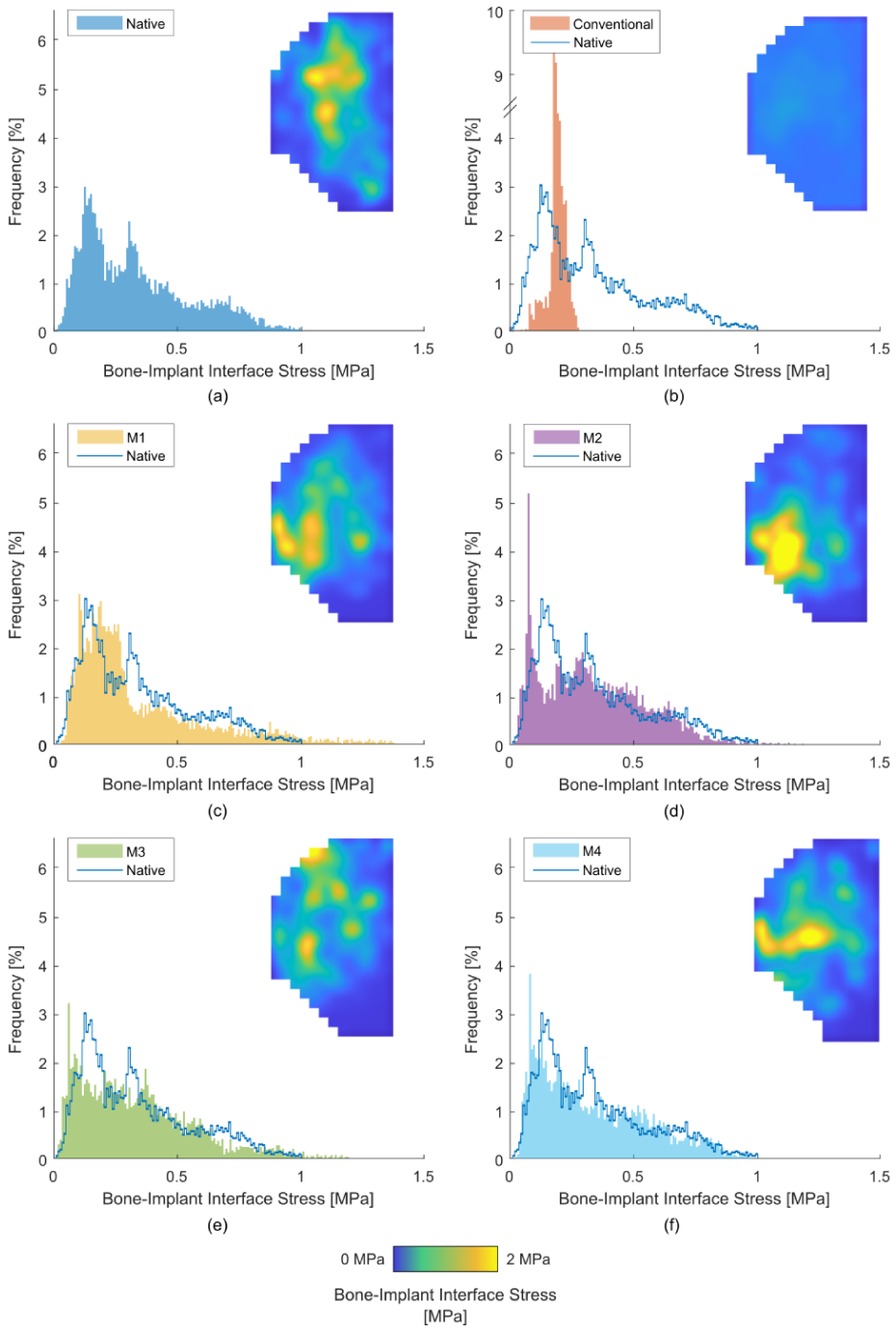


Figure 6.3: Bone-implant interface stress distribution in UKA. Average stress maps and histogram plots of bone-implant interface stress in UKA for (a) the native case, (b) conventional implants and the additive manufactured variants; (c) M1, (d) M2, (e) M3 and (f) M4. Note the break in axis of Figure b.

Maximum induced stress

The maximum stress in the medial condyle was not changed by the titanium lattice implants (M1-M4) compared to the native case ($p>0.05$) and was between 1.5 and 2.5 MPa for all cases (Figure 6.4, Table 6.2). No difference was detected between M1-M4. For the conventional implant (M0), the maximum stress was 10 times lower than the native case ($p<0.01$) with a value of 0.2 MPa, Figure 6.4, Table 6.2.

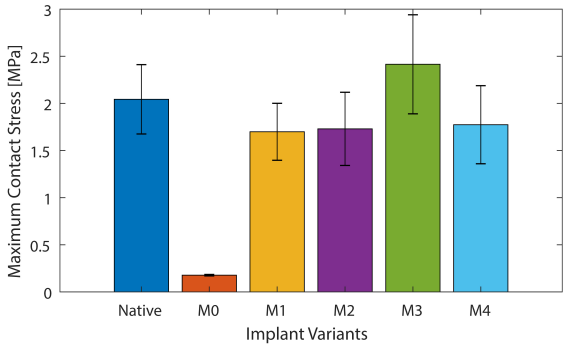


Figure 6.4: Maximum bone-implant interface stress in UKA. Maximum stress for medial UKA loading, for all test variants.

Table 6.2: Summary of results for UKA implant variants. Mean measures for similarity of stress distribution [%], percentage of interface area underloaded compared to the native case [%] and maximum stress [MPa] in the medial UKA.

Test Variant	Jaccard Similarity [%]	Area Underloaded [%]	Maximum Stress [MPa]
Native	-	-	2.0±0.7
M0	19.8±0.6	71.1±1.2	0.2±0.0
M1	76.9±1.8	1.2±1.0	1.7±0.6
M2	74.3±1.1	3.6±2.1	1.7±0.8
M3	71.2±2.3	5.0±1.7	2.4±0.9
M4	75.4±3.0	2.7±2.2	1.8±0.8

6.3.2 TKA Results

Stress Distribution

Across the whole bone-implant interface, the titanium lattice implants (T1-T4) replicated the native stress distribution in the medial condyle but there was no difference between M1, M2, M3 or M4, Figure 6.5. Stress at the bone-implant

interface was at least 67.8% similar to the native case, with less than 1.7% of interface area underloaded, Table 6.3. For the conventional implant (T0), stress distribution was only 20.5% similar to the native case. This resulted in bone beneath the dwell points being comparatively underloaded. This underloaded bone covered 77% of the bone-implant interface area.

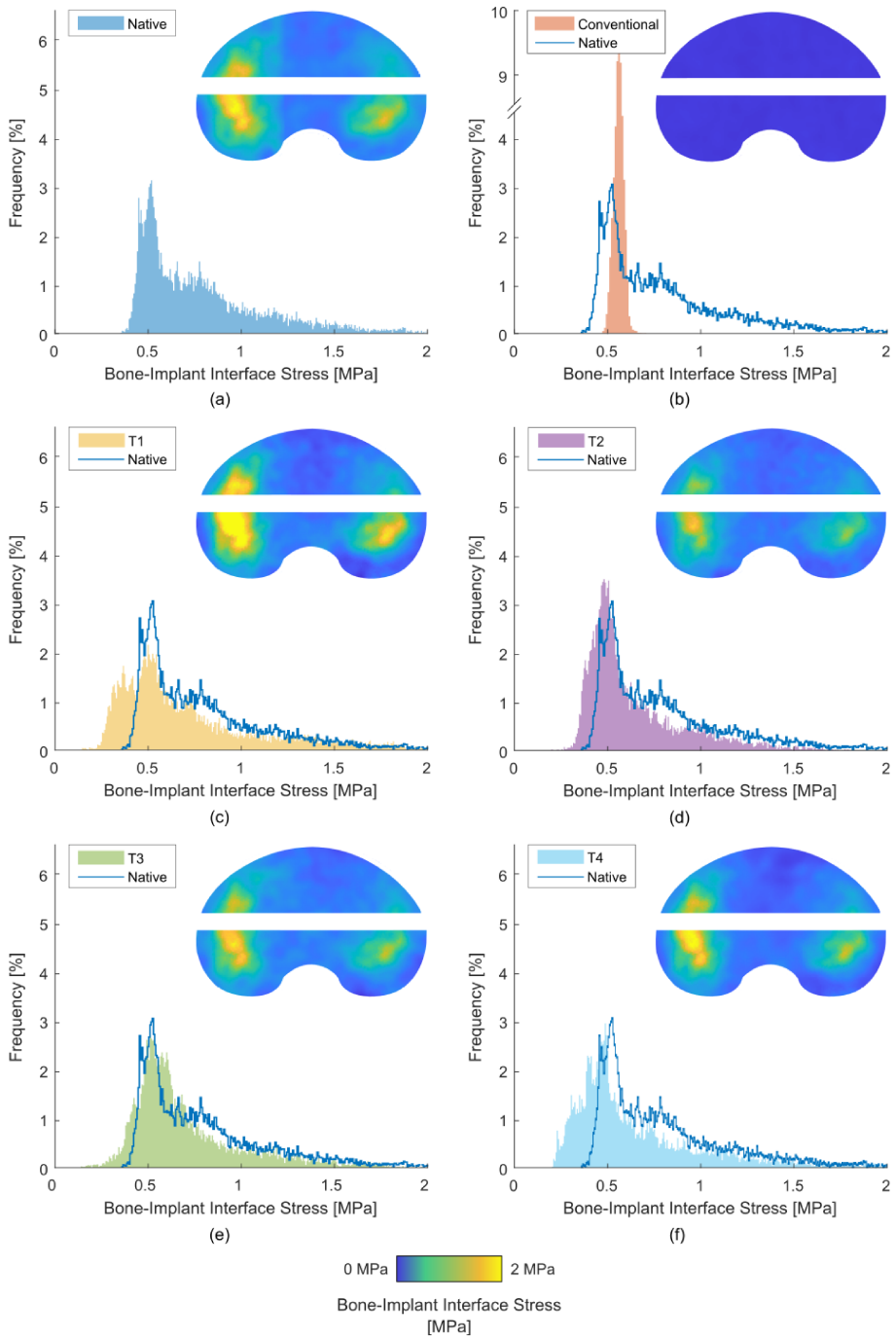


Figure 6.5: Bone-implant interface stress distribution in TKA. Average stress maps and histogram plots of bone-implant interface stress in TKA for (a) the native case, (b) conventional implants and the additive manufactured variants; (c) T1, (d) T2, (e) T3 and (f) T4. Note the break in axis of Figure b.

Maximum induced stress

In the medial condyle the maximum stress was not changed by the presence of three out of four of the titanium lattice implants (T2-T4) compared to the native case ($P>0.05$) and was between 2 and 2.5 MPa in these cases. The T1 titanium lattice implant generated a maximum stress 1.3 times greater than the native case ($p<0.05$) with a value of 2.7 MPa. The conventional implant (T0) generated a maximum stress 10.5 times lower than the native case ($p<0.05$) with a value of 0.2 MPa. In the lateral condyle, the maximum stress was not changed by the presence of the titanium lattice implants (T1-T4) compared to the native case ($P>0.05$) and was between 1.5 and 2 MPa in all cases. The conventional implant (T0) generated a maximum stress 8.5 times lower than the native case ($p<0.05$) with a value of 0.2 MPa.

In the native case, the maximum stress in the medial condyle was 20% greater than that in the lateral side ($p<0.01$). For the titanium lattice implants (T1-T4) the maximum stress in the medial condyle was 30% to 40% greater than in the lateral side (Figure 6.6, Table 6.3) ($p<0.01$). For the conventional implant (T0), no difference was found between stresses in the medial and lateral condyle ($p>0.05$).

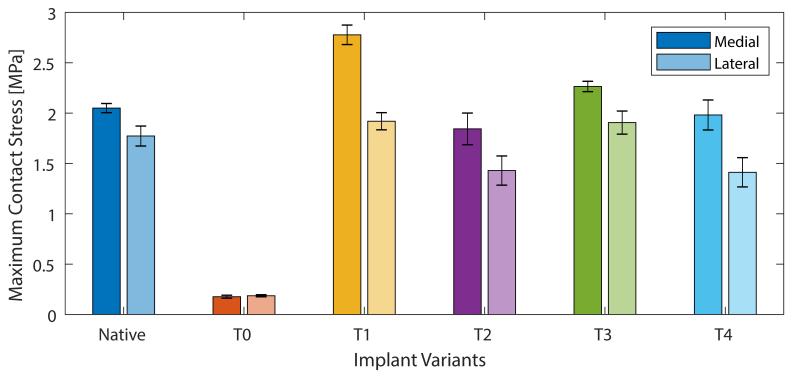


Figure 6.6: Maximum bone-implant interface stress in TKA. Maximum stress for each condyle in TKA loading, for all test variants.

Table 6.3: Summary of results for TKA implant variants. Mean measures for similarity of stress distribution [%], percentage of interface area underloaded compared to the native case [%] and maximum stress [MPa] in the medial TKA.

Test Variant	Jaccard Similarity	Area Underloaded	Maximum Stress	
			Medial	Lateral
	[%]	[%]	[MPa]	[MPa]
Native	-	-	2.1±0.1	1.7±0.2
M0	20.5±2.4	77.0±1.2	0.2±0.0	0.2±0.0
M1	77.6±5	0.9±0.8	2.7±0.7	1.9±0.2
M2	67.8±12.1	0.5±0.4	1.8±0.3	1.4±0.2
M3	74.2±5.8	1.7±0.5	2.2±0.1	1.7±0.3
M4	72.9±8.1	0.5±0.3	2.0±0.2	1.4±0.2

6.4 Discussion

6.4.1 Summary of Results

The most important finding of this study is that titanium lattice UKA and TKA implants can provide a load transfer in the proximal tibia that is very close to the native un-implanted bone, while conventional solid titanium implants underloaded 71% and 77% of the tibial bone surface area respectively. Both UKA and TKA titanium lattice implants generated the same magnitude and distribution of stress across the tibia as native bone, while conventional UKA and TKA implants generated peak stress magnitudes in the bone 10 and 9.7 times lower than the native case respectively. By maintaining normal load transfer to the bone, the titanium lattice implants may provide the mechanical conditions for normal bone remodelling throughout the implant's life.

6.4.2 Comparison to Literature

Our data can be compared to clinical observations of cementless trabecular metal-type tibial implants that have lower stiffness than conventional implants. A 13-year randomised controlled trial of such a device found better patient outcome and radiological findings compared to a conventional metal backed design [33]. This improved performance may have been partially due to the more normal load transfer for the trabecular metal design. Our data can also be compared to computational models of load transfer in the tibia [31, 34–36]. These models report stresses in the intact native tibia are centred around contact focal points and range from 0.06-2.4 MPa [35, 37, 38]. They also predict bone-implant interface stress to be 0.03-0.15 MPa after conventional medial UKA and TKA [35, 36, 38]. The same computational analyses reported that reduced modulus

implants (0.7-1.5 GPa) engender a bone-implant interface stress of 0.9-1.8 GPa [37, 39]. Our data concurs with all these prior findings, but our study is the first to manufacture such implants and demonstrate this in a human cadaveric study.

In addition to measuring load transfer, we had an unexpected finding related to the loadshare between the medial and lateral condyle. Many sources in literature observe that most of the load in the native knee is transmitted through the medial condyle [31]. For the native knee, our data matched this, with 53-62% of the load beneath the condyle concentrated on the medial side. However, when the conventional TKA was performed, the medial load share dropped to 48-52%. So while the adductor moment defines the medial/lateral load share at the bearing surface of the knee, the stiff tibial base plate of the conventional TKA may cause a more uniform load transfer to the bone with reduced medial bias. This has been observed previously [37]. Conversely, the titanium lattice implants closely replicated the native medial-lateral load split, with results ranging from 53-59% across all additive manufactured variants.

6.4.3 Considerations

A limitation of this study is that we used cadaveric specimens and assume the data translates to living bone. To minimise this we used fresh frozen specimens, not embalmed, and left all tissues critical to the loading intact. Another limitation was that the loading situation was a simplified example of someone standing still (full extension at body weight loading) whereas in reality a spectrum of loading conditions are applied to the proximal tibia. This study measured only contact stress at the bone-implant interface rather than internal stress and strain distribution within the bone. Further work is needed to explore the effects of additive manufactured implants on internal strains. All specimen donors in this study were male, due to supplier constraints. This is a limitation of the study because women are typically more affected by osteoarthritis than men and this should be explored furhter in future work. A technical limitation was the method of measuring contact stress in the native case required a transverse slot to be cut in the bone to place the sensor at the site of the bone-implant interface. The effects of this limitation were deemed to be acceptable following a finite element analysis which measured differences in contact stress between our experimental case and intact tibia of less than 3%. This was modelled with loading of 700N over a 60:40 medial:lateral load split and boundary conditions for the proximal tibial piece(s) applied from literature [40, 41]. A final limitation is that the lattice implant variants 1-4 represent a purist approach of matching the bone properties to demonstrate what is possible – future development of this concept would need design compromises to meet fatigue loading requirements such as ISO 14879-1:2020. However the additive manufacturing method is ideally suited to reach a compromise between load sharing and fatigue strength because solid

reinforcing elements can be built into the design at the CAD stage. In this study the implants had a thickness of 3mm (the same as most UKA and TKA implants on the market) and each size for both UKA and TKA had medial-lateral dimensions, anterior-posterior dimensions and profiles based on commonly used implants. In the future further analysis could be performed to determine the optimum size range and profile for tibial implants. Given that the UKA and TKA implants had dimensions comparable to typical implants, the joint line position was maintained when converting from UKA to TKA by moving the tibial resection plane distally - no more than a few milimeters.

6.4.4 Clinical Significance

Titanium lattice implants can restore native loading in the human knee following unicompartmental and total knee arthroplasty. This could be an improvement on the state of the art, enabling normal distribution of load in bone and therefore improved maintenance of bone density following UKA and TKA procedures. By maintaining normal distribution of load, the maintenance of bone throughout the implant's life could improve the bone implant interface, improving function and reducing pain. By maintaining loading across the whole metaphysis, titanium lattice implants would also make revision arthroplasty procedures easier for surgeons, less expensive for health care providers and safer for patients.

6.5 Conclusion

This study showed that normal load transfer in the proximal tibia can be maintained after knee arthroplasty (UKA and TKA) by using additive manufactured titanium lattice tibial components. By maintaining normal load transfer this study provides an exciting and encouraging case for the development of orthopaedic implants which can maintain healthy bone for a longer portion of a patient's lifetime.

6.6 Bibliography

[1] M. M. Petersen, C. Olsen, J. B. Lauritzen, and B. Lund, "Changes in bone mineral density of the distal femur following uncemented total knee arthroplasty," *The Journal of Arthroplasty*, vol. 10, pp. 7–11, 2 1995.

[2] J. T. Deen, T. B. Clay, D. A. Iams, M. B. Horodyski, and H. K. Parvataneni, "Proximal tibial resorption in a modern total knee prosthesis," *Arthroplasty Today*, vol. 4, pp. 244–248, 6 2018.

[3] P. Howard, R. Brittain, S. Lawrence, J. Stonadge, M. Wilkinson, T. Wilton, S. Dawson-Bowling, A. Watts, O. Specialists, R. Craig, C. Esler, A. Goldberg, S. Jameson, T. Jennison, J. Rees, A. Toms, E. Young, C. Boulton, D. Taylor, O. Espinoza, V. Mccormack, C. Newell, M. Royall, M. Swanson, Y. Ben-Shlomo, A. Blom, E. Clark, K. Deere, C. Gregson, L. Hunt, A. Judge, E. Lenguerrand, A. Price, D. Prieto-Alhambra, A. Sayers, and M. Whitehouse, "National Joint Registry | 17th Annual Report," tech. rep., National Joint registry, 2020.

[4] L. E. Bayliss, D. Culliford, A. P. Monk, S. Glyn-Jones, D. Prieto-Alhambra, A. Judge, C. Cooper, A. J. Carr, N. K. Arden, D. J. Beard, and A. J. Price, "The effect of patient age at intervention on risk of implant revision after total replacement of the hip or knee: a population-based cohort study," *The Lancet*, vol. 389, pp. 1424–1430, 4 2017.

[5] R. Huiskes, H. Weinans, and B. van Rietbergen, "The relationship between stress shielding and bone resorption around total hip stems and the effects of flexible materials.," *Clinical orthopaedics and related research*, vol. 274, no. Jan, pp. 124–134, 1992.

[6] D. S. Elliott, K. J. H. Newman, D. P. Forward, D. M. Hahn, B. Ollivere, K. Kojima, R. Handley, N. D. Rossiter, J. J. Wixted, R. M. Smith, and C. G. Moran, "A unified theory of bone healing and nonunion," *The Bone & Joint Journal*, vol. 98-B, pp. 884–891, 7 2016.

[7] G. M. Pagnotti, M. Styner, G. Uzer, V. S. Patel, L. E. Wright, K. K. Ness, T. A. Guise, J. Rubin, and C. T. Rubin, "Combating osteoporosis and obesity with exercise: leveraging cell mechanosensitivity," *Nature Reviews Endocrinology*, vol. 15, no. 6, pp. 339–355, 2019.

[8] C. T. Rubin and L. E. Lanyon, "Regulation of bone formation by applied dynamic loads," *Thr Journal of Bone and Joint Surgery*, vol. 66, no. April, pp. 397–402, 1984.

[9] S. M. Perren, "Physical and biological aspects of fracture healing with special reference to internal fixation.," *Clinical orthopaedics and related research*, no. 138, pp. 175–196, 1979.

[10] J. Wolff, "Concept of the Law of Bone Remodelling," in *The Law of Bone Remodelling*, Berlin, Heidelberg: Springer Berlin Heidelberg, 1986.

[11] S. Sturm, S. Zhou, Y. W. Mai, and Q. Li, "On stiffness of scaffolds for bone tissue engineering-a numerical study," *Journal of Biomechanics*, vol. 43, no. 9, pp. 1738–1744, 2010.

[12] L. Zhu, D. Luo, and Y. Liu, "Effect of the nano/microscale structure of biomaterial scaffolds on bone regeneration," *International Journal of Oral Science*, vol. 12, no. 1, pp. 1–15, 2020.

[13] N. Reznikov, C. Phillips, M. Cooke, A. Garbout, F. Ahmed, and M. M. Stevens, "Functional Adaptation of the Calcaneus in Historical Foot Binding," *Journal of Bone and Mineral Research*, vol. 32, pp. 1915–1925, 2017.

[14] S. Naghieh, M. R. Karamooz Ravari, M. Badrossamay, E. Foroozmehr, and M. Kadkhodaei, "Numerical investigation of the mechanical properties of the additive manufactured bone scaffolds fabricated by FDM: The effect of layer penetration and post-heating," *Journal of the Mechanical Behavior of Biomedical Materials*, vol. 59, pp. 241–250, 2016.

[15] S. Ghouse, N. Reznikov, O. R. Boughton, S. Babu, K. G. Ng, G. Blunn, J. P. Cobb, M. M. Stevens, and J. R. Jeffers, "The design and in vivo testing of a locally stiffness-matched porous scaffold," *Applied Materials Today*, vol. 15, pp. 377–388, 6 2019.

[16] R. Wauthle, J. Van Der Stok, S. A. Yavari, J. Van Humbeeck, J. P. Kruth, A. A. Zadpoor, H. Weinans, M. Mulier, and J. Schrooten, "Additively manufactured porous tantalum implants," *Acta Biomaterialia*, vol. 14, pp. 217–225, 3 2015.

[17] J. Wieding, T. Lindner, P. Bergschmidt, and R. Bader, "Biomechanical stability of novel mechanically adapted open-porous titanium scaffolds in metatarsal bone defects of sheep," *Biomaterials*, vol. 46, pp. 35–47, 4 2015.

[18] H. Spece, T. Yu, A. Law, M. Marcolongo, and S. Kurtz, "3D printed porous PEEK created via fused filament fabrication for osteoconductive orthopaedic surfaces," *Journal of the Mechanical Behavior of Biomedical Materials*, vol. 109, p. 103850, 2020.

[19] M. J. Munford, K. C. G. Ng, and J. R. T. Jeffers, "Mapping the Multi-Directional Mechanical Properties of Bone in the Proximal Tibia," *Advanced Functional Materials*, vol. 30, p. 2004323, 2020.

[20] U. Hossain, S. Ghouse, K. Nai, and J. R. Jeffers, "Controlling and testing anisotropy in additively manufactured stochastic structures," *Additive Manufacturing*, vol. 39, p. 101849, 3 2021.

[21] A.-M. Pobloth, S. Checa, H. Razi, A. Petersen, J. C. Weaver, K. Schmidt-Bleek, M. Windolf, A. Tatai, C. P. Roth, K.-D. Schaser, G. N. Duda, and P. Schwabe, "Mechanobiologically optimized 3D titanium-mesh scaffolds enhance bone regeneration in critical segmental defects in sheep.," *Science translational medicine*, vol. 10, 1 2018.

[22] J. Henkel, M. A. Woodruff, D. R. Epari, R. Steck, V. Glatt, I. C. Dickinson, P. F. M. Choong, M. A. Schuetz, and D. W. Hutmacher, "Bone Regeneration Based on Tissue Engineering Conceptions — A 21st Century Perspective," *Bone Research*, vol. 1, pp. 216–248, 2014.

[23] N. Harrison, J. R. Field, F. Quondamatteo, W. Curtin, P. E. McHugh, and P. McDonnell, "Preclinical trial of a novel surface architecture for improved primary fixation of cementless orthopaedic implants," *Clinical Biomechanics*, vol. 29, pp. 861–868, 9 2014.

[24] N. Harrison, P. E. McHugh, W. Curtin, and P. Mc Donnell, "Micromotion and friction evaluation of a novel surface architecture for improved primary fixation of cementless orthopaedic implants," *Journal of the Mechanical Behavior of Biomedical Materials*, vol. 21, pp. 37–46, 5 2013.

[25] S. Ghouse, S. Babu, R. J. Van Arkel, K. Nai, P. A. Hooper, and J. R. Jeffers, "The influence of laser parameters and scanning strategies on the mechanical properties of a stochastic porous material," *Materials and Design*, pp. 498–508, 2017.

[26] Irfan Abdulla, J. W. G. J. A. Daniel G Langohr Johnson, and G. S. Athwal, "The effect of humeral polyethylene insert constraint on reverse shoulder arthroplasty biomechanics," *Shoulder & Elbow*, vol. 10, no. 1, pp. 25–31, 2017.

[27] R. J. van Arkel, S. Ghouse, P. E. Milner, and J. R. Jeffers, "Additive manufactured push-fit implant fixation with screw-strength pull out," *Journal of Orthopaedic Research*, vol. 36, pp. 1508–1518, 5 2018.

[28] A. J. Garner, O. W. Dandridge, R. J. van Arkel, and J. P. Cobb, "The compartmental approach to revision of partial knee arthroplasty results in nearer-normal gait and improved patient reported outcomes compared to total knee arthroplasty," *Knee Surgery, Sports Traumatology, Arthroscopy*, pp. 1–10, 8 2021.

[29] M. N.Joseph, M. R.Carmontc, H. Tailor, J. M.Stephen, and A. A. Amis, "Total knee arthroplasty reduces knee extension torque in-vitro and patellofemoral arthroplasty does not," *Journal of Biomechanics*, vol. 104, no. May, p. 109739, 2020.

[30] F. Farahmand, W. Senavongse, and A. A. Amis, "Quantitative study of the quadriceps muscles and trochlear groove geometry related to instability of the patellofemoral joint," *Journal of Orthopaedic Research*, vol. 16, pp. 136–143, 1 1998.

[31] M. A. Verstraete, P. A. Meere, G. Salvadore, J. Victor, and P. S. Walker, “Contact forces in the tibiofemoral joint from soft tissue tensions: Implications to soft tissue balancing in total knee arthroplasty,” *Journal of Biomechanics*, vol. 58, pp. 195–202, 6 2017.

[32] T. T. Tanimoto, “elementary mathematical theory of classification and prediction,” 1958.

[33] M. Hampton, J. Mansoor, J. Getty, and P. M. Sutton, “Uncemented tantalum metal components versus cemented tibial components in total knee arthroplasty: 11- to 15-year outcomes of a single-blinded randomized controlled trial,” *The Bone & Joint Journal*, vol. 102-B, pp. 1025–1032, 8 2020.

[34] M. Tuncer, U. N. Hansen, and A. A. Amis, “Prediction of structural failure of tibial bone models under physiological loads: Effect of CT density–modulus relationships,” *Medical Engineering & Physics*, vol. 36, pp. 991–997, 8 2014.

[35] S. Nakamura, Y. Tian, Y. Tanaka, S. Kuriyama, H. Ito, M. Furu, and S. Matsuda, “The effects of kinematically aligned total knee arthroplasty on stress at the medial tibia,” *Bone & Joint Research*, vol. 6, pp. 43–51, 1 2017.

[36] K. Iesaka, H. Tsumura, H. Sonoda, T. Sawatari, M. Takasita, and T. Torisu, “The effects of tibial component inclination on bone stress after unicompartmental knee arthroplasty,” *Journal of Biomechanics*, vol. 35, pp. 969–974, 7 2002.

[37] B. Innocenti, E. Truyens, L. Labey, P. Wong, J. Victor, and J. Bellemans, “Can medio-lateral baseplate position and load sharing induce asymptomatic local bone resorption of the proximal tibia? A finite element study,” *Journal of Orthopaedic Surgery and Research*, vol. 4, pp. 1–15, 7 2009.

[38] P. Zhang, J. Liu, and A. C. To, “Role of anisotropic properties on topology optimization of additive manufactured load bearing structures,” 2016.

[39] C. E. H. Scott, M. J. Eaton, R. W. Nutton, F. A. Wade, S. L. Evans, and P. Pankaj, “Metal-backed versus all-polyethylene unicompartmental knee arthroplasty,” *Bone & Joint Research*, vol. 6, pp. 22–30, 1 2017.

[40] T. Fukubayashi and H. Kurosawa, “the contact area and pressure distribution pattern of the knee: A study of normal and osteoarthrotic knee joints,” *Acta Orthopaedica*, vol. 51, no. 1-6, pp. 871–879, 1980.

[41] P. Wretenberg, D. K. Ramsey, and G. Németh, “Tibiofemoral contact points relative to flexion angle measured with MRI,” *Clinical Biomechanics*, vol. 17, pp. 477–485, 7 2002.

7 Overall Discussion

7.1 Most Important Findings

7.2 Advancement of the Field

This thesis contributes to the advancement of the field and scientific understanding of key aspects of developing orthopaedic implants which encourage positive bone remodelling. This has been particularly exciting because the use of additive manufacturing in orthopaedics is growing and has potential to revolutionise the field with implants which maintain bone density and improve fixation. This same technology has applications in reconstruction of any joint in the body, such as the hip, patellofemoral joint, shoulder, spine or large defects in trauma cases.

A summary of the advancements made in the field of orthopaedics, and in particular additive manufacturing in orthopaedics, is given below:

7.2.1 Prediction and characterisation of bone's properties

The work in Chapter 3 characterised how bone's multiaxial modulus is heterogeneously distributed across the proximal tibia and enabled prediction of properties based on density data from CT scans, patient attribute and anatomical location. This was achieved to a greater level of understanding and resolution than previous data allowed.

7.2.2 Characterisation and control of lattice modulus and anisotropy

The work in Chapter 4 on the prediction of lattice properties has been fundamental in designing implants for testing. This work built upon existing methods in

literature to generate a model capable of predicting anisotropy properties in a biomimetic structure. This combined fundamental theoretical tensor relationships with modern manufacturing and testing methods to build a more complete model than previously available.

7.2.3 Application of lattices for fine control of bone strains

Imperial College London's Biomechanics group's additive manufacturing (AM) methods and structures has built upon existing literature to navigate limitations of the manufacture method. Much of the work conducted in the Biomechanics group prior to this thesis focused on the use of stochastic structures to navigate intellectual property that exists on the use of repeating cell structures. In Chapter 5 these existing methods were further developed to demonstrate a workflow which seamlessly varied the AM laser parameters with the strut angle to control structure anisotropy beyond what has been achieved before. This allows manufacture of structures which could control bone's strain response in multiple directions using only a CT scan of the bone.

7.2.4 Demonstration of the technology in partial and total knee implants

The proof of concept implants tested in Chapter 6 achieve novel and progressive results in human cadaveric testing. This work showed that stiffness matched implants can replicate a healthy mechanical environment and quantified the extent to which existing implants neglect this. Until now, low modulus or stiffness matched metal implants had been hypothesised but never shown or proven. The work in this Chapter made a key step towards ensuring that no solid material is included in the implant in the load path from the femur through the implant to the tibia, this is required for implants to be biomimetic and stimulate positive bone remodelling. This work represents an exciting development in the field and a development towards the future of orthopaedics.

7.3 Translational Opportunity

A key requirement of the work in this thesis was that the technology and results be scalable for use in the orthopaedic industry. The above outcomes are particularly important because they are all applicable and directly translatable into orthopaedics. For example, the methods used to extract density from calibrated CT scans can be used alongside existing clinical CT machines and protocols and the manufacturing methods and materials used in Chapters 4 through 6 are already in use within regulatory systems in the orthopaedic industry.

An important consideration for the future development of this work is the design of a mechanism to affix polymer bearings to the lattice components shown in

Chapter 6. Polymer bearing components are required to ensure a low wear articulating surface. Conventional methods use a mechanical clip or snap fit, with a hook mechanism between the polymer and metal components, but this requires solid metal to be present along the load path from femur to tibia. Ideally, the presence of solid metal obstructing the natural load path would be avoided as this will improve positive bone remodelling. Preliminary work on a fixation method between the metal and polymer has already begun.

Comparing the technology and results in this thesis with existing orthopaedic implants, a stark difference can be seen. Although some existing implants do utilise additive manufacturing technology, they still provide solid metal solutions, sometimes with a porous coating [1–3]. This means that no existing solutions attempt to address the underlying problems of many arthroplasty complications, which require a natural or positive remodelling process. The lattice implants shown in Chapter 6 may be further developed to achieve implants which maintain positive remodeling strains in peri-prosthetic bone, by matching the implant to bone's modulus, while also achieving sufficient strength in the implant for regulatory testing.

There are 1.3M knee patients treated worldwide every year and the proportion of patients who are under the age of 65 is growing (currently approximately 40%) [4]. Surgeons are currently hesitant to treat these young patients because they experience high failure rates and revision surgery has daunting consequences for the patient's quality of life [5]. By offering a viable route for surgeons to treat young patients without risking their ability to remain active in later life, the technology and implants developed in this thesis could revolutionise orthopaedics to benefit both patients and surgeons.

Healthcare providers would also benefit from implants like those developed in this thesis. Particularly partial knee implants have been shown to be cost-effective at the point of care and in the long-term compared to total knee implants. Patients have a significant risk of needing revision during their lifetime (~30% for patients under 65, ~10% for patients aged 65-75) and revisions to a TKA are more costly than a primary procedure [6–8].

The orthopaedics industry is dominated by 4 large US companies: Zimmer Biomet, Stryker, Smith & Nephew and DePuy Synthes. A likely route to establish our implants in the market would be to partner with one of these companies as a distributor. With this opportunity there are many challenges, including: protecting intellectual property, establishing and maintaining market fit, building a team, developing through regulation and many more. I am committed and motivated to bringing this technology from lab to operating room to keep patients healthy, active and enjoying life. In the past year we have begun OSSTEC, an orthopaedics start-up, to execute this plan.

There is much to be done in terms of protecting intellectual property, building a team that can realise this vision, securing funding and gaining clinical data for our implants. The past year has been an exciting time for me on this journey, in particular the past 6 months as we have won an InnovateUK grant and secured our first investment to bring this startup, OSSTEC, to life. Our greatest challenge going forward will be to establish relationships and partnerships with orthopaedic manufactures and original equipment manufacturers (OEMs) and we are mitigating this by engaging with OEMs at an early stage.

7.4 Future work

Further work is needed to make our implants a reality to help patients, surgeons, healthcare providers and distributors. This process includes both technical and commercial challenges.

7.4.1 Technical Limitations

With regards to further technical work, there are several key limitations of the studies presented here which can be addressed. These include analysis of sex effects, which were not explored in Chapter 6 and were underpowered in Chapter 3.

Furthermore, the studies presented in this thesis were limited by the number of freeze-thaw cycles used (Chapters 3 and 6), although this was mitigated as far as possible as discussed in the relevant Chapters, and by the use of cadaveric bone representing a time-zero analysis.

A key requirement for orthopaedic implants is that they satisfy high cycle fatigue loading. This is also a limitation of the additive manufacturing method because semi-sintered particles and weld lines cause inherent flaws and fatigue initiation sites. An interesting development for this work would be to progress towards implants which can achieve an optimal compromise between control of bone strains via axial loading and high fatigue strength through resistance to bending loads. Again, a key consideration here is to avoid the use of solid metal in the knee's load path. Promising initial data has been collected on this.

Similarly, wear characteristics of the implant have not been explored. It is proposed to integrate a polymer bearing (UHMWPE) into the implant. This material is readily used in the orthopaedic industry and has been shown to have sufficient articulating wear properties. Any fixing mechanism between the polymer and metal lattice would need to be characterised and tested in future.

Another exciting development for this thesis would be to integrate the underlying additive manufacturing technology into other implants, such as in the patellofemoral joint, shoulder and hip. Each of these cases has its own unique

loading environment and adaptation of the lattice structures developed here to accommodate high magnitude off-axis loads should be considered.

Further academic research is required in addition to industrial development work. This includes:

- Analysis of fixation feature design: Long-term fixation will be provided by bone ingrowth, whereas the absence of cement necessitates that initial fixation be provided by design of additional fixation features.
- Analysis of implant sizes and suitability for population: Various characteristics such as patient age, size, sex and ethnicity affect the size of implant a patient may need and this must be characterised.
- Possibility of integrating an additive manufactured articulating (AM) surface: This may be required in applications beyond the tibia. AM surfaces are typically rough and pitted and the layer-wise manufacturing process can lead to high local stresses under wear loading.
- Analysis of the effects of bone ingrowth: How does an implant with ingrowth affect bone's remodelling and how does the expected high level of fixation affect the ability to revise such an implant? This could be explored in an animal model with CT scans or X-rays to monitor one remodelling and ingrowth over time followed by micromotion and ease of revision testing upon sacrifice.

7.5 Conclusions

This work has characterised the distribution of bone's mechanical properties in the proximal tibia, describing bone as a orthotropic material with apparent modulus and strength 1.7 and 3 times respectively higher in the axial direction compared to the transverse directions. In the dominant axial direction, the bone was 1.3 times stiffer in the medial condyle than the lateral condyle. This was because the proximal cancellous bone in the medial condyle had an elastic modulus of 610 MPa that only decreased by about 10% over a 25 mm distal distance. In contrast, the proximal cancellous bone in the lateral condyle had an elastic modulus of 562 MPa that decreased by 50% over the same 25 mm distal distance.

Furthermore, it was shown that off-axis apparent modulus and strength of lattice structures can be predicted using fabric and elasticity equations. This tool, although less complete than finite element methods, provides a rapid and accurate way to analyse the modulus, strength and anisotropy of lattices to be determined while the component is at an early stage in the design process - without extensive computational power. A range of moduli and strengths were

reliably predicted across all directions, from 0.6 - 2.9 GPa and 15 - 40 MPa respectively.

Combining these findings, it was possible to control axial strain experienced in bone with titanium scaffold structures whose modulus was defined from clinical CT scans. The resulting strain response in bone was controlled from -15% to +15% relative to homeostasis by an inverse linear relationship with the titanium scaffold structure's apparent modulus.

The most important outcome of this work was that titanium lattice UKA and TKA implants can provide a load transfer in the proximal tibia that is very close to the native un-implanted bone. Furthermore, conventional solid titanium implants underloaded 71% (UKA) and 77% (TKA) of the tibial bone surface area respectively. Both UKA and TKA titanium lattice implants generated the same magnitude and distribution of stress across the tibia as native bone, whereas a reduction in stresses experienced in the bone of a factor of 10 (UKA) and 9.7 (TKA) were seen for conventional implants.

Ultimately this PhD thesis has established a workflow to generate additive manufactured structured which have mechanical properties closely tune to their surrounding bone, with implications to improve positive bone remodelling. This technology has possibilities to benefit patient cohorts who are young and active where faster healing capacity can be utilised, or patients with reduced bone density. By maintaining normal load transfer to the bone, titanium lattice implants may provide the mechanical conditions for normal bone remodelling throughout the implant's life, with opportunity to reduce implant failures to keep patients healthy and active.

7.6 Bibliography

[1] Zimmer Biomet, "Annual Report," tech. rep., 2020.

[2] Stryker, "Triathlon Tritanium Knee System," 2015.

[3] GlobalData, "Global hip and knee replacement market report," tech. rep., 2018.

[4] OECD, "Knee Replacement by Country - Health Care Utilisation: Medical technology," 7 2020.

[5] L. E. Bayliss, D. Culliford, A. P. Monk, S. Glyn-Jones, D. Prieto-Alhambra, A. Judge, C. Cooper, A. J. Carr, N. K. Arden, D. J. Beard, and A. J. Price, "The effect of patient age at intervention on risk of implant revision after total replacement of the hip or knee: a population-based cohort study," *The Lancet*, vol. 389, pp. 1424–1430, 4 2017.

[6] C. Willis-owen, K. Brust, H. Aslop, M. Miraldo, and J. P. Cobb, “Unicondylar knee arthroplasty in the UK National Health Service: An analysis of candidacy, outcome and cost efficacy,” *The Knee*, vol. 16, no. 6, pp. 473–478, 2009.

[7] S. Shankar, M. W. Tetreault, B. J. Jegier, G. B. Andersson, and C. J. Della Valle, “A cost comparison of unicompartmental and total knee arthroplasty,” *Knee*, vol. 23, no. 6, pp. 1016–1019, 2016.

[8] M. Bhandari, J. Smith, L. E. Miller, and J. E. Block, “Clinical and Economic Burden of Revision Knee Arthroplasty,” *Clinical Medicine Insights: Arthritis and Musculoskeletal Disorders*, vol. 5, p. CMAMD.S10859, 1 2012.

Appendix A

A.1 Appendices to Chapter 3

Table A.1: Model parameters for power law models for X, Y and Z apparent modulus. RMSE is given in MPa.

Test Direction	Apparent Modulus [GPa]			Model fit			
	Mean	Stan. Dev.	n	R^2	RMSE	Coefficient	Exponent
X	0.304	0.0.26	100	0.52	0.044	0.76	0.92
Y	0.362	0.300	101	0.57	0.050	0.91	0.93
Z	0.509	0.257	142	0.57	0.042	0.90	0.55

Table A.2: Model parameters for power law models for X apparent modulus data. Grouped by subchondral depth. RMSE is given in MPa.

Subchondral Depth [mm]	Apparent Modulus [GPa]		Model fit				
	Mean	Stan. Dev.	n	R^2	RMSE	Coefficient	Exponent
5	0.4187	0.2441	62	0.42	21	0.57	0.49
15	0.1564	0.0912	8	0.72	10	0.33	0.74
25	0.1379	0.0852	7	0.43	2	0.11	0.53
All	0.3607	0.2463	77	0.54	27	0.66	0.81

Table A.3: Model parameters for power law models for Y apparent modulus data. Grouped by subchondral depth. RMSE is given in MPa.

Subchondral Depth [mm]	Apparent Modulus [GPa]		Model fit				
	Mean	Stan. Dev.	n	R^2	RMSE	Coefficient	Exponent
5	0.4823	0.3041	62	0.58	28	0.77	0.72
15	0.3835	0.1178	11	0.49	51	0.48	0.52
25	0.1391	0.1160	4	0.64	21	0.16	0.35
All	0.4457	0.2740	76	0.62	29	0.81	0.89

Table A.4: Summary of Z apparent modulus data and power-law model parameters for the data. Grouped by subchondral depth and condyle.

Condyle	Subchondral Depth	Apparent Modulus			Model fit			
	[mm]	[GPa]						
		Mean	Stan. Dev.	n	R^2	RMSE	Coefficient	Exponent
Lateral	5	0.562	0.161	34	0.75	7	0.82	0.46
	15	0.342	0.195	20	0.71	11	1.44	1.13
	25	0.290	0.107	12	0.64	6	0.52	0.38
	All	0.437	0.211	66	0.75	13	0.87	0.63
Medial	5	0.610	0.280	41	0.73	32	0.87	0.56
	15	0.571	0.291	16	0.66	21	0.92	0.38
	25	0.532	0.199	8	0.83	6	1.28	0.79
	All	0.585	0.279	65	0.74	34	0.79	0.37

Table A.5: Model parameters for power law models for strength data. Grouped by test direction.

Test Direction	Model fit				
	n	R^2	RMSE [MPa]	Coefficient	Exponent
X	76	0.68	585	3.94	0.60
Y	74	0.65	413	3.29	0.56
Z	33	0.81	3230	16.08	1.63

A.2 Appendices to Chapter 4

The regression matrices for the known values of y, the column vector containing the elements from the observed orthotropic compliance tensor, and X were formed as below for the system of equations ($y = Xc + e$). Multiple data points for each row entry was performed so that a least squared regression could be performed to determine the coefficients in c.

$$\begin{pmatrix} ln\left(\frac{1}{S_{11}}\right) \\ ln\left(\frac{1}{S_{22}}\right) \\ ln\left(\frac{1}{S_{33}}\right) \\ ln\left(\frac{\nu}{S_{12}}\right) \\ ln\left(\frac{\nu}{S_{13}}\right) \\ ln\left(\frac{\nu}{S_{23}}\right) \end{pmatrix} = \begin{pmatrix} 1 & 0 & 0 & 0 & 0 & 0 & ln\left(\frac{1}{\rho}\right) & ln\left(\frac{1}{D_1^2}\right) & 0 & 0 \\ 0 & 1 & 0 & 0 & 0 & 0 & ln\left(\frac{1}{\rho}\right) & 0 & ln\left(\frac{1}{D_2^2}\right) & 0 \\ 0 & 0 & 1 & 0 & 0 & 0 & ln\left(\frac{1}{\rho}\right) & 0 & 0 & ln\left(\frac{1}{D_3^2}\right) \\ 0 & 0 & 0 & 1 & 0 & 0 & ln\left(\frac{1}{\rho}\right) & \left(\frac{1}{D_1}\right) & ln\left(\frac{1}{D_2}\right) & 0 \\ 0 & 0 & 0 & 0 & 1 & 0 & ln\left(\frac{1}{\rho}\right) & \left(\frac{1}{D_1}\right) & 0 & ln\left(\frac{1}{D_3}\right) \\ 0 & 0 & 0 & 0 & 0 & 1 & ln\left(\frac{1}{\rho}\right) & 0 & \left(\frac{1}{D_2}\right) & ln\left(\frac{1}{D_3}\right) \end{pmatrix} \begin{pmatrix} ln(\lambda_{11}) \\ ln(\lambda_{22}) \\ ln(\lambda_{33}) \\ ln(\lambda_{12}) \\ ln(\lambda_{13}) \\ ln(\lambda_{23}) \\ k \\ l_1 \\ l_2 \\ l_3 \end{pmatrix}$$

$$+ \begin{pmatrix} e_1 \\ e_2 \\ e_3 \\ e_4 \\ e_5 \\ e_6 \end{pmatrix}$$

A.3 Appendices to Chapters 5 and Chapter 6

The equilibration technique refered to in Chapters 5 and 6 for Tekscan pressure film used the fixtures described below. A rigid plate was allowed to rotate freely on a spherical ball joint (Figure A.1). A Tekscan pressure sensor was placed between the rigid plate and a Instron platens, with load increased so the platens were just in contact with the pressure sensor and rigid plate. At this point the rigid plate had rotated into position to be parallel with the Instron platens.

The load was increased to 800 N to equilibrate the pressure sensor. Adjustment of the four bolts in Figure A.1 allowed fine control of the distribution of pressure seen by the Tekscan sensels. The four bolts were adjusted to give a uniform distribution of pressure across the sensor and then the automatic Tekscan equilibration was performed. This was repeated every time a new sensor was used.

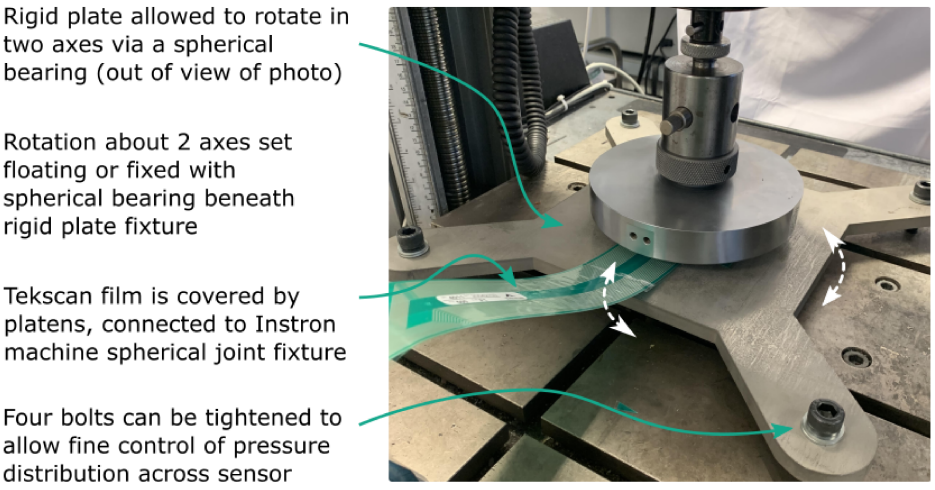


Figure A.1: Tekscan pressure film equilibration fixture. The full setup used to perform equilibration and calibration of Tekscan pressure films.